Met O (APR) Turbulence and Diffusion Note No. 246

Three-dimensional (STOCHEM) model studies of regional and global scale formation of tropospheric oxidants and acidifying substances

by

D. S. Stevenson, C. E. Johnson, W. J. Collins and R. G. Derwent

Hadley Centre for Climate Research
Meteorological Office
London Road
Bracknell
Berks, RG12 2SZ

This work was supported through the Public Meteorological Service research and development programme of the Meteorological Office, as part of the research programme of the Air and Environment Quality Division of the Department of the Environment, Transport and Regions through contract number EPG 1/3/93 and as part of the Climate Prediction programme of the Global Atmosphere Division of the Department of the Environment, Transport and Regions through contract number PECD 7/12/37.

THREE-DIMENSIONAL (STOCHEM) MODEL STUDIES OF REGIONAL AND GLOBAL SCALE FORMATION OF TROPOSPHERIC OXIDANTS AND ACIDIFYING SUBSTANCES

D S STEVENSON C E JOHNSON W J COLLINS and R G DERWENT

Hadley Centre for Climate Research,
Meteorological Office, Bracknell, Berkshire RG12 2SZ.

Abstract

In this study, a global 3-D Lagrangian chemistry model (STOCHEM) is applied to the formation of tropospheric oxidants and their influence on the regional scale formation and transport of photochemical ozone and on the deposition of acidic species. We show here how, without simultaneous action on the global scale to control methane and other tropospheric ozone precursors, concentrations of tropospheric oxidants will increase in future years, with the possibility of changing the intensity of regional scale photochemical episodes and the deposition patterns of acidic species in Europe. A number of policy scenarios are investigated to illustrate the coupling that might be anticipated between policy actions which might be envisaged in the global climate arena and measures currently under consideration to tackle acid rain within the European region. As the global tropospheric oxidant concentrations rise over the period from 1992 to 2015, total sulphur deposition loads over central Europe are expected to fall slower than SO_2 emissions. By the year 2015, peak ozone concentrations are anticipated to increase throughout Europe by about 10 ppb, during summertime and in the IS92a 'business-as-usual' scenario. The increase in ozone concentrations is diminished dramatically by the current reductions plans for NO_x and SO_2 emissions in both Europe and north America. However, maximum feasible reductions for NO_x and SO_2 in Europe are not enough to keep future peak ozone levels below internationally-accepted environmental criteria and action will be required on the global scale to control ozone precursor emissions, if ozone critical levels set to protect crops, are to be reached in the year 2015 within Europe.

THREE-DIMENSIONAL (STOCHEM) MODEL STUDIES OF REGIONAL AND GLOBAL SCALE FORMATION OF TROPOSPHERIC OXIDANTS AND ACIDIFYING SUBSTANCES

1. Introduction

It is considered likely that human activities have increased significantly the global baseline levels of ozone (O_3) in the northern hemisphere since preindustrial times (Hough and Derwent 1990). However, without the evidence of the increase in atmospheric concentrations from ice cores, we do not have the same confidence in the magnitude of the concentration increase with ozone as we do for the other greenhouse gases: methane (CH_4), nitrous oxide (N_2O) and carbon dioxide (CO_2) (IPCC 1996). The evidence that we do have for an ozone increase, is based on the fragmentary time series of reliable ozone measurements for the Montsouris Observatory, close to Paris, during the last century (Volz and Kley 1988). The ozone increase to present-day levels is about a factor of two and such an increase should be a general feature of much of the northern hemisphere troposphere. Photochemical models confirm that such an increase is plausible, based on our understanding of the global ozone life cycle and the impact of human activities upon it. Regional scale photochemical ozone episodes are superimposed on this global baseline and together they contribute to the damaging effects on plants, crops, semi-natural ecosystems and ultimately on human health (WHO 1987).

It has been recognised for some time now that the tropospheric oxidants such as ozone and hydrogen peroxide (H_2O_2) play an important role in the regional scale formation and deposition of acidic sulphur (SO_x) and nitrogen (NO_y and NH_x) species. There is therefore a close linkage between the problems of the global scale build-up of the tropospheric oxidants and regional scale acid rain (Grennfelt et al. 1994). The availability of tropospheric oxidants is thought to change the competitive balance between dry and wet deposition of acidic sulphur and nitrogen species and hence change the spatial scales of the deposition patterns spreading away from the source regions of sulphur dioxide (SO_2), oxides of nitrogen (NO_x) and ammonia (NH_3). These changes in deposition patterns, necessarily result from changes in lifetimes and hence mean transport distances of the acidic sulphur (SO_x), oxidised nitrogen (NO_y) and reduced nitrogen (NH_x) species. Policy actions to control acid rain in Europe, generally assume that deposition patterns or footprints will remain unchanged in the future, expressed in terms of unit pollutant release. That is to say, they assume that tropospheric oxidant levels and mean transport distances will remain unchanged into the future.

In this study, STOCHEM, a global 3-D Lagrangian chemistry model (Collins et al. 1997) is applied to the formation of tropospheric oxidants and their

influence on the regional scale formation and transport of photochemical ozone and on the deposition of acidic species. We show here how, without simultaneous action on the global scale to control methane and other tropospheric ozone precursors, concentrations of tropospheric oxidants will increase in future years, with the possibility of changing the intensity of regional scale photochemical episodes and the deposition patterns of acidic species in Europe. A number of policy scenarios are investigated to illustrate the coupling that might be anticipated between policy actions which might be envisaged in the global climate arena and measures currently under consideration to tackle acid rain within the European region.

2. Description of the Global 3-D Lagrangian Chemistry Model

So far the main approach to three-dimensional tropospheric chemistry modelling has been Eulerian. In the Eulerian approach, a regular rectangular grid is built throughout the model domain and a finite-differencing scheme is used to describe the processes involved in this fixed framework. The accurate representation of the advection of trace gases is not straightforward if negative concentrations, numerical dispersion and short timesteps are to be avoided (Chock and Winkler 1994; Dabdub and Seinfeld 1994). Pseudospectral techniques offer a formally accurate alternative to the conventional finite difference approach in models of atmospheric dynamics. However, when applied to atmospheric trace gas transport, they may generate negative concentrations and spurious oscillations.

In this study a Lagrangian approach has been adopted using 50,000 constant mass parcels of air, the centroids of which are advected by interpolated winds from the Meteorological Office UM operational model (Cullen 1993). By this method, all trace gas species are advected together so the chemistry and transport processes can be uncoupled and chemistry timesteps determined locally. There are disadvantages with the Lagrangian approach; species concentrations are defined on parcel centroids but output is generally required on an Eulerian grid and this may be over- or under- determined in a practical implementation where the number of parcels may be limited. Furthermore, distortions due to wind shears can render the notion of a distinct air parcel meaningless.

Although our implementation of the Lagrangian approach to three-dimensional chemistry and transport follows a number of the principles and approaches of the GRANTOUR model (Walton et al. 1988; Penner et al. 1991), it differs in a number of respects, including the handling of diffusion, reinitialisation of particles and the handling of emissions and deposition. The chemical scheme adopted contains 70 chemical species and is an extension of that employed in the development of European regional scale pollution control policies for ozone within the United Nations Economic Commission for Europe EMEP programme (Eliassen et al. 1982; Simpson 1991). A list of species is shown in Table 1.

Advection scheme

The height coordinate in the Meteorological Office Unified Model is a hybrid eta coordinate. This is derived from the atmospheric pressure at that height and the atmospheric pressure at the surface by the relation:

$$\eta = P/P_s + A\,(1/P_o - 1/P_s),$$

where P is the pressure,
P_s is the surface pressure,
P_o is a reference pressure (=1000 hPa) and
A is a coefficient having the dimensions of pressure.

A is set equal to zero near the surface and is equal to the pressure for heights greater than 30 hPa. Near the surface, η is terrain-following and is equal to P/P_s, above a height of 30 hPa, eta follows the pressure surfaces and is equal to P/(1000 hPa).

The Lagrangian cells are advected according to winds taken from the Meteorological Office UM operational model, which are based on a grid of 1.25° longitude, 0.833° latitude and 12 unevenly-spaced η levels between 1.0 and 0.0099 for the horizontal winds (U and V) and between 1.0 and 0.0075 for the vertical wind (W). The advection timestep is typically set to three hours and new cell positions are calculated using a 4th order Runge-Kutta advection scheme. Winds are interpolated linearly in time within the 6-hourly meteorological datasets, bi-linearly in the horizontal domain and using a cubic polynomial in the vertical.

Convection

Small-scale convective processes (i.e. smaller than can be resolved on the gridded wind data) can have a large influence on the tropospheric chemistry by lifting pollutants out of the boundary layer or bringing down O_3 and NO_y from the top of the troposphere (Ehhalt et al. 1992). We have included convection in our model using convective cloud fields diagnosed by the Unified Climate Model (these include convective cloud top height, convective cloud cover and convective precipitation). We mix completely a fraction of the cells throughout the column below the cloud top. The fraction mixed is given by the amount of cloud cover for clouds that are not precipitating, or by a mass flux calculated from the precipitation rate for those that are precipitating using a formula taken from Chatfield and Delany (1990). The mass flux is converted to a fraction by dividing it by the mass of air beneath the cloud base.

Inter-parcel exchange

During the advection process the Lagrangian cells are considered to be isolated parcels of air. However in reality the air is mixed with other parcels by diffusion processes characteristic of the size of a parcel. In this model the

mixing ratio of a species in a parcel c is brought closer to the average background mixing ratio $\underline{c}$ by adding a term ($\underline{c}$-c).d where d is a parameter representing the degree of exchange taken to be 10^{-3} in the troposphere and 10^{-6} in the stratosphere, (the division is taken arbitrarily to be at $\acute{\eta} = 0.4$). We estimate $\underline{c}$ to be the average mixing ratio of all the cells within a grid volume, which is chosen to be: 5° x 5° x $\Delta\acute{\eta} = 0.1$, as this gives an average of about one and a half cells per grid volume (more near the equator, less near the poles). The volumes are fixed to the Eulerian grid. The exchange is treated in a more theoretical manner by Walton et al. (1988).

Boundary layer height

The height of the boundary layer in our model is estimated from the archived Unified Model meteorological data in two ways based on a study by Maryon and Best (1992). The first is a dry adiabatic method. This involves following the dry adiabatic lapse rate curve up from the near-surface temperature and determining the height at which it intersects the environmental temperature profile. The second is a Richardson number method where the boundary layer height is taken to be the first model layer at which the bulk Richardson number exceeds a critical value. The critical value is usually taken as +0.25 but we use +1.3 as chosen by Maryon and Best (1992) which is more appropriate for the UM operational model output. The boundary layer height used is from the method giving the higher value. In practice the dry adiabatic method tends to be chosen in convective situations and the Richardson number method in stable situations.

Chemistry

The three-dimensional model STOCHEM contains a full description of the fast photochemistry of the troposphere and the free radical reactions which process the major tropospheric trace gases. Included in these emissions are those from human activities and industrial processes from the northern hemisphere continents, from aircraft operations in the free troposphere, from deforestation, biomass burning and agriculture in tropical and sub-tropical continental areas, natural emissions from oceans, soils, tundra and wetland systems. Accordingly, the chemistry describes the atmospheric oxidation and degradation of carbon monoxide, methane, a range of hydrocarbons, oxygenated hydrocarbons and simple sulphur compounds. Through the fast photochemistry reactions, these oxidation and degradation pathways are coupled to ozone and hydrogen peroxide production and destruction and hence control the oxidising capacity of the model troposphere.

The chemical and photochemical reactions included in the three-dimensional model chemistry are listed in Table 2, together with the assumed reaction pathways and rate coefficients. These data were compiled from databases of evaluated chemical kinetic data (Atkinson et al. 1992; DeMore et al. 1994; Atkinson et al. 1996), evaluations of previously published mechanisms (Wirtz et al. 1994) and commissioned reviews of the degradation mechanisms of

particular organic species such as isoprene and dimethyl sulphide (Jenkin et al. 1996). The chemical mechanism adopted includes a full description of both the nightime and daytime chemistry using a fixed five minute time-step.

A complete and detailed description of the chemistry outlined above would be well beyond the computer resources available and some simplifications have necessarily been made. The main form of simplification has been the neglect of highly reactive species where there is no significant change in competitive routes throughout the model domain. The hydrogen atom is not included explicitly in the mechanism because its sole fate is to form hydroperoxy radicals through reaction (1):

$$H + O_2 + M = HO_2 + M. \qquad (1).$$

The next class of species which have been neglected from the model chemistry, are the organic carbon radicals which are homologues of methyl (CH_3) and whose sole fate is to react with oxygen to form organic peroxy radicals through reactions of the form (2):

$$CH_3 + O_2 + M = CH_3O_2 + M. \qquad (2).$$

A further class of radicals which have been neglected are those oxy-radicals which react only with oxygen and have no other competitive routes. Such radicals are typified by the straight-chain alkoxy radicals, of which methoxy (CH_3O) is the simplest example:

$$CH_3O + O_2 = HO_2 + HCHO.$$

This principal simplification has been applied where possible throughout the mechanism and the composite and simplified reactions are presented in Table 2. Further simplifications have been applied to the assumed degradation schemes for isoprene and dimethyl sulphide and these are discussed further in the paragraphs below.

The current values of the rate coefficients, including their temperature- and pressure-dependences were calculated for each air parcel at the start of each chemistry time-step from the instantaneous location and pressure, temperature and specific humidity data.

Fast Photochemistry

The fast photochemistry of the sunlit troposphere has been described by the 28 chemical reactions listed in Table 2. These comprise the reactions of the odd-oxygen species: O and O_3, those of the hydrogen species: OH, HO_2, H_2, H_2O and H_2O_2, those of the NO_y species: NO, NO_2, HNO_3, HO_2NO_2 and of carbon monoxide. Together, these reactions set up the steady state concentrations of the highly reactive hydroxyl (OH) and hydroperoxy radicals (HO_2) and provide the main mechanism for the control of ozone production and destruction. The

bulk of these processes were identified by Levy (1971) and by Crutzen (1974) though over the subsequent years there have been many significant changes to the evaluated rate coefficient data for them.

The main OH and HO_2 free radical sources are photochemical in origin, through the solar photolysis of ozone and formaldehyde:

$O_3 + (\lambda < 317.5\ nm) = O^1D + O_2$

$O^1D + H_2O = OH + OH$

$HCHO + (\lambda < 360\ nm) = H + HCO$

$HCO + O_2 = HO_2 + CO$

The main OH to HO_2 free radical interconversion processes are:

$OH + CO = HO_2 + CO_2$

$OH + O_3 = HO_2 + O_2$,

and those which interconvert HO_2 to OH are:

$HO_2 + O_3 = OH + O_2 + O_2$

$HO_2 + NO = OH + NO_2$.

The representation of these two sets of processes in the three-dimensional model is relatively straightforward, however, care has been taken to treat the pressure-dependence of the of the OH + CO reactions in the required detail since this process is of dominating importance throughout the troposphere.

The main reactions controlling the destruction of the OH and HO_2 free radicals are:

$OH + HO_2 = H_2O + O_2$

$OH + NO_2 + M = HNO_3 + M$

$HO_2 + HO_2 + M = H_2O_2 + O_2 + M$

These two latter reactions show important pressure and temperature dependences throughout the troposphere which were represented using a detailed formulation of the fall-off behaviour, together with the evaluated third order low-pressure limiting rate coefficients and the second order high-pressure limiting rate coefficients. In addition, the $HO_2 + HO_2 + M$ reaction shows a significant water vapour catalysis which is both temperature and pressure dependent.

Methane Chemistry

The reaction of hydroxyl radicals with methane (CH_4) is the main initiating step in the degradation and removal of methane, making it one of the most important chemical processes in the sunlit troposphere. In addition, this process generates methyl peroxy radicals which through their reaction with nitric oxide, lead to ozone production. The OH + CH_4 reaction also generates a number of oxygenated species, including formaldehyde (HCHO), methyl hydroperoxide (CH_3OOH) and methyl alcohol (CH_3OH). Formaldehyde, itself, is photochemically-labile and is an important source of both free radicals and hydrogen. Methyl hydroperoxide is an important oxidising agent which accompanies hydrogen peroxide (H_2O_2) in most regions of the troposphere.

The accurate representation of the chemistry of the methyl peroxy radicals requires the detailed treatment of a number of temperature- and pressure-dependent competitive reactions, involving self reactions and reactions with NO, HO_2 and other organic peroxy radicals. The detailed chemical kinetic data for these reactions have only recently become available with the accuracy and reliability required to evaluate their importance in tropospheric models. This matter is given further attention in due course.

Chemistry of the Higher Hydrocarbons

STOCHEM includes a range of higher hydrocarbons and their atmospheric degradation pathways with a view to fulfilling a number of requirements. The role played by the higher hydrocarbons in the tropospheric ozone budget is still not resolved according to the IPCC (1996) scientific assessment. Organic nitrogen compounds such as peroxyacetylnitrate ($CH_3COO_2NO_2$: PAN) can potentially act as important carriers of NO_x out of the more polluted atmosphere into the free troposphere. To represent PAN adequately then all significant PAN sources need to be addressed. This means treating both natural and man-made PAN precursor hydrocarbons including isoprene, ethane, propane and the aromatic hydrocarbons.

The most important reason for including an adequate representation of the higher hydrocarbons comes from the requirement to represent the importance of the different ozone sources. STOCHEM aims to represent a comprehensive range of ozone sources, including man-made ground level photochemical smog over the polluted northern hemisphere continents, photochemical ozone formation from the natural biogenic isoprene emitted by tropical and sub-tropical vegetation and ozone formation in biomass burning plumes from tropical and sub-tropical vegetation systems in Africa and South America. The purpose of the 3-D model study is to achieve an adequate representation of the importance of each of these three main ozone sources. This is not straightforward because of the complexities and uncertainties in the chemistry of the hydrocarbons involved and the uncertainties of the hydrocarbon emissions from each of these sources, their seasonal and spatial distributions, their species composition profiles and the chemical environment in which they

occur with respect to the simultaneous emissions of other trace gases such as NO_x, CO and methane.

The following hydrocarbons have therefore been included:

* ethane, because of its low reactivity, its association with both natural sources and natural gas leakage and the widespread availability of surface measurement data, including seasonal variations.

* propane, because it is a major precursor of acetone, a widely distributed oxygenated hydrocarbon, and of PAN.

* butane, this is a major component of man-made hydrocarbon emissions from the industrial regions over the northern hemisphere continents, where its concentrations are widely measured.

* ethylene, this appears to have both man-made sources over the northern hemisphere continents and natural sources in the oceans.

* propylene, is a major source of ground level ozone in man-made photochemical smog episodes.

* isoprene, this is the major natural biogenic hydrocarbon which shows high reactivity during the daylight with OH and with ozone and NO_3 radicals during nighttime. Isoprene is the major precursor for the unsaturated carbonyl compounds such as methyl vinyl ketone and methacrolein and also has some man-made sources from pollution sources.

* toluene together with o-xylene, are major man-made hydrocarbons which account for a significant fraction between them of the ozone and PAN produced in ground level photochemical episodes. Dicarbonyl compounds such as methyl glyoxal (CH_3COCOH) and glyoxal (HCOCOH) appear to be major degradation products of the aromatic hydrocarbons. In addition, aromatic hydrocarbon degradation appears to lead to the formation low volatility organic nitrogen compounds which may lead to aerosol formation.

Few of the reaction steps in the assumed degradation pathways of the higher hydrocarbons have been studied individually under laboratory conditions. However, for the steps after the initial attack by OH radicals where accurate rate coefficient data are essential, relative rate coefficient may well suffice if sufficient information is available about the competition between the many different reaction pathways. Furthermore, structure-activity relationships have been developed for a wide range of different organic free radical reactions to extend the applicability of those reaction kinetic studies which have been completed to a wider spectrum of organic radicals species. The chemical mechanism used in STOCHEM has been derived from a Master Chemical Mechanism containing 7100 chemical reactions and 2492 chemical species, describing the degradation of 120 emitted hydrocarbons (Jenkin et al. 1997).

Chemistry of the Simple Sulphur Compounds

The global sulphur cycle has two main precursors: dimethyl sulphide (DMS) which is largely of natural origins and emitted by soils, vegetation and the oceans; and, sulphur dioxide (SO_2) which is largely emitted by human activities in the northern hemisphere continental areas, although volcanoes are an additional natural source.

The gas-phase chemistry of sulphur dioxide is relatively simple being dominated by oxidation by hydroxyl radicals to produce sulphur trioxide (SO_3) whose main fate is to react with water vapour to produce sulphuric acid (H_2SO_4). The reactions involved are:

$$OH + SO_2 + M = HOSO_2 + M$$

$$HOSO_2 + O_2 = HO_2 + SO_3$$

$$SO_3 + H_2O = H_2SO_4.$$

Only the first step has been included in the chemical mechanism since there does not appear to be any other competitive routes for either of the $HOSO_2$ radical or sulphur trioxide under tropospheric conditions.

In contrast, the chemistry of dimethyl sulphide is much more complex and a complete representation is beyond current computer capacity to represent completely. Nevertheless, the DMS oxidation scheme is thought to contain a number of important features which are considered important enough to retain in STOCHEM. One of the motivations for including the natural sulphur cycle is the accurate representation of the formation of cloud condensation nuclei over remote marine areas. The DMS chemistry is thought to be temperature dependent and to be heavily influenced by the presence of trace concentrations of NOx and ozone. These temperature and pollution effects may have important consequences for climate change prediction and this limits the simplifications that can be made with the DMS chemistry. A review was therefore commissioned of current understanding of the atmospheric and laboratory chemistry of DMS (Jenkin et al. 1996) from which the mechanism in Table 2 was assembled. Simple sensitivity runs demonstrated that the mechanism had the required temperature and pollution dependences (Jenkin et al. 1996). The main products of the atmospheric degradation of DMS appeared to be sulphur dioxide, sulphuric acid aerosol, dimethyl sulphone ($DMSO_2$) and methane sulphonic acid (CH_3SO_3H).

Cloud chemistry

It has been recognised for some time that aqueous-phase chemistry is important for some tropospheric species, in particular, for the oxidation of sulphur dioxide (SO_2) to form sulphate aerosols (Langner and Rodhe 1991). The incorporation of soluble species into cloud droplets is quite rapid (Warneck

1988) and is treated as an equilibrium process here. The gaseous species which are dissolved into the cloud water are nitric acid (HNO_3), ozone (O_3), carbon dioxide (CO_2), hydrogen peroxide (H_2O_2) and ammonia (NH_3). The aqueous-phase equilibria treated in the model are:

$H_2O = H^+ + OH^-$

$HNO_3 = H^+ + NO3^-$

$SO_2 = H^+ + HSO_3^-$

$HSO_3^- = H^+ + SO_3^{2-}$

$NH_3 = OH^- + NH_4^+$

$CO_2 = H^+ + HCO_3^-$

The hydrogen ion concentration in the clouds can then be calculated iteratively so that the pH-dependant species concentraitons can be determined. This treatment ignores the contributions made by organic acids or by alkaline aerosols generated as wind-blown dust.

The production of sulphate aerosol is treated by the reactions:

$HSO_3^- + H_2O_2 = SO_4^{2-} + H^+ + H_2O$

$HSO_3^- + O_3 = SO_4^{2-} + H^+ + O_2$

$SO_3^{2-} + O_3 = SO_4^{2-} + O_2$

Photochemical processes

The photochemical reactions that are included in our 3-D Lagrangian tropospheric chemistry model are described using a photolysis rate, or J-value, for a species which is the product of the spherically-integrated actinic flux, with the absorption cross-section and the quantum yield, integrated over all wavelengths. The quantum yield is taken to be the probability of the species dissociating after absorbing a photon. In practice, the integral is restricted to the range in which the integrand is significant and the integral itself is replaced by a sum over wavelength intervals. The cross-sections and quantum yields for the reactions have been obtained from published evaluations (DeMore et al. 1997).

The actinic flux is affected by a large number of factors. The solar flux incident on the atmosphere is attenuated by ozone and molecular oxygen absorption. The remaining flux reaching the troposphere is scattered by aerosols, clouds and atmospheric molecules and is reflected by the earth's surface. Thus the light incident on any air parcel has arrived by many different and tortuous

paths. The algorithm used to calculate the spherically integrated solar flux is an adaptation of the one-dimensional two stream model (upward and downward fluxes) developed by Hough (1988).

Parameterising the photolysis results for the 3-D chemistry model

Ideally we would like to be able to calculate the flux exactly but to do this for the 50,000 air parcels for every 5 minute timestep would be prohibitive in terms of computing time. We are fortunate that most of the variables on which the photolysis rates depend only vary slowly with time. The factors that affect the photolysis rates are;

solar flux,
aerosol content,
stratospheric oxygen and ozone columns,
tropospheric oxygen and ozone profiles,
surface albedo,
cloud cover,
height above surface,
and solar zenith angle (secant theta).

Of these, only the solar zenith angle and the cloud cover vary on a diurnal basis; the rest have a characteristic timescale of a year. Values of secant theta are calculated for each air parcel at every chemical time step from its latitude, longitude and time of day because the photolysis rates have a very strong dependence on solar zenith angle.

A 72x36 grid (5° x 5°) on nine levels spaced by $\Delta\acute{\eta}$ =0.1 is used when calculating the J-values as described above. For each grid square, the J-value for each reaction and for each level is recalculated every 45 minutes, taking into account the stratospheric ozone column, the surface albedo, the cloud cover and the variation of solar zenith angle with time of day. The aerosol and oxygen profiles are global averages fixed for all grid squares and are taken from Hough (1988). The stratospheric ozone is taken from a monthly 2-D climatology. The tropospheric ozone profile is calculated within the model. We have used the parameterisation from Hough (1988) to calculate the surface albedo. Photolysis rates for each time-step are obtained by interpolation in time between the appropriate values stored from the recalculation at intervals of 45 minutes.

The cloud data are taken from the Meteorological Office UM operational model as 6-hour snapshot values for high, medium, low and convective cloud. These are converted to physically thin (but may be optically thick), partially scattering layers in a 5° x 5° x $\Delta\acute{\eta}$=0.1 level array.

Emissions in the Present-Day Atmosphere

Emissions into the model are implemented as an additional term in the production flux for each species during each integration time-step. The

emissions used are listed in Table 3. The anthropogenic, biomass burning, vegetation, soil, oceans and 'other' are all surface sources based on two-dimensional (latitude, longitude) source maps. Stratospheric sources of ozone and nitric acid are calculated as two-dimensional inputs into the top model layer. The aircraft and lightning NO_x sources are three-dimensional. We use the term 'anthropogenic' in this paper to describe direct emissions from fossil fuel combustion, although man will also have a large influence on biomass burning and (through farming) on vegetation, paddies and animal sources. Aircraft are not included in the 'anthropogenic' emissions but are treated separately. The anthropogenic, paddy, tundra, wetland and 'other animal' sources (see Table 3) are held constant throughout the year at the yearly average value. The other sources vary by calendar month.

The methane emissions in Table 3 were based on the IPCC (1995) assessment which provided for a total source strength of 485 Tg yr^{-1}. The spatial distributions of the oceans, tundra and wetland sources were estimated from the corresponding distributions of biospheric zones (Olson and Watts 1982); anthropogenic sources were given the same distribution as NO_x emissions (Benkovitz et al. 1995) and biomass burning as that of SO_2 from the same source (Spiro et al. 1992). Global hydrocarbon emissions from vegetation sources were taken from (Hough 1991) and were distributed in space and time as for dimethyl sulphide from the corresponding soil and vegetation sources (Spiro et al. 1992). Soil NO_x emissions were taken from Yienger et al. (1995).

The entries in Table 3 for carbon monoxide are based on the literature review by Warneck (1988). Biomass burning and human activities, mainly the exhausts of petrol-engined vehicles, are the largest contributors. This table does not account for the carbon monoxide produced by hydrocarbon oxidation which our study shows to be a somewhat larger secondary source than any of the direct primary emissions. The spatial distribution of the anthropogenic sources were taken to be the same as that for NO_x (Benkovitz et al. 1995). All biomass burning sources were given the same spatial distribution which was taken from Spiro et al. (1992).

The principle source of the oxides of nitrogen is fossil fuel combustion and Table 3 reflects this situation (Logan 1983; Dignon and Hameed 1989). The spatial distribution was taken directly from Benkovitz et al. (1995). Although SO_2 gas-phase chemistry has little or no effect on ozone production, it does exert an influence on the lifetime and removal rate of hydrogen peroxide. We have included ammonia and DMS emissions and a DMS oxidation scheme so both the natural and human-influenced sulphur cycles are treated in some detail.

In our model, surface emissions are added on a 5° x 5° grid square basis. This is too coarse (600 km x 400 km at mid-latitudes) to resolve individual centres of pollution but is large enough to give an average cell occupancy of approximately two Lagrangian cells within the boundary layer per grid square in the mid-latitudes. After each advection timestep the surface emissions for a grid

square are distributed equally over all the Lagrangian cells that are within the boundary layer in that grid square. If there are no cells within the boundary layer for a particular emissions grid square then those emissions are stored until a cell does pass through.

Isoprene is emitted by vegetation during the day, with its emission rate being positively correlated with temperature (Jacob and Wofsy 1988). In our model we use the simple approach of emitting isoprene at a rate proportional to the cosine of the solar zenith angle during the day, with no emission at night. The rate is adjusted to give the appropriate total emission over a month for each grid square. These monthly emissions were taken from Guenther et al. (1995).

Lightning is an important NO_x source in the free troposphere (Turman and Edgar 1982; Franzblau and Popp 1989). We used a parameterisation from Price and Rind (1992) based on model-simulated monthly two-dimensional fields of convective cloud top heights. The emissions were distributed evenly by mass in the vertical between the ground and the convective cloud tops. The total was normalised to give a yearly emission of 5 Tg N yr^{-1}, emitted as NO. In comparison, Strand and Hov (1994) suggest a total of 8 Tg N yr^{-1} emitted in the regions of outflow from thunderclouds rather than distributed evenly in the vertical. The lightning emissions are calculated on a 5° x 5° x $\Delta\acute{\eta}$=0.1 grid. If there are no Lagrangian cells within an emissions grid volume then the emissions in other grid volumes are increased to give the correct global emission every timestep. For the NO_x emissions from civil and military aircraft three-dimensional emissions fields were used (Stevenson et al. 1997) which amounted to 0.85 Tg N yr^{-1} globally. These emissions have been assembled into the model using the same procedure as for lightning.

The cells in our model are constrained to remain below 100 hPa by imposing a fixed lid to the model. In reality, they would travel to and from the stratosphere bringing high ozone and NO_y concentrations down to the troposphere and losing species into the stratosphere. Murphy and Fahey (1994) estimate an ozone flux of 450 Tg yr^{-1} from the stratosphere and an NO_y (NO_y = $NO + NO_2 + HNO_3 + PAN + 2N_2O_5$) flux of 0.45 Tg N yr^{-1}. The upper boundary of our model is set at eta =0.1, (100 hPa) and so the vertical windfields are used to calculate an ozone flux across the $\acute{\eta}$ =0.1 surface on a 5° x 5° grid. We neglect any loss in species due to upwards transport into the stratosphere. Monthly zonal mean ozone fields are taken from Li and Shine (1995) and are interpolated to give the ozone mass mixing ratio at 98.5 hPa, which is used to calculate the stratospheric flux. This pressure level was chosen as it gives a total ozone flux of 650 Tg over one year. The NO_y flux is taken to be one thousandth of the ozone flux by mass (as N) and is emitted into the model as HNO_3. The emissions are calculated on a 5° x 5° grid and distributed equally between all Lagrangian cells that are within a grid square and have $\acute{\eta}$ values between 0.2 and 0.1. As with the surface emissions, if there are no Lagrangian cells in which to distribute the emissions, then the emissions are stored.

Emissions for the Scenario Cases Studied for the Year 2015

In the paragraphs above, the emissions have been described in some detail for the 1992 base case. Model results have been obtained for three scenario cases which aim to address the future situation in the year 2015 or thereabouts. The changes in the model output in these runs have largely been driven by changes in the total global emissions, rather in their spatial distribution or composition. Emissions from fuel combustion, biomass burning and from agriculture have been increased, loosely following a business-as-usual scenario, the IS92a case of the IPCC (1992). Table 3 compares the emissions assumed for 1992 and 2015 for the trace gases: methane, carbon monoxide, VOCs, SO_2 and NO_x. Lightning and stratospheric sources have been left unchanged but aircraft NOx emissions increase by a factor of 2.5 or so.

The three 2015 scenario cases differ in their treatments of the North American and European SO_2 and NO_x emissions from fuel combustion. The 2015-IS92a scenario has SO_2 and NO_x emissions from fuel combustion in the UN ECE region increasing by 35 and 45%, respectively, by the year 2010 or thereabouts. In the 2015-CRP scenario, North American SO_2 and NO_x emissions in 2010 fall to about 72% (28% reduction) and 95% (5% reduction) of the 1992 emissions (United Nations 1997). European SO_2 and NO_x emissions in 2010 fall to about 60% (40% reduction) and 79% (21% reduction), respectively, following the introduction of pollution control systems to combat acid rain (United Nations 1997). Emissions of carbon monoxide in North America fall to 92% (8% reduction) of their 1992 values and by 50% in Europe.

In the 2015-MFR scenario, SO_2 and NO_x emissions fall even further relative to their 1992 values. North American SO_2 and NO_x emissions are assumed in this illustrative scenario for 2010, to fall to about 27% (73% reduction) and 95% (5% reduction) of the 1992 emissions (United Nations 1997). European SO_2 and NO_x emissions in 2010, on the other hand, are assumed to fall to about 2% (98% reduction) and 40% (60% reduction), respectively, following the introduction of strict pollution control measures in Europe to combat acid rain. Globally SO_2 emissions from human activities fall to about 20% (80% reduction) of their 1992 values to reflect global concerns about acidification and climate change. The NO_x control measures in the illustrative 2015-MFR scenario were developed from the integrated assessment modelling studies of IIASA (Amann et al. 1997).

Dry Deposition

For all cells within the boundary layer the species loss flux due to dry deposition is calculated to be [c] x V_d /H where [c] is the species concentration, V_d is the species-dependant deposition velocity and H is the height of the boundary layer. The deposition velocity, V_d, depends on the location of the cell, according to whether the cell is over land or ocean. Deposition velocities are taken from Hough (1991) and are tabulated in Table 4. This simple parametrisation of dry deposition could be extended to include differences

between tundra, forest, desert etc. At present there is no parameterisation of ice cover. The sea ice and Antarctica are classified as 'ocean', and all other land ice is classified as 'land'. The deposition velocities are for a height of 1 metre and are chosen specifically for the purposes of global-scale modelling. If we assume that species concentrations at 50 metres are representative of those throughout the mixed boundary layer then we can convert the deposition velocities at 1 metre to give values at 50 metres, allowing for aerodynamic resistance using:

$$1 / V_{50} = 1 / V_1 + 50 / K_z$$

where V_{50} is the deposition velocity at 50 metres, V_d is the deposition velocity at 1 metre and K_z is the effective vertical eddy diffusion coefficient in $m^2 s^{-1}$ between 1 metre and 50 metres. K_z is calculated from the Unified Model heat flux, surface temperature and surface stress using Monin-Obukhov scaling.

Wet Deposition

The aqueous phase deposition of the following soluble species is treated in STOCHEM:
* formaldehyde (HCHO),
* nitric acid (HNO_3 and nitrogen pentoxide (N_2O_5),
* hydrogen peroxides (H_2O_2) and the organic hydroperoxides (ROOH), and
* sulphur dioxide (SO_2).

Scavenging coefficients for large-scale and convective precipitation were adopted from Penner et al. (1994) and the scheme to convert fractional scavenging rates to grid cell average rates follows the scheme of Walton et al. (1988).

Model output

Although the model itself is Lagrangian, the most useful way to visualise the output is as concentrations on a regular grid. The chosen output grid was 5° x 5° x $\Delta\acute{\eta}$ = 0.1, as used in the emissions and for inter-parcel exchange. The species concentration in each 3-D grid box is taken to be the average of all the cells in that box. To smooth out the distributions near the poles and to fill in holes where there are no cells in a grid box, the grid is convolved with a 2-dimensional (longitude-latitude) Gaussian filter with a constant width of 200 km.

As well as the species concentrations it is often useful to see the fluxes through particular reactions. The average flux per cell within each grid box divided by the volume of a cell at a height corresponding to the middle of the box gives the volume-averaged reaction flux in molecule $cm^{-3} s^{-1}$.

Initial concentrations

The initial methane concentrations were established from the mid-1992 values from the NOAA-CMDL flask sampling network (Dlugokencky et al. 1994). The initial concentrations for 2015 for the tropospheric source gases were uplifted from their 1992 values in proportion to the increase in emissions in the scenario. Initial concentrations for carbon monoxide were established from the latitudinal cross-section of surface carbon monoxide measurements reviewed by Derwent et al. (1994). The initial ozone concentrations were taken from an altitude-latitude climatology calculated from a previous model experiment

Numerical Methods

The time-development of the volume mixing ratio of a trace gas, c_i, in a particular air parcel was represented in STOCHEM by the differential equation:

$$dc_i / dt = E_i + P_i - L_i c_i - v_i c_i / h - w_i c_i - M_i$$

where:
* E_i is the instantaneous emission rate of the species, should the air parcel be in the atmospheric boundary layer,
* P_i is the local rate of chemical production of the species,
* L_i is the local rate coefficient for chemical destruction,
* v_i is the species-dependent dry deposition velocity, should the air parcel be in the atmospheric boundary layer,
* w_i is the species-dependent wet scavenging loss coefficient, should the air parcel be in cloud, and
* M_i is the loss of material by inter-parcel exchange.

In all, the 70 x 50 000 = 3 500 000 simultaneous, initial-valued differential equations were solved using a backwards-Euler iterative numerical procedure due to Hertel et al. (1993), with a time-step (DTS) of five minutes and eight iterations per time-step. The numerical formula which relates the mixing ratio at the end of the step, Y^{t+dt}, to that at the start, Y^{t}, takes the form:

$$Y_i^{t+dt} = (Y_i^{t} + DTS * P_i) / (1 + DTS * L_i)$$

The STOCHEM model took 1 hour of CPU time on the Met Office CRAY C90 to run about 2 days of model experiment and each scenario case required a model experiment which covered at least 15 months in model time. Each model experiment used a database of analysed meteorological data which began on 1st June 1995 and extended until at least 31st August 1996. All model results were taken from the last complete 12 month period from 1st September 1995 to 31st August 1996, inclusive.

3. Some Model Results for the Global Atmosphere

The model experiments described in this study, were started up from the assumed initial composition of the troposphere during June of the first model year and were run through to the Autumn of the next model year. All model concentrations were generated by the processes within the model without intervention, flux adjustment or the operation of fixed concentrations at any of the model boundaries. Initial conditions were set for methane, ozone and carbon monoxide but only those set for methane had a significant influence on the model atmospheric composition after more than 2-3 months into the model experiments.

Global Free Radical Budgets

The central governing species in the STOCHEM model experiments is the hydroxyl (OH) radical. Figure 1a shows the distribution of OH calculated for July 1992, expressed as a monthly mean mixing ratio for the model layer closest to the surface at $\acute{\eta}$=0.95 corresponding to an approximate altitude of 550 metres, midway up the daytime atmospheric boundary layer. Monthly averaging smooths out the time-of-day variations in OH, leaving a distribution which appears zonal (constant around latitude circles) and showing a marked contrast between the summer and winter hemispheres. Local monthly mean OH mixing ratios reach 0.5 ppt (corresponding to an OH concentration of about 1.25×10^7 molecule cm^{-3}) with a global mean surface layer mixing ratio of 0.056 ppt (1.4×10^6 molecule cm^{-3}). OH concentrations tend to be higher over the northern hemisphere continents, reflecting the influence of NO_x sources which are largely land-based. The influence of the large natural biogenic emissions of isoprene from the forested regions of South America and West Africa can be clearly seen in the depressed OH mixing ratios in these areas.

Because of the extremely low mixing ratios of tropospheric hydroxyl radicals and because of its high chemical reactivity, there are no global scale observations with which to compare these model calculated concentrations. However, indirect techniques have been applied to the estimation of the globally-averaged mean tropospheric hydroxyl radical concentration and some of these estimates are gathered together in Table 4. Also shown is the mean tropospheric OH concentration calculated by spatially averaging the STOCHEM model results over all seasons, day and night, pole-to-pole and throughout the depth of the troposphere. The mean tropospheric hydroxyl radical concentration calculated here is well within the range of the different estimates.

As the emissions of the main tropospheric source gases which control the OH budget steadily increase from 1992 to 2015 in the IS92a business-as-usual scenario, the OH concentrations respond as shown in Figures 1b and c. The global mean surface OH mixing ratio increases only slightly from 0.056 to 0.057 ppt, that is by just under 1%. That this change is relatively small compared with the changes in the levels of the tropospheric source gases, reflects their

opposing influences on OH. Increases in methane and carbon monoxide concentrations tend to reduce OH through the reactions:

$OH + CH_4 = CH_3 + H_2O$

$OH + CO = H + CO_2$

where increases in NO_x concentrations tend to increase OH through:

$HO_2 + NO = OH + NO_2$

and decrease OH through:

$OH + NO_2 + M = HNO_3 + M$.

Because of the short lifetime of NO_x and because its main sources are continental, there is a large difference in the concentration ratio of HO_2 to OH in remote marine environments compared with polluted continental environments.

The largest differences in the surface layer OH mixing ratios between 1992 and 2015 reach about 0.05 ppt and are located over the northern hemisphere continents. There also appears to be a region with depressed rather than increased OH levels over North West Europe. This changeover from increased to decreased OH presumably results from opposing influences of NO and NO_2 on OH through the HO_2 + NO and OH + NO_2 reactions as indicated above. Strong NO_x inhibition of OH production is an important feature of regional scale photochemical ozone formation and so it is heartening to see its influence in the STOCHEM results. It is, however, surprising to see that its occurrence is not widespread throughout the other heavily-industrialised regions of the northern hemisphere. This may be a reflection of the coarse spatial resolution of the man-made NO_x emission inventory which may spread NO_x emissions over too large an area, reducing emission densities to below the level where NO_x inhibition of regional scale photochemical ozone is important.

The impacts of the trace gas increases on the free radical burdens and budgets are analysed in Table 5 for the entire model domain and for a complete year. The step-change in the methyl peroxy (CH_3O_2) and organic peroxy (RO_2) radical inventories between 1992 and the various 2015 scenarios is clearly evident in this table. The increases in global OH and HO_2 radical burdens are also evident, though they are much smaller than those in the organic peroxy radicals. The budget analyses shows that although it is helpful to see the influence of the changes in tropospheric source gases through the initial reactions of OH with CH_4 or CO and of HO_2 with NO as described in the paragraphs above, this is by no means their sole influence. Free radical production also increases through increased formaldehyde photolysis and there are necessarily compensating changes in free radical sinks to maintain the fast photochemical balance. Furthermore, a small increase in OH removal through

increased OH + NO_2 + M is also apparent, leading to the inhibition of photochemical ozone formation in the atmospheric boundary layer as noted above.

Global Methane Budgets

The methane life cycle is controlled by its sources and sinks, with hydroxyl radical oxidation providing the major sink. An important test of the accuracy and completeness of the STOCHEM model treatment of the fast tropospheric photochemistry is whether the model calculated methane lifetime agrees with literature estimates.

The STOCHEM model employs an initial methane distribution based on the mid-1992 concentrations from the NOAA-CMDL flask sampling network (Dlugokencky et al. 1994) and a total methane source strength of 485 Tg CH_4 yr^{-1}. The model methane burden then moves away from its initial distribution and may accumulate or dissipate over the 15-month model experiment, depending on the magnitude of the calculated tropospheric hydroxyl radical distribution.

In the atmosphere, methane has shown an annual increase in burden of 35-45 Tg yr^{-1} during the 1980s and somewhat smaller values throughout the 1990s. A turnover time of 8.7± 1.6 years has been estimated (IPCC 1996), of which tropospheric OH oxidation contributes a turnover time of 9.9 years, allowing for some small soil uptake and stratospheric loss processes.

Table 6 presents a budget analysis for methane in the different model experiments. The model methane turnover time is about 8.7 years which is close to the recommendation in the IPCC (1996) assessment. This turnover time changes only slightly between the model experiments, in agreement with the small changes detected in the mean tropospheric hydroxyl radical concentrations.

As a further test of the accuracy and completeness of the STOCHEM model treatment of the global methane life cycle, a separate model experiment was conducted following the procedures outlined in the Delta Methane model intercomparison (IPCC 1995). In this intercomparison experiment, a number of tropospheric models were used to estimate the change in methane oxidation rates for a step-change of 20% in global methane concentrations. An experiment was therefore performed with STOCHEM to define its response to a 20% increase in initial methane concentrations, from 1725 ppb to 2070 ppb. The annual removal coefficient in yr^{-1} for methane with hydroxyl radicals decreased by 4.1%, giving a decrease of -0.205% in removal coefficient per % change in methane concentrations. As Table 7 shows, this is well within the accepted range of model results in the Delta Methane intercomparison. It is also reassuringly close to the -0.20% value reported for the UK Meteorological Office 2-D tropospheric model TROPOS.

Global Ozone Budgets

Since pre-industrial times, tropospheric ozone levels are thought to have increased in the northern hemisphere as discussed in the introduction above. As the tropospheric source gases increase in concentration from 1992 through to 2015, the STOCHEM model predicts that the human influence on past ozone levels continues into the future. Figure 2a presents the distribution of ozone in the surface model layer in July 1992 and Figure 2b the corresponding distribution for 2015 in the IS92A case, with the difference plot in c). The monthly mean July surface ozone concentration increases from 32.76 to 35.67 ppb, representing an increase of about 9%. The increase is mainly in the northern hemisphere and over the continental areas.

In January, the surface ozone levels are lower over the continents of the northern hemisphere compared with the summertime levels because of lower photochemical production, see Figure 3a. The response to the increasing tropospheric source gases in 2015 changes sign in these regions and surface ozone levels decrease. In lower latitudes, an increase in surface ozone through to 2015 is still observed as found in Figure 2b and c for July. The January increase in surface ozone concentrations of 2.6 ppb is somewhat smaller in magnitude compared with the July increase and is in a different location, but it still nevertheless represents the same percentage change.

Both Figures 2a and 3a show evidence of a 'tongue' of ozone leaving the eastern seaboard of the north American continent and spreading across the North Atlantic Ocean towards the continent of Europe. The 'belt' of ozone stretches from Europe across the continental land mass and joins up with the ozone peaks over Asia. These features illustrate the long-range intercontinental scale of ozone formation and transport in the lower troposphere originally postulated by Parrish et al. (1993). They remain, clearly, in the corresponding plots for 2015, see Figures 2b and 3b.

To explain how the ozone levels have increased from 1992 through to 2015, the respective global ozone budgets are presented in Table 8. These budgets show that the increased ozone production required to sustain the higher ozone levels in 2015 compared with 1992 has come mainly from the increased reaction flux through $HO_2 + NO$. This flux has been driven up largely by increased CO oxidation, increased ozone photolysis, increased formaldehyde photolysis and increased availability of NO. The increased methane oxidation has not only increased the $CH_3O_2 + NO$ flux but has also produced extra HO_2 and CO which have contributed to the increased $HO_2 + NO$ flux.

The different 2015 scenario variants have different global ozone budgets, mainly because of changes to the $HO_2 + NO$ flux. The relatively subtle differences in regional NO_x emissions appear to have a clear global influence on the ozone budgets. In all the cases in Table 8, the ozone destruction processes readjust to the different ozone production terms and re-establish balanced budgets. The changes in the NO_x levels between the different 2015 scenario

variants exerts a small influence on the $O_3 + HO_2$ flux and prompt a small readjustment in the relative importance of the different destruction mechanisms.

Ozone lifetimes change only slightly from close to 21 days in the 1992 model experiment to 20.5-20.8 days in the 2015 model experiments. This relatively short lifetime, when taken with the relatively large atmospheric burden, means that ozone has one of the largest annual turnovers due to atmospheric chemical processes, of all the tropospheric trace gases.

Global Budgets of the other Tropospheric Oxidants

In addition to ozone, the troposphere contains a number of other oxidant species. These include the family of peroxyacylnitrates, of which peroxyacetylnitrate (PAN) is the best characterised. PAN is an important contributor to the oxidised nitrogen species, known collectively as NO_y. The other oxidants also include hydrogen peroxide (H_2O_2) and the organic hydroperoxides (ROOH), of which methyl hydroperoxide (CH_3OOH) is the first family member. Hydrogen peroxide plays an important role as the major oxidant for sulphur dioxide and the formation of acidified rain and snow.

In the polluted boundary layer, ozone and PAN are generally closely correlated in time, demonstrating their common photochemical source. Whereas almost all organic compounds show some propensity to form ozone on photochemical degradation in the presence of sunlight and NO_x, only certain organic compounds have the molecular structural frameworks which favour PAN formation. All photochemical PAN formation occurs through the reaction:

$$CH_3COO_2 + NO_2 + M = PAN + M$$

and so the production of the peroxyacetyl CH_3COO_2 radical is essential to PAN production.

The STOCHEM model demonstrates that there are several sources of the peroxyacetyl radical involving the photooxidation of certain organic compounds. Figure 4 illustrates the framework of interlinking reactions in STOCHEM which account for PAN production in the troposphere. Much of the PAN production in STOCHEM is derived from the photooxidation of isoprene from natural biogenic sources and of butane from human activites, see Table 9.

Surface PAN concentrations are highest over the continents and lowest over the ocean areas. In July, Figure 5a shows peak PAN concentrations exceeding 2 ppb over the polluted continental areas and minimum values close to 20-40 ppt over the remote southern oceans. The global mean surface PAN concentrations in July increase from 179 to 207 ppt from 1992 to 2015 in response to the changes in trace gas emissions, see Figure 5b. Any increase is almost entirely restricted to the polluted northern hemisphere continental regions, Figure 5c.

The global life cycle of hydrogen peroxide is dominated by photochemical production in the following reaction:

$HO_2 + HO_2 + M = H_2O_2 + O_2 + M$

and by removal in wet deposition, see Table 10. The main role of hydrogen peroxide is to act as a temporary reservoir for the HO_x radicals and 'catalyse' odd-hydrogen interconversion through its photolysis and reaction with OH:

$HO_2 + HO_2 + M = H_2O_2 + O_2 + M$

$H_2O_2 + (200nm < \lambda < 300nm) = OH + OH$

$HO_2 + HO_2 = OH + OH$

$HO_2 + HO_2 + M = H_2O_2 + O_2 + M$

$OH + H_2O_2 = H_2O + HO_2$

$OH + HO_2 = H_2O + O_2$

The oxidation of SO_2 in cloud droplets, see Table 10, though important in the life cycle of SO_2 and for the formation of acidifying substances, nevertheless is only a small part of the global budget of hydrogen peroxide. This is because of the order of magnitude disparity between the global flux forming hydrogen peroxide which is close to 1000 Tg yr^{-1} and the SO_2 emission source strength which is close to 100 Tg S yr^{-1}.

Surface hydrogen peroxide concentrations are highest over the continents and lowest over the ocean areas. In July, Figure 6a shows peak hydrogen peroxide concentrations exceeding 1 ppb over the polluted continental areas, approaching 10 ppb over Amazonia and minimum values below 300 ppt over the remote southern oceans. The global mean surface hydrogen peroxide concentrations in July increase from 899 to 952 ppt from 1992 to 2015 in response to the changes in trace gas emissions, see Figure 6b. The increase is restricted to the sub-tropical regions over the major continental regions, Figure 6c. Over the highly polluted industrial regions of the northern hemisphere continents, local concentrations decrease because of the competition between the reactions $NO+HO_2$ and HO_2+HO_2.

Global Sulphur Deposition Budgets

The pre-industrial global sulphur cycle was dominated by fate and behaviour of natural dimethyl sulphide (DMS) which is emitted from the decay of plankton in the surface layers of the oceans and carbonyl sulphide (COS) from biomass burning. Sulphur dioxide (SO_2) emissions from coal and oil burning have increased dramatically during the 20th century and at some point, have

overtaken the natural sources on the global scale. SO_2 is converted into sulphuric acid and then to ammonium sulphate aerosol by photochemical reactions involving the OH radical and by oxidation in cloud droplets involving hydrogen peroxide, ozone and ammonia. DMS is also oxidised by OH radicals but its degradation routes are relatively more complex than of SO_2 and generate a variety of oxidation products including dimethyl sulphone, methane sulphonic acid, sulphur dioxide and sulphate aerosol.

Because of the different physical and chemical properties of the different sulphur compounds and their oxidation products, they all differ in their subsequent atmospheric removal processes and lifetimes. Dry deposition is an efficient process for SO_2, but is a relatively inefficient process for aerosol species, see Table 11. By contrast, wet scavenging tends to be quite efficient for aerosols compared with gases as shown in Table 12, although its general importance is limited by the sporadic nature of precipitation. Dry deposition can occur under all weather conditions but it can only operate on material within the atmospheric boundary layer. These differences turn out to exert major limitations on the fates and behaviour of the different sulphur compounds and hence on the processes which control the global sulphur budgets and lifetimes.

Dry deposition of SO_2 is a major driving process in the regional scale acid rain problems of North America and Europe. Figure 7 plots the global scale spatial pattern of the model dry deposition flux of SO_2 for 1992 emissions in the context of the global deposition fluxes for all components of the global sulphur cycle. There are significant differences between the hemispheres with the largest fluxes over North America and Europe. Dry deposition fluxes exceed 1 g S m^{-2} yr^{-1} over the industrialised continents and fall to below 10 mg S m^{-2} yr^{-1} over the southern oceans. These calculated deposition fluxes are well within the range observed in the various global acid deposition networks. Further detailed comparisons with the European dry deposition observations are provided in a later section.

The wet deposition of sulphur compounds occurs when the sulphur compounds enter clouds and act as nuclei for the formation of cloud droplets which are subsequently scavenged within the cloud by falling rain droplets. Some wet deposition also occurs by the scavenging of water soluble compounds by falling rain droplets below the cloud base. Some of the wet deposition of sulphur compounds will therefore occur by the nucleation scavenging of sulphuric acid and ammonium sulphate and by the below-cloud washout of sulphur dioxide. The role of ammonia is vital here because it is the major alkaline species in the atmosphere and so acts to control the acidity of cloud droplets and hence the oxidation rate of sulphur dioxide.

The model calculated global distributions of the wet deposition of sulphuric acid and ammonium sulphate are also shown in Figure 7, and are similar both in magnitude and spatial distribution. It appears that the wet removal of ammonium sulphate is approximately one half that of sulphuric acid and this is

similar proportion to that seen in the observations in the global deposition networks. In a later section, the model wet deposition fields for sulphate and ammonium will be carefully compared with the European wet deposition observations. Wet sulphur deposition fluxes exceed 200 mg S m^{-2} yr^{-1} over the polluted continents and fall to below 50 mg S m^{-2} yr^{-1} and below, over the southern oceans. Observed wet sulphur deposition over the continents ranges from 500-1000 mg S m^{-2} yr^{-1} and 60-120 mg S m^{-2} yr^{-1} over the remote oceans (Whelpdale and Kaiser, 1996), providing excellent confirmation of the model results.

Of the sulphur emitted globally from both natural biogenic and human activities, 36% is returned to the earth's surface as dry deposition and 64% as wet deposition in the STOCHEM model. The corresponding percentages of global sulphur emissions returned by dry deposition in other global chemistry-transport models are 41% (Langner and Rodhe 1991), 43% (Pham et al. 1995), 47% (Feichter et al. 1996) and 33% (Chin et al. 1996). The present model is therefore giving global dry and wet sulphur deposition fluxes in agreement with the relative proportions shown in a number of other global model studies.

Global Oxidised Nitrogen Deposition Budgets

Understanding of the wet removal of atmospheric nitrogen compounds is not as advanced as that for the sulphur compounds because of major analytical problems involved with the observation and detection of the nitrogen compounds involved. Much of the NO_x =NO+NO_2 emitted into the atmosphere is rapidly converted into nitric acid by reaction with OH radicals:

$$OH + NO_2 + M = HNO_3 + M$$

However, nitric acid itself is readily dry deposited. Nitric acid is exceedingly difficult to measure reliably and few datasets are available globally. The available measurements suggest strongly that there is not enough nitric acid to account for much of the observed nitrate in rain over Europe. Nitrate aerosol can readily account for the observed levels of nitrate in rain but there would need to be efficient routes for its formation from NO_x which did not necessarily have to involve nitric acid as an intermediate precursor. The mechanisms thought to account for the conversion of NO_x into nitrate aerosol involve the participation of the ubiquitous sea-salt aerosol and include:

$$NO_2 + O_3 = NO_3 + O_2$$

$$NO_3 + NO_2 + M = N_2O_5 + M$$

$$N_2O_5 + 2NaCl + H_2O = 2NaNO_3 + 2HCl$$

or the formation of ammonium nitrate aerosol and sodium nitrate aerosol through nitric acid:

$N_2O_5 + H_2O = 2HNO_3$

$NH_3 + HNO_3 = NH_4NO_3$

$HNO_3 + NaCl = NaNO_3 + HCl$.

The sodium and ammonium nitrate aerosols are then removed by the nucleation scavenging route in clouds and are deposited to the ground in rain. The collective term for all the oxidised nitrogen trace gas species is NO_y = $NO+NO_2+PAN+HNO_3$+nitrate aerosol.

Much of this detailed chemistry is included in STOCHEM and the resulting global deposition fields for the oxidised nitrogen NO_y species are shown in Figure 8 for 1992 emissions. Global NO_y deposition is dominated by the contribution from wet deposition which accounts for 72% of the total. The largest single term in the global deposition budget is the wet deposition of nitrate aerosol which accounts for 54% of total deposition. Dry and wet deposition of nitric acid appear to have similar magnitudes and together account for an additional 32% of total deposition.

The nitrate wet deposition levels are significantly higher over the northern hemisphere continents compared with the southern hemisphere oceans. Peak continental values approach 200 mg N m^{-2} yr^{-1} and lowest oceanic values are below 30 mg N m^{-2} yr^{-1}. Observed wet nitrate deposition over the continents ranges from 150-400 mg N m^{-2} yr^{-1} and 15-60 mg N m^{-2} yr^{-1} over the remote oceans (Whelpdale and Kaiser, 1996), providing good confirmation of the model results.

Global Reduced Nitrogen Deposition Budgets

Ammonia, NH_3, is the most important alkaline gas in the atmosphere and is emitted almost entirely from soils as a result of agricultural processes. There are additional emissions from oceans though these are currently much more uncertain compared with those from agriculture. There are few measurements of ammonia in the boundary layer because it is difficult to measure reliably. The available studies point to ammonia being readily dry deposited and to react rapidly with acidic gases forming aerosol species such ammonium sulphate, nitrate and chloride. Ammonium aerosols are efficiently scavenged into precipitation as is gaseous ammonia itself. The later process exerts a significant influence on the acidity of cloud droplets and hence on the rate of sulphur dioxide oxidation by hydrogen peroxide and ozone.

Much of the detailed understanding of the fate and behaviour of ammonia is incorporated into STOCHEM and the resulting global deposition fields for ammonia and its ammonium compounds are shown in Figure 9. Global NH_x deposition is dominated by the contribution from wet deposition which accounts for 62% of the total. The largest single terms are the wet deposition and dry deposition of gaseous ammonia which are closely similar in magnitude and

between them account for 71% of total deposition.

The spatial patterns of the NH_x deposition fields, both dry and wet, are dominated by the influence of continental land areas. Only the wet deposition field of ammonium sulphate aerosol shows appreciable deposition over the remote oceans. Peak wet NH_x deposition levels over continental areas approach 200 mg N m^{-2} yr^{-1}. In contrast wet deposition levels over the remote oceans are 10-30 mg N m^{-2} yr^{-1} or lower. Total deposition levels appear to be higher over continental Europe and Asia compared with north America, south America and Africa. Observed wet ammonium deposition over the continents ranges from 210-500 mg N m^{-2} yr^{-1} and 5-40 mg N m^{-2} yr^{-1} over the remote oceans (Whelpdale and Kaiser, 1996), providing excellent confirmation of the model results.

4. European Acid Deposition in the STOCHEM Model

Dry sulphur deposition

There are two processes which, in principle, contribute to dry sulphur deposition and they are the dry deposition of gaseous sulphur dioxide (SO_2) and of particulate sulphate aerosol, including both sulphuric acid droplets and ammonium sulphate particles. Of these, however, only the dry deposition of sulphur dioxide makes a major contribution and this is the only process considered in detail in this section. The observed dry sulphur deposition field across Europe from 25°W to 45°E and from 35°N to 70°N for 1994 is plotted out in Figure 10a. This observed field was obtained by combining the annual mean SO_2 concentrations from the EMEP monitoring network (Hjellbrekke et al. 1996) for 1994 in μg S m^{-3} with a dry deposition velocity for SO_2 of 5 mm s^{-1}. Dry sulphur deposition appears to increase steadily eastwards from about 250 mg S m^{-2} yr^{-1} over Ireland to a maximum of 640 mg S m^{-2} yr^{-1} in central Europe.

The STOCHEM model calculated dry sulphur deposition field over Europe shows the same general features as the observations with low values on the Atlantic Ocean fringes and high values in central Europe, see Figure 10b. The model values are between double and three times the observations so that the maximum value is over 1600 mg S m^{-2} yr^{-1}. The European area-weighted mean dry sulphur deposition is 538 mg S m^{-2} yr^{-1} in the model compared with 246 mg S m^{-2} yr^{-1} in the observations (Hjellbrekke et al. 1996). For the central England grid square, the model gives a dry sulphur deposition load of 800 mg S m^{-2} yr^{-1}. The STOCHEM model dry sulphur budget for the UK amounts to about 240 thousand tonnes S yr^{-1} and is well within the range of the estimated budgets of 154 and 265 thousand tonnes yr^{-1} based on the UK precipitation network (RGAR 1997) and the EMEP model (Barrett and Berge 1996), respectively.

On the basis of the site-by-site and budget comparisons for dry sulphur

deposition, it would appear that the STOCHEM model estimates are within about a factor of two of the available estimates from observations and from other models. The STOCHEM model is therefore representing some of the salient features that control the dry deposition budgets for the UK and Europe.

Wet sulphur deposition

There are, in principle, two main processes which contribute to wet sulphur deposition and these are the in-cloud scavenging of sulphate aerosol particles, including both sulphuric acid droplets and ammonium sulphate particles, and the below-cloud scavenging of sulphur dioxide. The observed wet sulphur deposition field from the EMEP precipitation network (Hjellbrekke et al. 1996) for 1994 is shown in Figure 11a using the observations in which sea-salt sulphate has been subtracted. The observed deposition field steadily increases from about 400 mg S m^{-2} yr^{-1} over northern Scotland to 1000 mg S m^{-2} yr^{-1} in central Europe.

The STOCHEM model calculated wet sulphur deposition field over Europe shows all of the main features of the observed field, with low values on the Atlantic Ocean fringes and higher values in central and Eastern Europe, see Figure 11b. The STOCHEM values are generally closely similar to the observations for much of the European area. Model maximum values are just over 1000 mg S m^{-2} yr^{-1} and minimum values about 300 mg S m^{-2} yr^{-1}. The mean wet sulphur deposition load over the area of Figure 11b is 440 mg S m^{-2} yr^{-1} compared with the mean observed wet sulphur deposition load of 574 mg S m^{-2} yr^{-1} . The model appears to be underestimating observation by about 23%. For the central England grid square, the STOCHEM model gives a mean wet deposition load of 500 mg S m^{-2} yr^{-1}. The model wet sulphur budget for the UK amounts to about 150 thousand tonnes S yr^{-1} compared with the estimated budgets of 226 and 185 thousand tonnes yr^{-1} from the UK precitation network (RGAR 1997) and from the EMEP model (Barrett and Berge 1996), respectively.

On the basis of the site-by-site and budget comparisons for wet sulphur deposition, it would appear that the STOCHEM model estimates are within ± 25% of the observations. The model is therefore representing most of the salient features that control the wet sulphur deposition budgets for the UK and Europe.

Total sulphur deposition

By adding together the dry sulphur and wet sulphur deposition fields, it is possible to generate a total sulphur deposition field which gives a representation of the total acid deposition load received by the earth's surface and brought by the deposition of acidic sulphur species. The observed EMEP total sulphur deposition field is shown in Figure 12a and the corresponding field from STOCHEM in Figure 12b. The mean total sulphur deposition load over the entire map area is 821 mg S m^{-2} yr^{-1} in the EMEP observations and 980 mg S m^{-2} yr^{-1} in STOCHEM. This level of agreement, to within ± 30%, is

considered highly acceptable for a global chemistry-transport model.

Wet oxidised nitrogen deposition

In comparison with sulphur deposition, much less is known about the mechanisms underpinning the estimates of the wet deposition of nitrogen compounds. Reliable observations are available for the nitrate concentrations in precipitation and these can be compiled quite accurately into wet deposition fields for oxidised nitrogen (NO_y) compounds, see Figure 13a. The observed EMEP wet NO_y deposition field (Hjellbrekke et al. 1996) shows a minimum in the European arctic of about 76 mg N m^{-2} yr^{-1} and a maximum in central and southern Europe of about 700 mg N m^{-2} yr^{-1}.

The STOCHEM model includes the scavenging of gaseous NO_y compounds, nitric acid and N_2O_5 by background aerosol particles to form nitrate aerosol which is then removed into rain by in-cloud scavenging. The resulting wet NO_y deposition field is shown in Figure 13b. Again, it shows many of the features found in the observations, with minimum values in the arctic and maximum values in central Europe. However, calculated values underestimate the observations by about a factor of two. The area-weighted mean wet NO_y deposition in the observations is about 325 mg N m^{-2} yr^{-1}, with the model calculated value of 210 mg N m^{-2} yr^{-1}, about 35 % lower.

For the central England grid square, the model gives a wet deposition load of 220 mg N m^{-2} yr^{-1}. The model wet NO_y budget for the UK amounts to about 66 thousand tonnes N yr^{-1} , which is nearly within the range set by the estimated budgets of 110 and 74 thousand tonnes yr^{-1} from the precipitation network (RGAR 1997) and from the EMEP model (Barrett and Berge 1996), respectively.

On the basis of the site-by-site and budget comparisons for wet oxidised nitrogen deposition, it would appear that the STOCHEM model estimates are about 30 % too low but with the correct spatial pattern over Europe. The model is therefore catching some but not all of the important features that control the wet oxidised nitrogen deposition budgets for the UK and Europe. Clearly, further work is required in STOCHEM to improve the treatment of the wet scavenging of nitric acid and N_2O_5.

Wet reduced nitrogen deposition

As with the deposition of oxidised nitrogen compounds, little is known about the mechanisms underpinning the estimates of the wet deposition of reduced nitrogen compounds. Reliable observations are available for the ammonium concentrations in precipitation and these can be compiled quite accurately into wet deposition fields for reduced nitrogen (NH_x) compounds, see Figure 14a. The observed EMEP wet NH_x deposition field (Hjellbrekke et al. 1996) shows a minimum in the European arctic of about 70 mg N m^{-2} yr^{-1} and a maximum in central and southern Europe of about 980 mg N m^{-2} yr^{-1}.

The STOCHEM model includes the scavenging of gaseous ammonia into cloud droplets and its reaction in cloud droplets to form ammonium sulphate which is then removed into rain by in-cloud scavenging. The resulting wet NH_x deposition field is shown in Figure 14b. Again, it shows many of the features found in the observations, with minimum values in the arctic and maximum values in central Europe. However, calculated values grossly underestimate the observations. The area-weighted mean wet NH_x deposition in the observations is about 440 mg N m^{-2} yr^{-1} with the model value of 150 mg N m^{-2} yr^{-1} about a factor of three below this value. For the central England grid square, the STOCHEM model gives a wet deposition load of 170 mg N m^{-2} yr^{-1}. The model wet NH_x budget for the UK amounts to about 51 thousand tonnes N yr^{-1} compared with the estimated budgets of 138 and 94 thousand tonnes yr^{-1} from the precipitation network (RGAR 1997) and from the EMEP model (Barrett and Berge 1996), respectively.

On the basis of the site-by-site and budget comparisons for wet reduced nitrogen deposition, it would appear that the STOCHEM model estimates are about a factor of two to three, too low. The model is therefore catching some but not all of the important features that control the wet reduced nitrogen deposition budgets for the UK and Europe. Clearly, further work is required on the ammonia emissions in the model, its dry deposition and the formation of ammonium sulphate aerosol and its wet scavenging.

Future Acid Deposition in the 2015 Scenario Cases

Figures 15a-d present the total sulphur deposition maps for the 1992 and three 2015 scenario cases. In the IS92a scenario case, European SO_2 emissions are anticipated to rise by 35% with an attendant 32% increase in model area-weighted mean total sulphur deposition, see Figures 15a and b. This scenario does not take into account the measures already agreed by UN ECE member states to control SO_2 emissions over the time frame of the year 2015. The 2015-CRP scenario takes these measures into account both in north American and European SO_2 emissions. The latter emissions are assumed to be 60% of their 1990 levels, (that is, 40% lower). Figures 15a and c show that a substantial reduction in sulphur deposition is anticipated by the year 2015 with current reduction plans compared with the present day situation.The model area-weighted mean total sulphur deposition for 1992 emissions was about 980 mg S m^{-2} yr^{-1} , Figure 15a, and is estimated to fall to about 656 mg S m^{-2} yr^{-1} by 2015, Figure 15c. This decrease in total sulphur deposition amounts to about 33%, compared with the 40% reduction in emissions, both expressed relative to their respective 1992 levels. In the 2015-MFR scenario case, European SO_2 emissions fall to 2.2% of their 1992 levels assuming the strictest emission reductions. The area-weighted mean total sulphur deposition merely falls to 120 mg S m^{-2} yr^{-1}, that is to 12% of its 1992 level, see Figure 15d.

In the 1992 scenario case, the integrated sulphur deposition over the European study region in Figure 7, amounted to about 17.3 million tonnes S yr^{-1}, for an area of 17.6 million km^2. This integrated deposition corresponds approximately

to about three-quarters of the total European SO_2 emissions. The remaining quarter of the European emissions is available for long range transport and is ultimately deposited in the Arctic and Atlantic Oceans and across the continents of Asia and Africa. The corresponding EMEP model estimate (Barrett and Birge 1996) of the total sulphur deposition in 1990 is 15.1 million tonnes S yr^{-1} , in excellent agreement with the value from STOCHEM.

In the 2015 scenario cases, integrated sulphur deposition increases to about 22.8 million tonnes S yr^{-1}, in the IS92a case but decreases to about 11.6 million tonnes S yr-1 in the 2015-CRP case. In the 2015-MFR case, integrated sulphur depsotion falls even further to 2.1 million tonnes S yr-1, despite European SO2 emissions only of 0.4 million tonnes S yr-1. European sulphur deposition is anticipated to be greater than the European sulphur emissions. Under these conditions, almost all of the SO_2 emitted over Europe is deposited there with no remainder exported out of Europe. Furthermore, a small but significant net import of sulphur from North America and Asia is now apparent by long range transport in Figure 15d. This net import explains the apparent excess of sulphur deposition over emission.

Clearly, as the global tropospheric oxidant concentrations rise over the period from 1992 to 2015, total sulphur deposition loads over central Europe are expected to fall slower than SO_2 emissions. This is because, all things being equal, more oxidation can occur and less so less European sulphur is available for long range transport. However, as European sulphur deposition loads fall, contributions from north America and Asia will become more noticeable. Reductions in sulphur deposition loads to sensitive ecosystems may not necessarily fall directly in line with the fall in European SO_2 emissions.

For the consideration of the environmental problems associated with soil and freshwater acidification and with the eutrophication of sensitive ecosystems, it makes no significant difference if the nitrogen inputs arise by either the wet or dry routes or as oxidised NO_y or reduced nitrogen NH_x. Accordingly, concern is given to total nitrogen deposition from all nitrogen-containing trace substances and by all deposition routes. Figures 16a-d present maps of European total nitrogen deposition for 1992 and for the three 2015 scenario cases. The area-weighted mean nitrogen deposition amounts to 651 mg N m^{-2} yr^{-1} in the base case and rises to 853 mg N m^{-2} yr^{-1} in the 2015 IS92a case, Figures 16a and b. The increase in nitrogen deposition is about 30%, which closely parallels that in the emissions, 45% in NO_x and 20% in ammonia. In the 2015-CRP scenario case, current reductions plans for NO_x emissions bring total nitrogen deposition back down almost to its 1992 levels, see Figure 16c. The stringent NOx emission reductions in the 2015-MFR scenario, reduce the mean total nitrogen deposition down to 563 mg N m^{-2} yr^{-1}, corresponding to a level 13% lower than in the 1992 base case. This reduction in total nitrogen deposition reflects the outcome of a reduction in NO_x emissions of 60% and an increase of 20% in NH_3 emissions.It appears that total nitrogen deposition loads fall significantly slower than NO_x emissions as the concentrations of tropospheric oxidants rise in the future and ammonia emissions remain unchecked.

The integrated total nitrogen deposition in Figure 16 for the 1992 model calculations amounted to about 11.5 million tonnes N yr^{-1}, or about 80% of the total European NO_x+NH_3 emissions summed. The total integrated nitrogen deposition in the EMEP model for 1990 (Barrett and Birge 1996) is 10.92 million tonnes N yr^{-1} , in close agreement with the present study.

5. Photochemical Oxidant Formation in North-west Europe in the STOCHEM Model

Present Day Observed and Calculated Ozone Distributions Across Europe

Ozone concentrations at rural monitoring sites in north-west Europe tend to show higher values in the spring and summer months compared with autumn and winter months. Peak ozone concentrations also tend to be higher in central Europe compared with those reported in the northern or western fringes. The World Health Organisation have recommended an air quality critieria value for ozone of 60 ppb, maximum 8-hour mean concentration, not to be exceeded more than once per year (WHO 1996). It is likely that during 1995, this level was exceeded at almost all of the rural European ozone monitoring sites, except those in the arctic fringes of northern Europe. Some of these facets can be seen in Figure 17a which plots a contour map through the 95-percentile hourly mean ozone concentrations reported during April to September 1995 for the 96 EMEP ozone monitoring stations (Hjellbrekke 1997). The 95-percentile hourly value is the 219th highest ranked hourly ozone value reported during the six month period. It represents a level which is indicative of the general frequency and intensity of photochemical ozone episodes observed in that year.

The 95-percentile hourly ozone levels reach a maximum of just over 70 ppb in Italy. Levels are above 65 ppb across a wide area of central Europe covering the Alps, much of Germany and Italy and extending eastwards into the Former Republic of Yugoslavia and the Czech and Slovak Republics. The 60 ppb contour divides the United Kingdom through Midlands and separates central Europe from Scandinavia and from the Russian Federation. The 50 ppb contour includes much of the European arctic.

The monthly mean ozone concentrations for Europe from STOCHEM generally peak during July and so July concentrations are a reasonable guide to the maximum ozone concentrations found over Europe, see Figure 17b. Since STOCHEM cannot resolve the shallow nocturnal boundary layers which are often seen at night over rural areas during summertime, it is unable to reproduce the marked diurnal variations observed in rural ozone monitoring records. However, STOCHEM should be able to reproduce the mid-afternoon ozone concentrations when convection is at its most efficient and surface ozone concentrations are representative of those found in a considerable depth of the lower atmosphere. Mean ozone concentrations for the lowest layer of STOCHEM at 550 metres should therefore be directly comparable with the

mid-afternoon maximum surface ozone concentrations and should be considerably higher than the observed mean surface ozone concentrations which are strongly influenced by nighttime values, depleted by dry deposition under shallow nocturnal inversion layers.

The monthly mean surface layer ozone distribution for July from STOCHEM in Figure 17b shows many features in common with the 95-percentile hourly mean ozone observations from the EMEP network in Figure 17a. The low arctic values are reproduced by STOCHEM, together with the dividing lines across the United Kingdom and through Scandinavia. The maximum over Italy is also reproduced in STOCHEM but on an altogether larger scale which includes much of the Balkans and southern Europe. There are too few ozone monitoring sites in southern Europe and the Balkans to attribute any particular significance to the apparent overestimation of the observed ozone concentrations in south east Europe. The European area-weighted mean July ozone concentration in the model was 55 ppb, compared with the observed mean 95-percentile hourly mean ozone concentration of 58.4 ppb in the EMEP network.

Whilst peak hourly ozone concentrations or some suitable percentile, have a certain simplicity, this simplicity is not always an advantage in choosing ozone indicators for use in developing air quality policies. The World Health Organisation, for example, have preferred to develop air quality guidelines for ozone based on 8-hourly mean ozone concentrations. However, 8-hourly mean concentrations cannot easily be incorporated into integrated assessment models. It has therefore been proposed that, for the purposes of integrated assessment modelling, the AOT_{60} concept is employed as a surrogate for the 8-hourly mean exposure measure (Bull and Krzyzanowski 1997). AOT_{60} values in ppb hours are calculated from hourly ozone records by summing all the concentration exceedances above a 60 ppb threshold, throughout a six-month period. Figure 18a presents a scatter plot of AOT_{60} values in ppb hours for each of the 96 EMEP ozone monitoring sites against their respective 95-percentile hourly mean ozone concentrations. This scatter plot was then used to convert the ozone concentrations from STOCHEM into AOT_{60} values, directly.

The observed and model calculated European distributions of AOT_{60} are plotted out in Figures 19a and b, repectively. These maps show many features in common, including the maximum values in central Europe and the steep gradients towards the arctic. However, because of the steepening relationship between AOT_{60} and 95-percentile with increasing ozone levels, there is a tendency for the model to overestimate AOT_{60} levels. The observed European area-weighted mean AOT_{60} exposure in the EMEP network was 2700 ppb hours compared with 3800 ppb hours in the model.

Whilst the high percentiles of the hourly mean ozone concentrations are a useful indicator of the frequency and intensity of photochemical episodes and hence of the importance of the ozone exposures to human health, there are other important environmental impacts of ozone (WHO 1987). To gauge the

significance of ozone and its impacts on crops and vegetation, critical levels have been defined for ozone in terms of the accumulated time that ozone concentrations are above a particular threshold concentration (Karenlampi and Skarby 1996). Considering commercial crops such as wheat, then a critical level for ozone can be defined in terms of a threshold concentration of 40 ppb and the accumulated exposure, AOT_{40}, above this level of 3000 ppb hours during daylight and the growing season, May to July inclusive. For forests, the critical level is defined with the same 40 ppb threshold but with an accumulated exposure, AOT_{40}, of 10 000 ppb hours during all hours and the whole summertime period.

Ozone critical levels for crops are exceeded throughout Europe in all but the arctic regions. The critical levels for forests are only exceeded in central and southern Europe, with a dividing line skirting southern England, including Denmark and southern Sweden and then dividing the Russian Federation. Because of the strong overlap between the two exceeded regions, further consideration need only be given to the AOT_{40} for crops.

By plotting out the AOT_{40} crops levels against the 95-percentile hourly mean ozone concentrations for the 96 EMEP ozone monitoring sites, see Figure 18b, it is possible to construct a relationship between the quantities that can be used to convert the model ozone concentrations into AOT_{40} values. The observed AOT_{40} distribution obtained from the EMEP network is shown in Figure 20a and can be compared directly with the model results in Figure 20b. Again, there are many striking similarities between the observed and model calculated maps. The 3000 ppb hours contour in the observations is found in the Arctic regions of Norway, Finland and Russia and this is also the case in the model. Peak AOT_{40} exposures reach and exceed 12000 ppb hours in the Alps and Italy. A maximum with a similar magnitude is found in the model but it is somewhat greater in magnitude and is located more towards central and eastern Europe.

The observed European area-weighted mean AOT_{40} exposure over the EMEP network is 6500 ppb hours, more than twice the ozone critical level, compared with 7100 ppb hours in the model calculations.

Ozone Distributions in the Year 2015

Figures 21a-d map the changes in the July ozone distribution across Europe for 1992 and the three 2015 scenario cases. In the base case, maximum ozone concentrations were just under 76 ppb with the 50 ppb contour passing through the arctic regions and up the Atlantic coast fringes of Europe. Most of Great Britain lies between the 50 and 60 ppb contours. In the 2015-IS92a business-as-usual case, the maximum concentrations increase to 86 ppb and most of Great Britain moves up to between the 60 and 70 ppb contours. This increase is almost, but not quite, removed in the 2015-CRP scenario case, where the maximum value calculated is 73 ppb. In the 2015-MFR scenario case, the 60 ppb contour moves off Great Britain and the maximum concentrations in Europe fall to just under 70 ppb. The WHO air quality standard of 60 ppb

maximum 8-hour mean concentration (WHO 1996) is likely to be exceeded throughout much of continental Europe, although it is unlikely to be exceeded in the United Kingdom and Scandinavia.

The maps of AOT_{60} in 1992 and 2015 in Figures 22a-d show similar behaviour to that of the peak ozone concentrations. There is a substantial increase in AOT_{60} exposures anticipated between the 1992 and the year 2015, which is close to a doubling. This increase relative to 1992 is reduced significantly in the 2015-CRP scenario case. The additional NO_x emission reductions implied in the 2015-MFR scenario case, reduce AOT60 exposures but does not remove them entirely. The WHO air quality standard is not met across Europe in the 2015-MFR scenario case.

The target of reducing AOT_{40} exposures to reach the ozone critical level of 3000 ppb hours appears infeasible in Figures 23a-d. As shown in Figure 23d, with maximum feasible reductions in SO_2 and NO_x, AOT_{40} exposures still exceed 3000 ppb hours over the entire area of north-west and central Europe. Only the Arctic areas of Norway, Finland and Russia have substantial areas where the ozone critical level is not exceeded. The European area-weighted mean AOT40 exposure remains at about double the ozone critical level in the 2015-MFR scenario case.

This situation in 2015 is caused by the global growth in man-made methane, hydrocarbons, NO_x and carbon monoxide emissions leading to increased baseline tropospheric ozone concentrations. These increased baseline concentrations approach so closely to the AOT_{40} threshold concentration, that regional photochemical ozone production can still lead to exceedance of ozone critical levels despite large reductions in European NO_x emissions. Action on the global scale to control ozone precursor emissions other than NO_x will be required if ozone critical levels are to be reached in the year 2015 across Europe.

6. DISCUSSIONS AND CONCLUSIONS

In this study, a global 3-D Lagrangian chemistry model (STOCHEM) is applied to the formation of tropospheric oxidants and their influence on the regional scale formation and transport of photochemical ozone and on the deposition of acidic species. We show here how, without simultaneous action on the global scale to control methane and other tropospheric ozone precursors, concentrations of tropospheric oxidants will increase in future years.

Tropospheric hydroxyl radical concentrations increase globally only slightly by about 1% between 1992 and 2015 in the IS92a 'business-as-usual' scenario of the IPCC. This concentration increase appears to be driven by a complex interaction between the separate trends in methane and carbon monoxide which act to decrease OH concentrations and the trends in NO_x and ozone

which act to increase OH concentrations.

Globally, the ozone burden increases by about 8% between 1992 and 2015 and the mean surface concentration increases by about 3 ppb, taking the mean concentration up to just under 36 ppb. Surface ozone concentrations may be up to 10 ppb higher during summertime over the polluted northern hemisphere continental regions.

The global sulphur cycle has already been heavily influenced by human activities with man-made SO_2 sources now dominating over the oxidation of dimethyl sulphide by a factor of about 6. The lifetime of sulphur dioxide is just under 2 days with dry and wet deposition roughly comparable removal processes. The global burdens of sulphur dioxide and sulphate aerosols are closely similar although the sulphate aerosol lifetime is just under 4 days. Wet deposition is by far the dominant removal process for sulphate aerosol.

On the European scale, STOCHEM gives an excellent account of the major features of spatial pattern of sulphur deposition in comparison with the observations from the EMEP network. Dry deposition is overestimated by about a factor of two and wet deposition underestimated by about 25%, leaving total deposition within ± 30% of the observations. Wet deposition of oxidised and reduced nitrogen compounds are underestimated and further work is required to improve the treatment of the wet scavenging of nitrogen compounds.

As the global tropospheric oxidant concentrations rise over the period from 1992 through to 2015, sulphur deposition loads are anticipated to fall slower than SO_2 emissions. This is because, all things being equal, more oxidation of the sulphur can occur increasing local deposition and decreasing long range transport out of Europe. Furthermore, as European SO_2 emissions fall, the long range transport contributions from other continents and from natural sources become more noticeable. Reductions in sulphur deposition to remote and sensitive ecosystems may not fall directly in line with the fall in European SO_2 emissions.

STOCHEM generates a particularly realistic picture of the distribution of ozone concentrations across Europe compared with the observations from the EMEP monitoring network. By the year 2015, peak ozone concentrations are anticipated to increase throughout Europe by about 10 ppb, during summertime and in the IS92a 'business-as-usual' scenario. The increase in ozone concentrations is diminished dramatically by the current reductions plans for NO_x and SO_2 emissions in both Europe and north America. However, maximum feasible reductions for NO_x and SO_2 in Europe are not enough to keep future peak ozone levels below internationally-accepted environmental criteria. Only with additional stringent reductions in European VOC and CO emissions, can health-based air quality guidelines for ozone be met satisfactorily throughout Europe. However, action will be required on the global scale to control ozone precursor emissions if ozone critical levels set to protect crops, are to be reached in the year 2015 within Europe.

7. ACKNOWLEDGEMENTS

This work was supported through the Public Meteorological Service research and development programme of the Meteorological Office, as part of the research programme of the Air and Environment Quality Division of the Department of the Environment, Transport and Regions through contract number EPG 1/3/93 and as part of the Climate Prediction programme of the Global Atmosphere Division of the Department of the Environment, Transport and Regions through contract number PECD 7/12/37. The assistance of Ms Anne-Gunn Hjellbrekke in providing the EMEP AOT_{60} data is gratefully appreciated. Dr Michael Jenkin and Dr Gary Hayman are acknowledged for their help in reviewing the chemical kinetic data used in the chemical mechanism.

8. REFERENCES

Amann, M., Bertok, I., Cofala, J., Gyarfas, F., Heyes, C., Klimont, Z., Makowski, M., Shibayev, S. and Schopp, W., (1997). Cost-effective control of acidification and ground-level ozone. Third Interim Report. International Institute for Applied Systems Analysis, Laxenburg, Austria.

Atkinson, R., (1994). Gas-phase tropospheric chemistry of organic compounds. J. Phys. Chem. Ref. Data, Monograph Number 2, 1-216.

Atkinson, R., Baulch, D.L., Cox, R.A., Hampson, R.F., Kerr, J.A. and Troe, J., (1992). Evaluated kinetic and photochemical data for atmospheric chemistry. Supplement IV. IUPAC subcommittee on gas kinetic data evaluation for atmospheric chemistry. J. Phys. Chem. Ref. Data, 21, 1125-1568.

Atkinson, R., Baulch, D.L., Cox, R.A., Hampson, R.F., Kerr, J.A., Rossi, M.J. and Troe, J., (1996). Evaluated kinetic and photochemical data for atmospheric chemistry. Supplement V. IUPAC subcommittee on gas kinetic data evaluation for atmospheric chemistry. Atmospheric Environment, 30, 3903-3904.

Barrett, K. and Berge, E., (1996). Transboundary air pollution in Europe. Part 1: Estimated dispersion of acidifying agents and of near surface ozone. EMEP/MSC-W Report 1/96. The Norwegian Meteorological Institute, Oslo, Norway.

Benkovitz, C.M., Dignon, J., Pacyna, J., Scholtz, T., Tarrason, L., Volder, E. and Graedel, T.E., (1995). Global inventories of anthropogenic emissions of SO_2 and NO_x. in preparation.

Bull, K.R. and Krzyzanowski, M., (1997). Health efffects of ozone and nitrogen

oxides in an integrated assessment of air pollution. Institute for Environment and Health. University of Leicester, UK.

Chatfield, R.B. and Delany, A.C., (1990). Convection links biomass burning to increased tropical ozone: However, models will tend to overpredict O_3. J. Geophys. Res. 95, 18473-18488.

Chin, M., Jacob, D.J., Gardner, G.M., Foreman-Fowler, M.S., and Spiro, P.A., (1996). A global three-dimensional model of tropospheric sulphate. J. Geophys. Res., 101, 18667-18690.

Chock, D.P. and Winkler, S.L., (1994). A Comparison of advection algorithms coupled with chemistry. Atmospheric Environment 28, 2659-2675.

Collins, W.J., Stevenson, D.S., Johnson, C.E. and Derwent, R.G. (1997). Tropospheric ozone in a global-scale three-dimensional Lagrangian model and its response to NOx emissions controls. J. Atmos. Chem. 26, 223-274.

Crutzen, P.J., (1974). Photochemical reactions initiated by and influencing ozone in the unpolluted troposphere. Tellus 26, 47-57.

Cullen, M.J.P., (1993). The unified forecast/climate model. Meteorological Magazine, 122, 81-94, London, UK.

Dabdub, D. and Seinfeld, J.H., (1994). Numerical advective schemes used in air quality models - sequential and parallel implementation. Atmospheric Environment 28, 3369-3385.

DeMore W.B., Sander S.P., Golden D.M., Hampson R.F., Kurylo M.J., Howard C.J., Ravishankara A.R., Kolb C.E. and Molina M.J. (1994) Chemical kinetics and photochemical data for use in stratospheric modeling. NASA Panel for Data Evaluation No. 10. Jet Propulsion Laboratory 94-26, JPL, Pasadena, California, USA.

DeMore W.B., Sander S.P., Golden D.M., Hampson R.F., Kurylo M.J., Howard C.J., Ravishankara A.R., Kolb C.E. and Molina M.J. (1994) Chemical kinetics and photochemical data for use in stratospheric modeling. Evaluation Number 12. Jet Propulsion Laboratory 97-4, JPL, Pasadena, California, USA.

Derwent, R.G., Simmonds, P.G. and Collins, W.J., (1994). Ozone and carbon monoxide measurements at a remote maritime location, Mace Head, Ireland, from 1990 to 1992. Atmospheric Environmnet 28, 2623-2637.

Dignon, J. and Hameed, S., (1989). Global emissions of nitrogen and sulfur oxides from 1860 to 1980. J. Air Pollut. Control Ass. 39, 180-186.

Dlugokencky, E.J., Lang, P.M., Masarie, K.A., and Steele, L.P. (1994). Atmospheric CH_4 records from sites in the NOAA/CMDL air sampling network.

Trends 93, pp 274-350. Carbon Dioxide Information Center, Oak Ridge National Laboratory, USA.

Ehhalt, D.H., Rohrer, F. and Wahner, A., (1992). Sources and distribution of NO_x in the upper troposphere at northern mid-latitudes. J. Geophys. Res. 97, 3725-3738.

Eliassen, A., Hov, O., Isaksen, I.S.A., Saltbones, J. and Stordal, F., (1982). A Lagrangian long range transport model with atmospheric boundary layer chemistry. J. Applied Met. 21, 1645-1661.

Feichter, J., Brost, R.A., and Heimann, M., (1991). Three-dimensional modelling of the concentrations and deposition of ^{210}Pb aerosols. J. Geophys.Res., 96, 22447-22460.

Franzblau, E. and Popp, C.J., (1989). Nitrogen oxides produced from lightning. J. Geophys. Res. 94, 11089-11104.

Grennfelt, P., Hov, O. and Derwent, R.G., 1994. Second generation abatement strategies for NO_x, NH_3, SO_2 and VOCs. Ambio 23, 425-433.

Guenther, A., Hewitt, C.N., Erickson, D., Fall, R., Geron, C., Graedel, T., Harley, P., Klinger, L., Lerdau, M., McKay, W.A., Pierce, T., Scholes, R., Steinbrecher, R., Tallamraju, R., Taylor, J. and Zimmerman, P., (1995). A global model of natural volatile organic compound emissions. J. Geophys. Res. 100, 8873-8892.

Hertel, O., Berkowicz, R., Christensen, J., and Hov. O. (1993). Tests of two numerical schemes for use in atmospheric transport chemistry models. Atmospheric Environment 27A, 2591-2611.

Hjellbrekke, A.-G., (1997). Ozone measurements 1995. EMEP/CCC Report 3/97, Norwegian Institute For Air Research, Kjeller, Norway.

Hjellbrekke, A.-G., Schaug, J. and Skjelmoen, J.E., (1996). EMEP Data Report 1994. Part 1: Annual summaries. EMEP/CCC Report 4/96, Norwegian Institute For Air Research, Kjeller, Norway.

Hough, A.M., (1988). The calculation of photolysis rates for use in global tropospheric modelling studies. AERE Report R-13259, HMSO, London.

Hough, A.M., (1991). Development of a two-dimensional global tropospheric model: Model chemistry. J. Geophys. Res. 96, 7325-7362.

Hough, A.M. and Derwent, R.G. (1990). Changes in the global concentration of tropospheric ozone due to human activities. Nature 344, 645-650.

IPCC (1992). Climate change 1992. Intergovernmental Panel on Climate

Change. Cambridge University Press, Cambridge, UK.

IPCC (1995). Climate change 1994. Intergovernmental Panel on Climate Change. Cambridge University Press, Cambridge, UK.

IPCC (1996). Climate Change 1995. Intergovernmental Panel on Climate Change. Cambridge University Press, Cambridge, UK.

Jacob, D.J. and Wofsy, S.C., (1988). Photochemistry of biogenic emissions over the Amazon forest. J. Geophys. Res. 93, 1477-1486.

Jenkin, M.E., Clement, C.F. and Ford, I.J., (1996). Gas-to-particle conversion pathways. AEA Technology Report, AEA/RAMP/20010010/001/Issue 1, Culham Laboratory, Oxfordshire, UK.

Jenkin M.E., Saunders S.M. and Pilling M.E., (1997). The tropospheric degradation of volatile organic compounds: A protocol for mechanism development. Atmospheric Environment 31, 81-104.

Karenlampi L. and Skarby L., (1996). Critical levels for ozone in Europe: Testing and finalizing the concepts. University of Kuopio, Finland.

Langner, J. and Rodhe, H., (1991). A global three-dimensional model of the tropospheric sulphur cycle. J. Atmos. Chem. 13, 225-263.

Levy, H., (1971). Normal atmosphere: large radical and formaldehyde concentrations predicted. Science, 173, 141-143.

Li, D. and Shine, K., (1995). A 4-dimensional ozone climatology for UGAMP models. UGAMP Internal Report, University of Reading, UK.

Lightfoot, P.D., Cox, R.A., Crowley, J.N., Destriau, M., Hayman, G.D., Jenkin, M.E., Moortgat, G.K. and Zabel, F., (1992). Organic peroxy radicals: Kinetics, spectroscopy and tropospheric chemistry. Atmospheric Environment 26A, 1805-1961.

Logan, J.A., (1983). Nitrogen oxides in the troposphere: Global and regional budgets. J. Geophys. Res. 88, 10785-10807.

Maryon, R.H. and Best, M.J., (1992). NAME, ATMES and the boundary layer problem. Met O (APR) Turbulence and Diffusion Note No. 204, Meteorological Office, Bracknell, UK.

Metcalfe, S.E., Whyatt, J.D. and Derwent, R.G., (1995). A comparison of model and observed network estimates of sulphur deposition across Great Britain for 1990 and its likely source attribution. Quart. J. Roy. Met. Soc. 121, 1387-1411.

Murphy, D.M. and Fahey, D.W., (1994). An estimate of the flux of stratospheric

reactive nitrogen and ozone into the troposphere. J. Geophys. Res. 99, 5325-5332.

Olson, J. and Watts, J., (1982). Map of major world ecosystem complexes, Environmental Sciences Division, Oak Ridge National Laboratory, USA.

Parrish D.D., Holloway J.S., Trainer M., Murphy P.C., Forbes G.L., and Fehsenfeld F.C. (1993). Export of North American ozone pollution to the North Atlantic Ocean. Science 259, 1436-1439.

Penner, J.E., Atherton, C.S., Dignon, J., Ghan, S.J., Walton, J.J. and Hameed, S., (1991). Tropospheric nitrogen: A three-dimensional study of sources, distributions and deposition. J. Geophys. Res. 96, 959-990.

Pham M., Muller, J.-F., Brasseur G., Granier C. and Megie G., (1996). A three-dimensional model study of the tropospheric sulfur cycle. J. Geophys. Res., 100, 26061-26092.

Price, C. and Rind, D., (1992). A simple lighting parameterization for calculating global lightning distributions. J. Geophys. Res. 97, 9919-9933.

RGAR, (1997). Acid deposition in the United Kingdom 1992-1994. Review Group on Acid Rain. AEA Technology plc, Culham Laboratory, Oxfordshire, UK.

Simpson, D., (1991). Long period modelling of photochemical oxidants in Europe. EMEP MSC-W Note 1/91}, Norwegian Meteorological Institute, Oslo, Norway.

Spiro, P.A., Jacob, D.J. and Logan, J.A., (1992). Global inventory of sulfur emissions with 1°x1° resolution. J. Geophys. Res. 97, 6023-6036.

Stevenson, D.S., Collins, W.J., Johnson, C.E. and Derwent, R.G., (1997). The impact of aircraft nitrogen oxide emissions on tropospheric ozone studied with a 3D Lagrangian model including fully diurnal chemistry. Atmospheric Environment 31, 1837-1850.

Strand, A. and Hov, O, (1994). A two-dimensional global study of tropospheric ozone production. J. Geophys. Res. 99, 22877-22895.

Turman, B.N. and Edgar, B.C., (1982). Global lightning distributions at dawn and dusk. J. Geophys. Res. 87, 1191-1206.

United Nations, (1996). Report of the Twentieth Session. EB.AIR/GE.1/28, Geneva, Switzerland.

Volz, A. and Kley, D., (1988). Evaluation of the Montsouris series of ozone measurements made in the nineteenth century. Nature 332, 240-242.

Walton, J., MacCracken, M., Ghan, S., (1988). A global-scale Lagrangian trace species model of transport, transformation, and removal processes. J. Geophys. Res. 93, 8339-8354.

Warneck, P., (1988). Chemistry of the natural atmosphere, pp. 158-170, Academic Press, San Diego, California.

Whelpdale D.M. and Kaiser M.S. (1996) Global acid deposition assessment. World Meteorological Office Global Atmosphere Watch Report No. 106, WMO, Geneva, Switzerland.

WHO, (1987). Air quality guidelines for Europe. World Health Organisation Regional Publications, European Series No. 23, Copenhagen.

WHO, (1996). Update and revision of the WHO air quality guidelines for Europe. European Centre for Environment and Health, Bilthoven, Netherlands.

Wirtz, K., Roehl, C., Hayman, G.D. and Jenkin, M.E., (1994). LACTOZ re-evaluation of the EMEP MSC-W photo-oxidant model. EUROTRAC, Garmisch-Partenkirchen, Germany.

Yienger, J.J. and Levy, H. III, (1995). An empirical model of global soil-biogenic NO_x emission. J. Geophys. Res. 100, 11447-11464.

TABLE 1. List of species in the STOCHEM model.

Simple reactive atoms and free radicals

O^1D
O^3P
OH
NO_3
HO_2

Tropospheric source gases

NO
NO_2
CO
CH_4
H_2
SO_2
$(CH_3)_2S$
NH_3

Secondary pollutants

N_2O_5
HCHO
O_3
HNO_3
H_2O_2
peroxy nitric acid
sulphate aerosol
ammonium sulphate aerosol
nitrate aerosol
organic nitrogen-containing aerosol
dimethyl sulphoxide
methane sulphonic acid
dimethyl sulphone

Organic Compounds

CH_3OH
C_2H_4
C_2H_6
C_3H_6
C_3H_8
CH_3COCH_3
C_4H_{10}
C_5H_8
toluene

o-xylene

Secondary Organic Pollutants

CH_3CHO
PAN
CH_3OOH
C_2H_5OOH
C_3H_7OOH
C_4H_9OOH
isoprene hydroperoxide
methyl vinyl ketone hydroperoxide
$CH_3COC_2H_5$
CH3COCHO
CHOCHO
CHOC(CH3)=CHCHO
CH2=CHCOCH3

Reactive organic intermediates and free radicals

CH_3O_2
$C_2H_5O_2$
CH_3COO_2
$C_3H_7O_2$
$CH_3COCH_2O_2$
$C_4H_9O_2$
$CH_3COCH(O_2)CH_3$
$CH_2O_2CH_2OH$
$CH_3CHO_2CH_2OH$
toluene peroxy
o-xylene peroxy
methylmaleic dialdehyde peroxy
isoprene peroxy
methyl vinyl ketone peroxy
nitrato acetaldehyde
nitrato proprionaldehyde
nitrato isoprene aldehyde
CH_2OO
methyl sulphoxide radical
methyl sulphonate radical
dimethyl sulphone peroxy

TABLE 2. The rate coefficient and chemical kinetic data employed in the STOCHEM model.

Chemical or Photochemical Reaction Process	Rate coefficient
Simple atom and free radical reactions in fast photochemical balance	
1 $O+O_2+M=O_3+M$	(1,2,3) 6.0×10^{-34} [M] $(T/300)^{-2.3}$
2 $O+NO+M=NO_2+M$	(1,4) 9.0×10^{-32} $(T/300)^{-1.5}$
3	(1,5) 3.0×10^{-11}
4 $O(^1D)+O_2=O(^3P)+O_2$	(1,6) 3.2×10^{-11} exp(70/T)
5 $O(^1D)+N_2=O(^3P)+N_2$	(1,6) 1.8×10^{-11} exp(110/T)
6 $O(^1D)+H_2O=OH+OH$	(1,6) 2.2×10^{-10}
7 $NO+O_3=NO_2+O_2$	(1,6) 2.0×10^{-12} exp(-1400/T)
8 $NO_2+O_3=NO_3+O_2$	(1,6) 1.2×10^{-13} exp(-2450/T)
9 $OH+O_3=HO_2+O_2$	(1,6) 1.6×10^{-12} exp(-940/T)
10 $HO_2+O_3=OH+O_2+O_2$	(1,6) 1.1×10^{-14} exp(-500/T)
11 $O+NO_2=NO+O_2$	(1,6) 6.5×10^{-12} exp(120/T)
12 $NO+HO_2=OH+NO_2$	(1,6) 3.7×10^{-12} exp(250/T)
13 $OH+NO_2+M=HNO_3+M$	(1,4) 2.6×10^{-30} $(T/300)^{-3.2}$
14	(1,5) 2.4×10^{-11} $(T/300)^{-1.3}$
15 $HO_2+NO_2+M=HO_2NO_2+M$	(1,4) 1.8×10^{-31} $(T/300)^{-3.2}$

16	(1,5)	4.7×10^{-12} (T/300)$^{-1.4}$
17 $HO_2NO_2+M=HO_2+NO_2+M$	(1,7)	$k_{HO2+NO2+M} / 2.1 \times 10^{-27}$ exp(10900/T)
18 $OH+HO_2NO_2=H_2O+NO_2+O_2$	(1,6)	1.3×10^{-12} exp(380/T)
19 $OH+HO_2=H_2O+O_2$	(1,6)	4.8×10^{-11} exp(250/T)
20 $OH+H_2O_2=H_2O+HO_2$	(1,6)	2.9×10^{-12} exp(-160/T)
21 $OH+H_2=H_2O+HO_2$	(1,6)	5.5×10^{-12} exp(-2000/T)
22 $OH+HNO_3=NO_3+H_2O$	(1,6)	7.2×10^{-15} exp(785/T)
23	(1,6)	4.1×10^{-16} exp(1440/T)
24	(1,2)	1.9×10^{-33} exp(725/T)
25 $HO_2+HO_2+M=H_2O_2+M$	(1,6)	2.3×10^{-13} exp(600/T)
26	(1,2)	1.9×10^{-33} exp(890/T)
27	(1,11)	1.4×10^{-21} exp(2200/T) [H2O]
28 OH+CO=HO2+CO2	(1,6)	1.5×10^{-13} 1+(0.6M/2.55×10^{19})

Methane Chemistry

29 $OH+CH_4=CH_3O_2+H_2O$	(13,6)	7.44×10^{-18} T^2 exp(-1361/T)
30 $CH_3O_2+NO=NO_2+HO_2+HCHO$	(1,6)	4.2×10^{-12} exp(180/T)
31 $CH_3O_2+CH_3O_2=2HO_2+2HCHO+O_2$	(14,6)	9.1×10^{-14} exp(416/T)x 25exp(-1165/T)/(1+25exp(-1165/T)
32 $CH_3O_2+CH_3O_2=HCHO+CH_3OH+O_2$	(14,6)	9.1×10^{-14} exp(416/T)x (1-25exp(-1165/T))/(1+25exp(-1165/T)

33	$OH+CH_3OH=HO_2+HCHO+O_2$	(1,6)	$6.7x10^{-12}$ exp(-600/T)
34	$CH_3O_2+HO_2=CH_3OOH+O_2$	(1,6)	$3.8x10^{-13}$ exp(800/T)
35	$OH+HCHO=HO_2+CO+H_2O$	(1,6)	$1.0x10^{-11}$
36	$OH+CH_3OOH=CH_3O_2+H_2O$	(6,17)	$1.90x10^{-12}$ exp(190/T)
37	$OH+CH_3OOH=OH+HCHO$	(6,17)	$1.00x10^{-12}$ exp(190/T)

Nighttime chemistry

38	$NO+NO_3=NO_2+NO_2$	(1,6)	$1.5x10^{-11}$ exp(170/T)
39	$NO_2+NO_3+M=N_2O_5+M$	(1,4)	$2.2x10^{-30}$ $(T/300)^{-3.9}$
40		(1,5)	$1.5x10^{-12}$ $(T/300)^{-0.7}$
41	$NO_3+NO_3=NO_2+NO_2+O_2$	(1,6)	$8.5x10^{-13}$ exp(-2450/T)
42	$N_2O_5+M=NO_2+NO_3+M$	(8,9)	$2.2x10^{-3}$ $(T/300)^{-4.4}$ exp(-11080/T)
43		(8,10)	$9.7x10^{14}$ $(T/300)^{0.1}$ exp(-11080/T)
44	$NO_3+HO_2=HNO_3+O_2$	(6,8)	$9.2x10^{-13}$
45	$NO_3+HO_2=OH+NO_2+O_2$	(6,8)	$3.6x10^{-12}$
46	$NO_3+HCHO=HNO_3+HO_2+CO$	(1,6)	$5.8x10^{-16}$
47	$NO_3+C_2H_6=HNO_3+C_2H_5O_2$	(6,13)	$5.7x10^{-12}$ exp(-4426/T)
48	$NO_3+nC_4H_{10}=sC_4H_9O_2+HNO_3$	(6,13)	$2.76x10^{-12}$ exp(-3279/T)
49	$NO_3+C_2H_4=CH_2(NO_3)CHO+HO_2$	(6,13,18)	$4.88x10^{-18}$ T^2 exp(-2282/T)
50	$OH+CH_2(NO_3)CHO=HCHO+NO_2$	(6,17)	$4.95x10^{-12}$

51	$NO_3+C_3H_6=CH_3CH(NO_3)CHO+HO_2$	(6,13,18) 4.59×10^{-13} exp(-1157/T)
52	$OH+CH_3CH(NO_3)CHO=CH_3CHO+NO_2$	(6,17) 5.25×10^{-12}
53	$NO_3+CH_3CHO=HNO_3+CH_3COO_2$	(1,6) 1.4×10^{-12} exp(-1900/T)
54	$NO_3+C_5H_8=NO_3C_4H_6CHO+HO_2$	(6,13,18) 3.03×10^{-12} exp(-446/T)
55	$OH+NO_3C_4H_6CHO=MVK+NO_2$	(6,17) 4.16×10^{-11}
56	NO3+ORGNIT=MEMALD+GLYOX+$2NO_2$	(6,19) 7.0×10^{-14}
57	NO_3+DMS=CH_3SO+HCHO+HNO_3	(6,19) 1.9×10^{-13} exp(520/T)

Chemistry of the higher hydrocarbons

58	$OH+C_2H_6=C_2H_5O_2+H_2O$	(13,6) 1.51×10^{-17} T^2 exp(-492/T)
59	$C_2H_5O_2+NO=NO_2+HO_2+CH_3CHO$	(1,6) 8.7×10^{-12}
60	$C_2H_5O_2+HO_2=C_2H_5OOH+O_2$	(6,17) 7.5×10^{-13} exp(700/T)
61	$OH+C_2H_5OOH=C_2H_5O_2+H_2O$	(6,17) 1.90×10^{-12} exp(190/T)
62	$OH+C_2H_5OOH=CH_3CHO+OH+O_2$	(6,17) 1.0×10^{-11}
63	$C_2H_5O_2+CH_3O_2=2HO_2+CH_3CHO+HCHO$	(6,15) 2.0×10^{-13}
64	$C_2H_5O_2+C_2H_5O_2=2HO_2+2CH_3CHO$	(6,15) 9.8×10^{-14} exp(-100/T)
65	$OH+CH_3CHO=CH_3COO_2+H_2O$	(1,6) 6.0×10^{-12} exp(250/T)
66	$CH_3COO_2+NO_2+M=PAN+M$	(4,8) 2.7×10^{-28} $(T/300)^{-7.1}$
67		(5,8) 1.2×10^{-11} $(T/300)^{-0.9}$
68	$PAN+M=CH_3COO_2+NO_2+M$	(9,15) 5.5×10^{-3} exp(-12064/T)

69		(10,15) 3.9×10^{16} exp(-13628/T)
70	$CH_3COO_2+NO=NO_2+CH_3O_2+CO_2$	(6,15) 2.0×10^{-11}
71	$OH+PAN=NO_3+HCHO$	(6,8) 9.5×10^{-13} exp(-650/T)
72	$CH_3COO_2+CH_3O_2=HCHO+HO_2+CH_3O_2+CO_2$	(6,14) 5.1×10^{-12} exp(272/T) /1+4.4×10^{5} exp(-3910/T)
73	$CH_3COO_2+CH_3O_2=2HCHO+O_2$	(6,14) 5.1×10^{-12} exp(272/T) x 1 - 1/1+4.4×10^{5} exp(-3910/T)
74	$CH_3COO_2+CH_3COO_2=2CH_3O_2+2CO_2+O_2$	(6,15) 2.8×10^{-12} exp(530/T)
75	$OH+C_3H_8=C_3H_7O_2+H_2O$	(6,13) 1.5×10^{-17} T^2 exp(44/T)
76	$C_3H_7O_2+NO=NO_2+HO_2+CH_3COCH_3$	(6,16) 4.8×10^{-12}
77	$C_3H_7O_2+HO_2=C_3H_7OOH+O_2$	(6,17) 1.92×10^{-13} exp(1250/T)
78	$C_3H_7OOH+OH=C_3H_7O_2+H_2O$	(6,17) 1.00×10^{-12} exp(190/T)
79	$C_3H_7OOH+OH=CH_3COCH_3+OH+O_2$	(6,17) 2.42×10^{-11}
80	$OH+CH_3COCH_3=CH_3COCH_2O_2+H_2O$	(6,13) 5.34×10^{-18} T^2 exp(-230/T)
81	$CH_3COCH_2O_2+NO=NO_2+HCHO+CH_3COO_2$	(6,17) 5.3×10^{-12}
82	$CH_3COCH_2O_2+CH_3O_2=HO_2+2HCHO+CH_3COO_2$	(6,17) 1.2×10^{-12}
83	$C_3H_7O_2+CH_3O_2=2HO_2+HCHO+CH_3COCH_3+O_2$	(6,17) 4.0×10^{-14}
84	$OH+nC_4H_{10}=sC_4H_9O_2+H_2O$	(6,13) 1.51×10^{-17} T^2 exp(190/T)
85	$sC_4H_9O_2+NO=NO_2+HO_2+CH_3COC_2H_5$	(6,15) 4.1×10^{-12}
86	$sC_4H_9O_2+HO_2=sC_4H_9OOH+O_2$	(6,17) 2.24×10^{-13} exp(1250/T)
87	$sC_4H_9OOH+OH=sC_4H_9O_2+H_2O$	(6,17) 1.90×10^{-12} exp(190/T)

88	$sC_4H_9OOH+OH=CH_3COCH_3+OH+O_2$	(6,17) $3.21x10^{-11}$
89	$sC_4H_9O_2+CH_3O_2=2HO_2+HCHO+CH_3COC_2H_5$	(6,15) $1.0x10^{-14}$
90	$OH+CH_3COC_2H_5=CH_3COCHO_2CH_3+H_2O$	(6,13) $3.24x10^{-18}\ T^2\ exp(414/T)$
91	$CH_3COCHO_2CH_3+NO=NO_2+CH_3COO_2+CH_3CHO$	(6,15) $5.0x10^{-12}$
92	$CH_3COCHO_2CH_3+CH_3O_2=HO_2+HCHO+CH_3COO_2+CH_3CHO$	(6,15) $1.0x10^{-14}$
93	$OH+C_2H_4+M=HOC_2H_4O_2+M$	(4,8) $7.0x10^{-29}\ (T/300)^{-3.1}$
94		(5,8) $9.0x10^{-12}$
95	$HOC_2H_4O_2+NO=NO_2+HO_2+2HCHO$	(6,15) $9.0x10^{-12}$
96	$HOC_2H_4O_2+CH_3O_2=2HO_2+3HCHO+O_2$	(6,15) $1.0x10^{-12}$
97	$C_2H_4+O_3=HCHO+0.47CH_2OO+0.31CO+0.22CO_2+0.31H_2O+0.31H_2+0.2HO_2$	(6,8) $1.2x10^{-14}\ exp(-2630/T)$
98	$OH+C_3H_6+M=HOC_3H_6O_2+M$	(4,8) $8.0x10^{-27}\ exp(T/300)^{-3.5}$
99		(5,8) $3.0x10^{-11}$
100	$HOC_3H_6O_2+NO=NO_2+HO_2+HCHO+CH_3CHO$	(6,15) $9.0x10^{-12}$
101	$HOC_3H_6O_2+CH_3O_2=2HO_2+2HCHO+CH_3CHO+O_2$	(6,15) $1.0x10^{-14}$
102	$C_3H_6+O_3=HCHO+0.3CH_4+0.4CO+0.6CO_2+0.28OH+0.12CH_3OH+0.3HO_2+0.58CH_3O_2$	(6,15) $4.0x10^{-15}\ exp(-1900/T)$
103	$C_3H_6+O_3=CH_3CHO+0.24H_2+0.58CO+0.42CO_2+0.58H_2O+0.18HO_2$	(6,15) $2.6x10^{-15}\ exp(-1900/T)$
104	$OH+toluene=MEMALD+GLYOX+HO_2$	(6,13) $5.96x10^{-12}$

105	OH+toluene=TOLP1	(6,19) 1.19×10^{-13}
106	TOLP1+NO_2=ORGNIT	(6,19) 1.0×10^{-11}
107	TOLP1+HO_2=MEMALD+MGLYOX	(6,19) 1.0×10^{-11}
108	OH+MEMALD=MEMALD1	(6,15) 5.6×10^{-11}
109	MEMALD1+NO=NO_2+HO_2+MGLYOX+GLYOX	(6,15) 9.0×10^{-12}
110	MEMALD1+CH_3O_2=2HO_2+HCHO+MGLYOX+GLYOX	1.0×10^{-13}
111	OH+o-xylene=MEMALD+MGLYOX+HO_2	(6,13) 1.37×10^{-11}
112	OH+o-xylene=OXYL1	(6,19) 2.74×10^{-13}
113	OXYL1+NO_2=ORGNIT	(6,19) 1.0×10^{-11}
114	OXYL1+HO2=MEMALD+MGLYOX	(6,19) 1.0×10^{-11}
115	OH+ORGNIT=MEMALD+GLYOX+NO_2	
116	OH+MGLYOX=CH_3COO_2+CO+H_2O	(6,19) 1.72×10^{-11}
117	OH+GLYOX=HO_2+2CO+H_2O	(6,19) 1.14×10^{-11}

Chemistry of Isoprene

118	OH+C_5H_8+M=$HOC_5H_8O_2$+M	(6,19) 2.54×10^{-11} exp(410/T)
119	$HOC_5H_8O_2$+NO=NO_2+HO_2+MVK+HCHO	(6,19) 2.08×10^{-12} exp(180/T)
120	$HOC_5H_8O_2$+CH_3O_2=2HO_2+2HCHO+MVK	5.0×10^{-13}
121	$HOC_5H_8O_2$+HO_2=ISOPOOH+O_2	(6,19) 2.45×10^{-13} exp(1250/T)
122	OH+ISOPOOH=MVK+HCHO+OH	(6,19) 4.20×10^{-11}

123 $O_3+C_5H_8$=MVK+0.78CO+0.22CH_2OO+0.27HO_2 +0.27OH	(6,17) $7.86x10^{-15}$ exp(-1913/T)
124 OH+MVK+M=$HOMVKO_2$+M	(6,19) $4.13x10^{-12}$ exp(452/T)
125 $HOMVKO_2$+NO=NO_2+HO_2+HCHO+MGLYOX	(6,19) $2.46x10^{-12}$ exp(180/T)
126 $HOMVKO_2$+HO_2=MVKOOH+O_2	(6,19) $2.23x10^{-13}$ exp(1250/T)
127 OH+MVKOOH=MGLYOX+HCHO+OH	(6,19) $5.77x10^{-11}$
128 $HOMVKO_2$+CH_3O_2=2HO_2+2HCHO+MGLYOX	$2.0x10^{-12}$

Chemistry of the simple sulphur compounds

129 OH+SO_2+M=HO_2+SO_3+M	(1,4) $3.0x10^{-31}$ $(T/300)^{-3.3}$
130	(1,5) $1.5x10^{-12}$
131 CH_3O_2+SO_2=HO_2+HCHO+SO_3	(6,12) $4.0x10^{-17}$
132 OH+DMS=CH_3SO+HCHO	(6,19) $9.6x10^{-12}$ exp(-234/T)
133 OH+DMS=DMSO+HO_2	(6,19) $1.7x10^{-42}$ exp(7810/T) [O2] / (1+$5.5x10^{-31}$ exp (7460/T) [O2])
134 CH_3SO+O_3=CH_3SO_2+O_2	(1,6) $6.0x10^{-13}$
135 CH_3SO+NO_2=CH_3SO_2+NO	(6,19) $8.0x10^{-12}$
136 CH_3SO_2+O_3=CH_3SO_3+O_2	(6,19) $3.0x10^{-13}$
137 CH_3SO_3+NO_2=CH_3SO_3+NO	(6,19) $4.0x10^{-12}$
138 CH_3SO_2+O_2=CH_3O_2+SO_2	(6,19) $5.0x10^{13}$ exp-(1+8656/T)
139 CH_3SO_3+HO_2=MSA	(6,19) $5.0x10^{-11}$

140 $CH_3SO_3+O_2=CH_3O_2+SA$	(6,19) $5.0x10^{13}$ exp-(1+11071/T)
141 $CH_3SO_3+HCHO=MSA+HO_2+CO$	(6,19) $1.6x10^{-15}$
142 $OH+DMSO=DMSO_2+HO_2$	(6,19) $5.8x10^{-11}$
143 $OH+DMSO_2=DMSP$	(6,19) $1.0x10^{-12}$
144 $DMSP+NO=NO_2+HCHO+CH_3SO_2$	(6,19) $4.1x10^{-12}$ exp(180/T)
145 $DMSP+CH_3O_2=HO_2+HCHO+CH_3SO_2$	(6,19) $3.0x10^{-13}$

Aerosol Processes

146 SO2=SA	(20,21) $2.77x10^{-6}$
147 SA=wet deposition	(20,21) $1.16x10^{-6}$
148 MSA=wet deposition	(20,21) $1.16x10^{-6}$
149 N2O5+aerosol=NA+NA	(20,21) $5.0x10^{-6}$
150 HNO3+aerosol=NA	(20,21) $5.0x10^{-6}$
151 ORGNIT=NA	(20,21) $5.0x10^{-6}$

Photolysis Processes

152 $O_3+hv=O(^3P)+O_2$	
153 $O_3+hv=O(^1D)+O_2$	
154 $NO_2+hv=NO+O$	
155 $H_2O_2+hv=OH+OH$	

156 $HNO_3+hv=OH+NO_2$	
157 $HNO_4+hv=HO_2+NO_2$	
158 $NO_3+hv=NO+O_2$	
159 $NO_3+hv=NO_2+O$	
160 $N_2O_5+hv=NO_2+NO_2+O$	
161 $HCHO+hv=2HO_2+CO$	
162 $HCHO+hv=H_2+CO$	
163 $CH_3CHO+hv=CH_3O_2+HO_2+CO$	
164 $CH_3COCH_3+hv=CH_3COO_2+CH_3O_2+CO$	
165 $CH_3COC_2H_5+hv=C_2H_5O_2+CH_3O_2+CO$	
166 GLYOX+hv=HCHO+CO	
167 MGLYOX+hv=$CH_3COO_2+HO_2+CO$	
168 $CH_3OOH+hv=OH+HO_2+HCHO$	
169 $C_2H_5OOH+hv=OH+HO_2+CH_3CHO$	
170 $C_3H_7OOH+hv=OH+HO_2+CH_3COCH_3$	
171 $sC_4H_9OOH+hv=OH+HO_2+CH_3COC_2H_5$	
172 ISOPOOH+hv=OH+HO_2+MGLYOX+HCHO	
173 MVKOOH+hv=OH+HO_2+MGLYOX+HCHO	
174 PAN+hv=$NO_2+CH_3COO_2$	

Notes:

1. JPL (1994).
2. third order rate coefficient in cm^6 $molecule^{-2}$ s^{-1}.
3. M is the molecular concentration of third bodies, usually air molecules.
4. third order low pressure limiting rate coefficient in cm^6 $molecule^{-2}$ s^{-1}.
5. second order high pressure limiting rate coefficient in cm^3 $molecule^{-1}$ s^{-1}.
6. units in cm^3 $molecule^{-1}$ s^{-1}.
7. equilibrium constant expression taken from JPL (1994) and given as ratio of forward and back rate coefficients.
8. IUPAC IV data evaluation, Atkinson et al. (1992).
9. second order low pressure limiting rate coefficient in cm^3 $molecule^{-1}$ s^{-1}.
10. first order high pressure limiting rate coefficient in s^{-1}.
11. multiplying factor to take into account water vapour catalysis.
12. EMEP mechanism, Simpson (1992).
13. Atkinson (1994).
14. Lightfoot et al. (1992).
15. LACTOZ review, Wirtz et al. (1994).
16. IUPAC V data evaluation, Atkinson et al. (1996).
17. Master Chemical Mechanism, Jenkin et al. (1996).
18. nighttime chemistry of NO3-addition products.
19. Jenkin (1996).
20. first order rate coefficient in s^{-1}.
21. Metcalfe et al. (1996).

TABLE 3. Global emissions of the major tropospheric trace gases in 1992 and 2015 in the various scenario cases.

Scenario case	1992 base case	2015 IS92a	2015 CRP	2015 MFR
Tg yr^{-1}				
NO_x, fuel combustion	21.0	30.45	24.0	22.1
NO_x, biomass burning	8.0	8.8	8.8	8.8
CO, fuel combustion	425.0	488.8	395.0	395.0
CO, biomass burning	500.0	550.0	550.0	550.0
CH_4, human activities	155.0	186.0	186.0	186.0
CH_4, biomass burning	40.0	44.0	44.0	44.0
VOC, human activities	100%	120%	120%	120%
SO_2, fuel combustion	65.1	87.9	67.0	12.3
SO_2, biomass burning	2.2	2.4	2.4	2.4
NH_3, human activities	37.1	44.5	44.5	44.5
NH_3,biomass burning	5.9	6.5	6.5	6.5

Notes:
a. CRP: current reduction plans, that is, NO_x and SO_2 emissions for the UN ECE region, calculated on the basis of the policies that governments have agreed (United Nations 1996).
b. MFR: the reference scenario of IIASA for the UN ECE region, calculated on the basis of the NO_x emission controls which are technically feasible for the year 2010 (Amann et al. 1997). About 80% reduction additionally assumed globally on SO_2 emissions from human activities.

TABLE 4. Estimates of the mean tropospheric hydroxyl radical concentration obtained by different indirect techniques and the STOCHEM model calculated concentration.

Study		Mean hydroxyl radical concentration, molecules cm^{-3}
methyl chloroform method		
Lovelock (1977)		0.7
Singh (1977a)		0.2-0.6
Singh (1977b)		0.41
Neely and Plonka (1978)		1.15
Prinn et al. (1992)		0.81
Prinn et al. (1995)		0.97
^{14}CO method		
Weinstock (1969)		1.2
Volz et al. (1981)		0.65
chemistry-transport models		
Crutzen and Fishman (1977)	2-D	0.8
Derwent and Curtis (1977)	2-D	0.76
Chang et al. (1977)	1-D	1.68
Wuebbles et al. (1994)	2-D	0.83
Derwent (1996)	2-D	0.74
This study (STOCHEM)	3-D	0.77

TABLE 5. Annual budgets and inventories for the major tropospheric free radical species in 1992 and 2015.

Scenario case	1992 base case	2015 IS92a	2015 CRP	2015 MFR

Free radical burdens, annually averaged over the entire model domain in 10^{30} molecules.

OH	5.92	6.01	6.00	5.98
HO_2	402	417	415	416
CH_3O_2	239	263	265	264
RO_2	344	369	373	374

Annual mean tropospheric OH concentration, 10^6 molecule cm^{-3} .

OH	0.77	0.79	0.78	0.78

Free radical budget terms, annually averaged over the entire model domain in 10^{36} molecules.

'new OH' sources	66	72	72	71
OH to HO_2 & RO_2	110	122	120	119
HO_2& RO_2 to OH	52	59	56	56
'new HO_2 & RO_2' sources	48	55	53	52
'new OH' sinks	8	8	8	8
'new HO_2 & RO_2' sinks	107	119	117	116

Notes:
a. the expressions 'new sources' and 'new sinks' are used to distinguish those processes which merely recycle the radicals continuously from those which generate or destroy them permanently.

TABLE 6. Annual budgets for methane in the years 1992 and 2015 integrated over the entire model domain.

Scenario case	1992 base case	2015 IS92a	2015 CRP	2015 MFR
Source terms, Tg yr^{-1}				
Emissions	485	537	537	537
Sink terms, Tg yr^{-1}				
$OH+CH_4$	455	544	541	539
Burden, Tg	3953	4741	4744	4746
Turnover time, years	8.68	8.72	8.77	8.81

TABLE 7. Illustrative results from the IPCC Delta methane intercomparison for sensitivity and methane turnover time and the analogous results from STOCHEM.

Model		Sensitivity , %	Lifetime, years
U. Cambridge	2-D	-0.17%	13.2
AER	2-D	-0.18%	11.9
TROPOS UKMO	2-D	-0.20%	9.8
LLNL	3-D	-0.22%	8.7
AER	2-D	-0.26%	12.5
U. Oslo	3-D	-0.34%	9.2
LLNL	2-D	-0.35%	11.5
IPCC assessment		-0.26%	8.7±1.6
STOCHEM	3-D	-0.205%	8.7

Notes:

a. details of the Delta Methane intercomparison experiment are available in IPCC (1995).

b. Sensitivity is defined as the percentage change in OH+methane removal coefficient in yr^{-1} for each percentage increase in tropospheric methane concentrations.

TABLE 8. Annual budgets for ozone in the years 1992 and 2015 integrated over the entire model domain.

Scenario case	1992 base case	2015 IS92a	2015 CRP	2015 MFR
Ozone production terms, Tg yr^{-1}.				
strat. influx	865	865	865	865
$NO+HO_2$	3007	3403	3274	3235
$NO+CH_3O_2$	893	1051	1038	1029
$NO+RO_2$	712	761	753	749
Total	5477	6080	5937	5891
Ozone destruction terms, Tg yr^{-1}				
O^1D+H_2O	2171	2369	2344	2338
O_3+OH	394	436	424	420
O_3+HO_2	1093	1245	1211	1205
O_3+HC	102	106	106	106
deposition	1510	1664	1624	1605
other losses	214	268	236	226
Total	5484	6088	5947	5900

TABLE 9. Annual budgets for PAN for the years 1992 and 2015 integrated over the entire model domain.

Scenario case	1992 base case	2015 IS92a	2015 CRP	2015 MFR
PAN sources, Tg yr^{-1}				
isoprene	0.71	0.71	0.71	0.71
butane	0.19	0.22	0.22	0.22
propylene	0.09	0.10	0.10	0.10
ethane	0.03	0.03	0.03	0.03
toluene	0.02	0.02	0.02	0.02
propane	0.01	0.02	0.02	0.02
o-xylene	0.01	0.01	0.01	0.01
acetone	0.006	0.008	0.008	0.008
PAN burden, Gg = 10^9 g	2.96	3.55	3.41	3.32
Lifetime, hours	24.2	27.7	26.6	26.0

TABLE 10. Annual hydrogen peroxide budgets for the years 1992 and 2015 integrated over the entire model domain.

Scenario case	1992 base case	2015 IS92a	2015 CRP	2015 MFR
H_2O_2 sources, Tg yr^{-1}				
	930	1000	988	989
H_2O_2 sinks, Tg yr^{-1}				
H_2O_2 + hv	270	291	288	291
H_2O_2+OH	215	231	227	228
SO_2 oxid^n in cloud droplet	18	21	18	9
dry dep^n	83	89	88	90
wet dep^n	344	369	366	371
H_2O_2 burden, Tg	2.53	2.66	2.68	2.71
H_2O_2 lifetime, hours	23.8	23.8	23.8	23.8

TABLE 11. Annual sulphur dioxide budgets and inventories for the years 1992 and 2015 integrated over the entire model domain.

Scenario case	1992 base case	2015 IS92a	2015 CRP	2015 MFR
Source terms, Tg S yr^{-1}				
SO_2 emission	76.2	99.2	76.5	28.4
DMS oxidn	11.7	11.7	11.7	11.7
Total source	87.9	110.9	88.2	40.1
Sink terms, Tg S yr^{-1}				
SO_2 + OH	14.2	18.5	14.4	6.4
SO_2 aq oxidn	23.4	27.3	25.4	14.4
SO_2 dry depn	29.1	38.5	28.0	9.0
SO_2 wet dep	21.3	26.6	20.4	10.4
Total sink	88.0	110.9	88.2	40.1
Sulphur dioxide inventory, Tg S				
Inventory, Tg	0.44	0.54	0.42	0.20
Sulphur dioxide loss lifetime, days				
Lifetime, days	1.81	1.79	1.75	1.83

TABLE 12. Annual sulphate aerosol budgets and inventories for the years 1992 and 2015 integrated over the entire model domain.

Scenario case	1992 base case	2015 IS92a	2015 CRP	2015 MFR
Source terms, Tg S yr^{-1}				
SO_2 + OH	14.2	18.5	14.4	6.4
DMS oxidn	0.3	0.4	0.4	0.4
SO_2 aq oxid	23.4	27.3	27.4	14.4
Total source	38.0	46.2	40.2	21.1
Sink terms, Tg S yr^{-1}				
SO_4 dry depn	4.2	5.2	4.4	2.0
SO_4 wet dep	33.8	41.0	35.8	19.2
Total sink	38.0	46.2	40.2	21.1
Sulphate aerosol inventory, Tg				
Inventory, Tg	0.43	0.54	0.45	0.22
Sulphate aerosol loss lifetimes, days				
Lifetime, days	4.2	4.3	4.1	3.8

Captions to the Figures

Figure 1. The monthly mean distribution of the mixing ratios of the hydroxyl radical in the model surface layer for a) July 1992 and b) July 2015 and c) their differences.

Figure 2. The monthly mean distribution of surface ozone concentrations for a) July 1992 and b) July 2015 and c) their differences.

Figure 3. The monthly mean distribution of surface ozone concentrations for a) January 1992 and b) January 2015 and c) their differences.

Figure 4. The framework of interlinking reactions which form and destroy PAN in the STOCHEM model.

Figure 5. The monthly mean distribution of surface PAN concentrations for a) July 1992 and b) July 2015 and c) their differences.

Figure 6. The monthly mean distribution of surface hydrogen peroxide concentrations for a) July 1992 and b) July 2015 and c) their differences.

Figure 7. The spatial distribution of each of the sulphur deposition fluxes in the global sulphur cycle for 1992 emissions.

Figure 8. The spatial distribution of each of the oxidised nitrogen deposition fluxes in the global nitrogen cycle for 1992 emissions.

Figure 9. The spatial distribution of each of the reduced nitrogen deposition fluxes in the global nitrogen cycle for 1992 emissions.

Figure 10. The European dry sulphur deposition field, based on a) 1994 EMEP observations and b) STOCHEM for 1992 emissions.

Figure 11. The European wet sulphur deposition field, based on a) 1994 EMEP observations and b) STOCHEM for 1992 emissions.

Figure 12. The European total sulphur deposition field, based on a) 1994 EMEP observations and b) STOCHEM for 1992 emissions.

Figure 13. The European wet oxidised nitrogen deposition field, based on a) 1994 EMEP observations and b) STOCHEM for 1992 emissions.

Figure 14. The European wet reduced nitrogen deposition field, based on a) 1994 EMEP observations and b) STOCHEM for 1992 emissions.

Figure 15. Total sulphur deposition in the a). 1992 base case, b). 2015-IS92a c). 2015-CRP and d). 2015-MFR scenario cases.

Figure 16. Total nitrogen deposition in the a). 1992 base case, b). 2015-IS92a c). 2015-CRP and d). 2015-MFR scenario cases.

Figure 17. The distribution of ozone across Europe as indicated by a) the EMEP 95-percentile hourly mean ozone concentrations for April to September 1995 and b) the mean monthly concentrations from STOCHEM for July.

Figure 18. Scatter plots of a). AOT_{60} and b). AOT_{40} crops against the 95-percentile hourly mean ozone concentrations from April to September 1995 for the 96 EMEP monitoring network sites.

Figure 19. The European AOT_{60} ozone distribution based on a) 1995 EMEP observations and b) STOCHEM for 1992 emissions.

Figure 20. The European AOT_{40} ozone distribution based on a) 1995 EMEP observations and b) STOCHEM for 1992 emissions.

Figure 21. Ozone distributions for July across Europe calculated for a-d) 2015 scenario cases.

Figure 22. Distributions of AOT_{60} exposures across Europe calculated for a-d) 2015 scenario cases.

Figure 23. Distributions of AOT_{40} crops across Europe calculated for a-d) 2015 scenario cases.

Figure 1. The monthly mean distribution of the mixing ratios of the hydroxyl radical in the model surface layer for a) July 1992 and b) July 2015 and c) their differences.

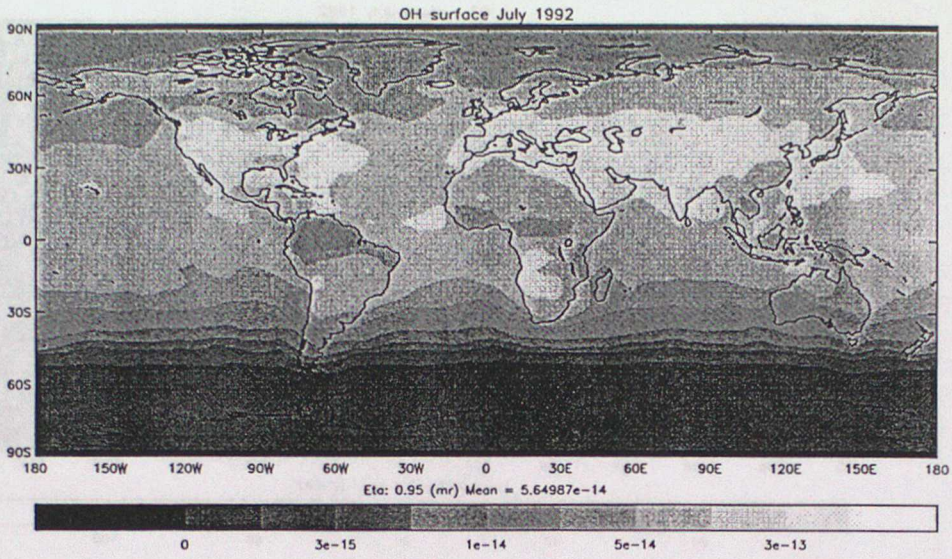

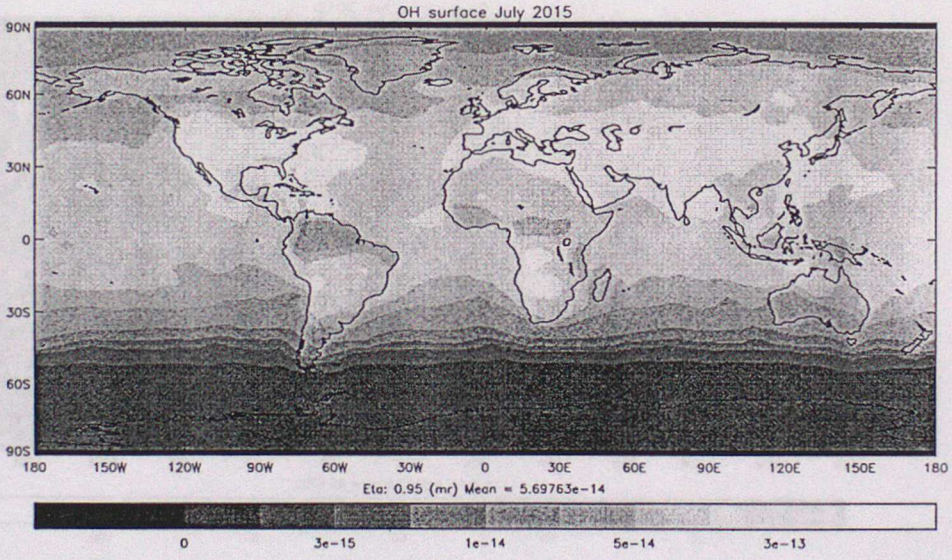

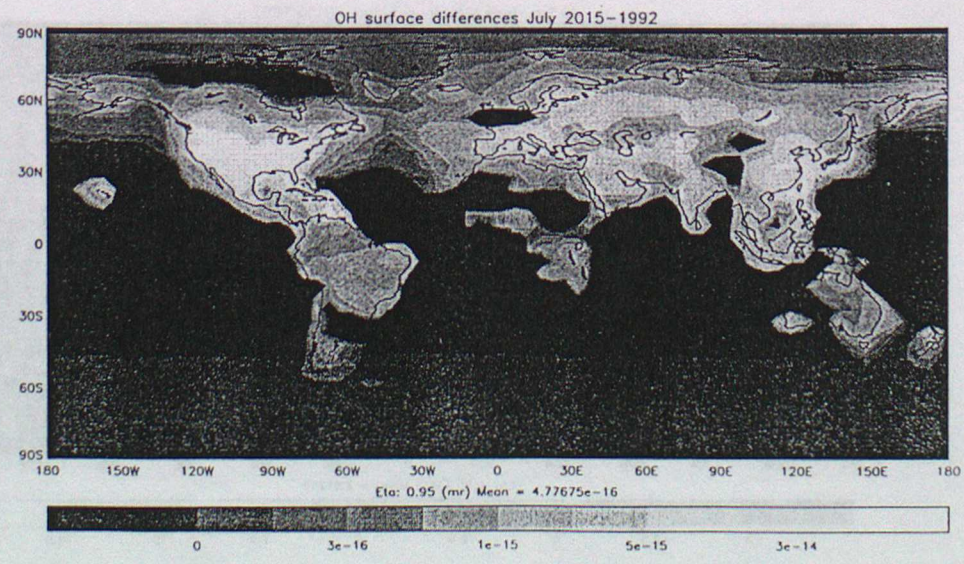

Figure 2. The monthly mean distribution of surface ozone concentrations for a) July 1992 and b) July 2015 and c) their differences.

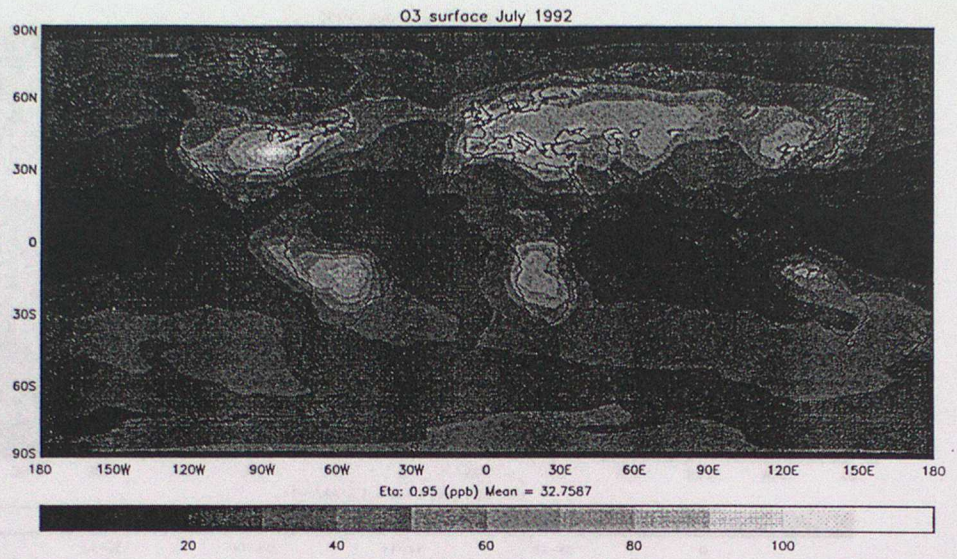

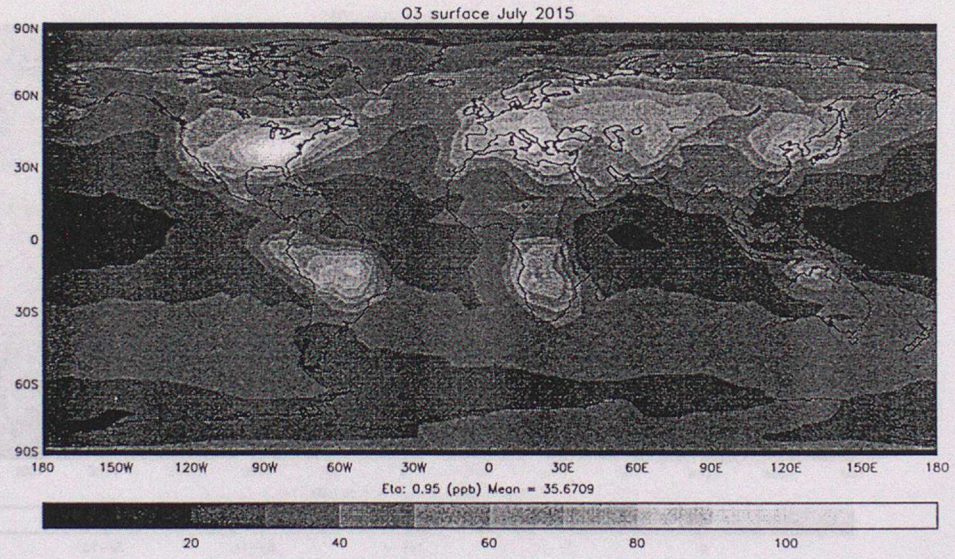

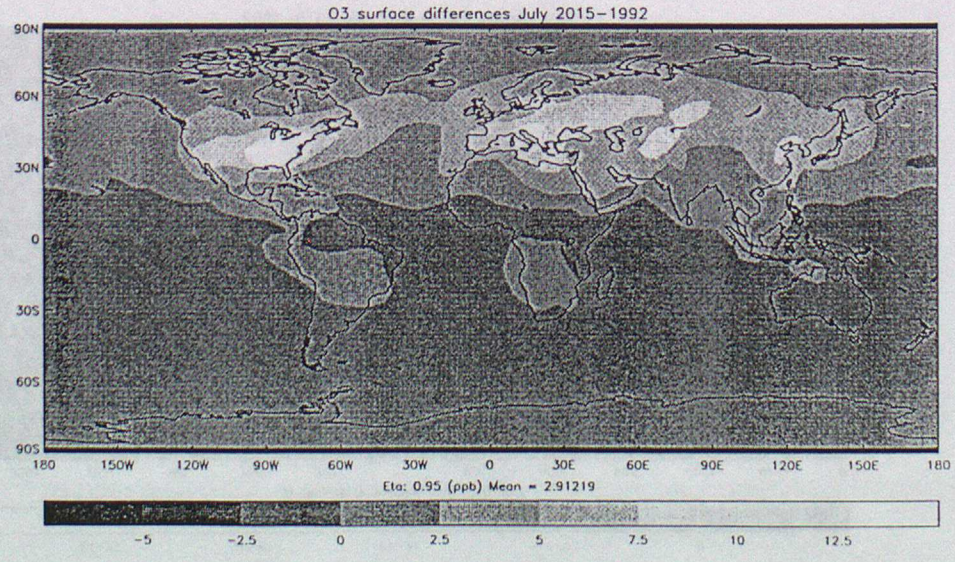

Figure 3. The monthly mean distribution of surface ozone concentrations for a) January 1992 and b) January 2015 and c) their differences.

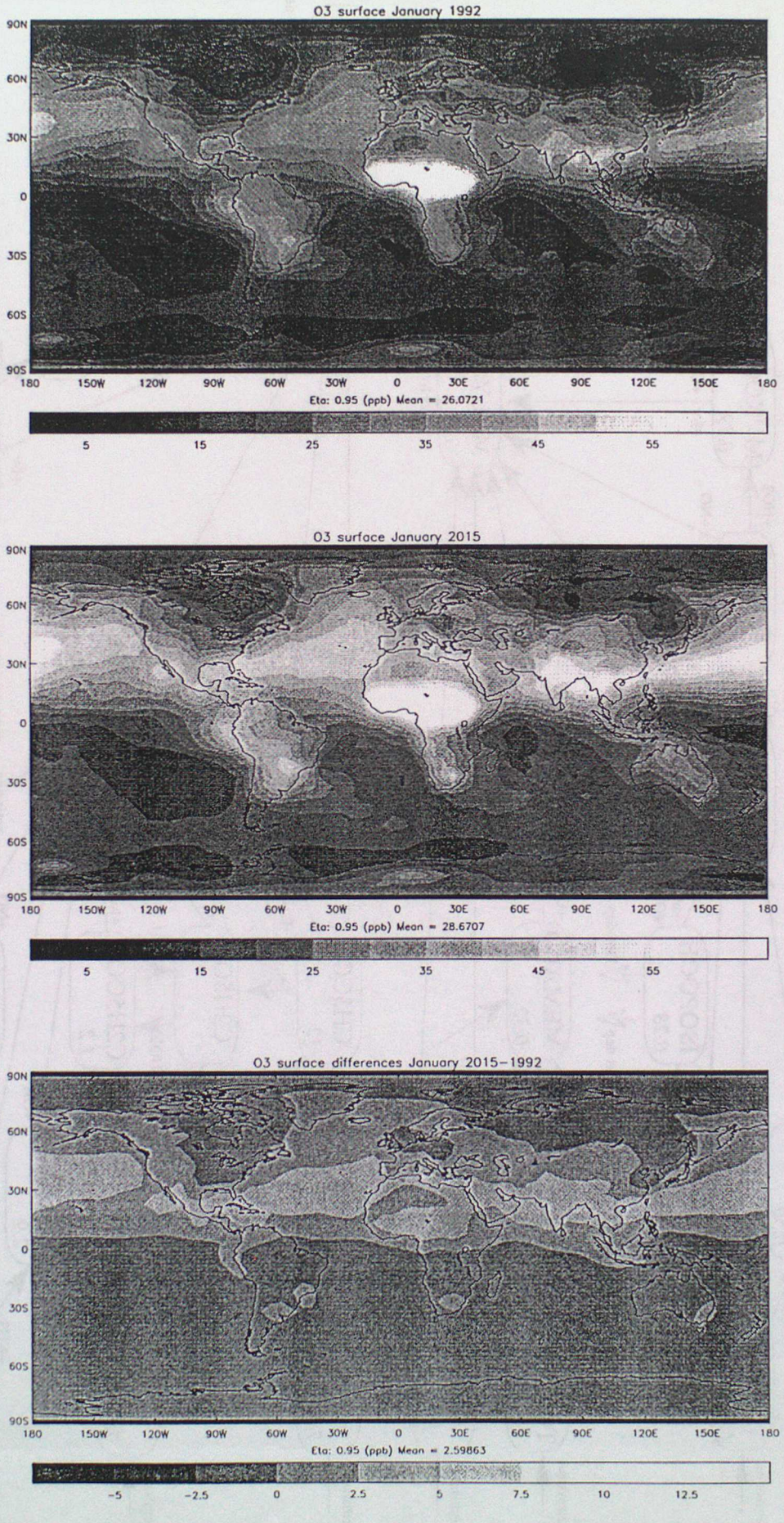

Figure 4. The framework of interlinking reactions which form and destroy PAN in the STOCHEM model.

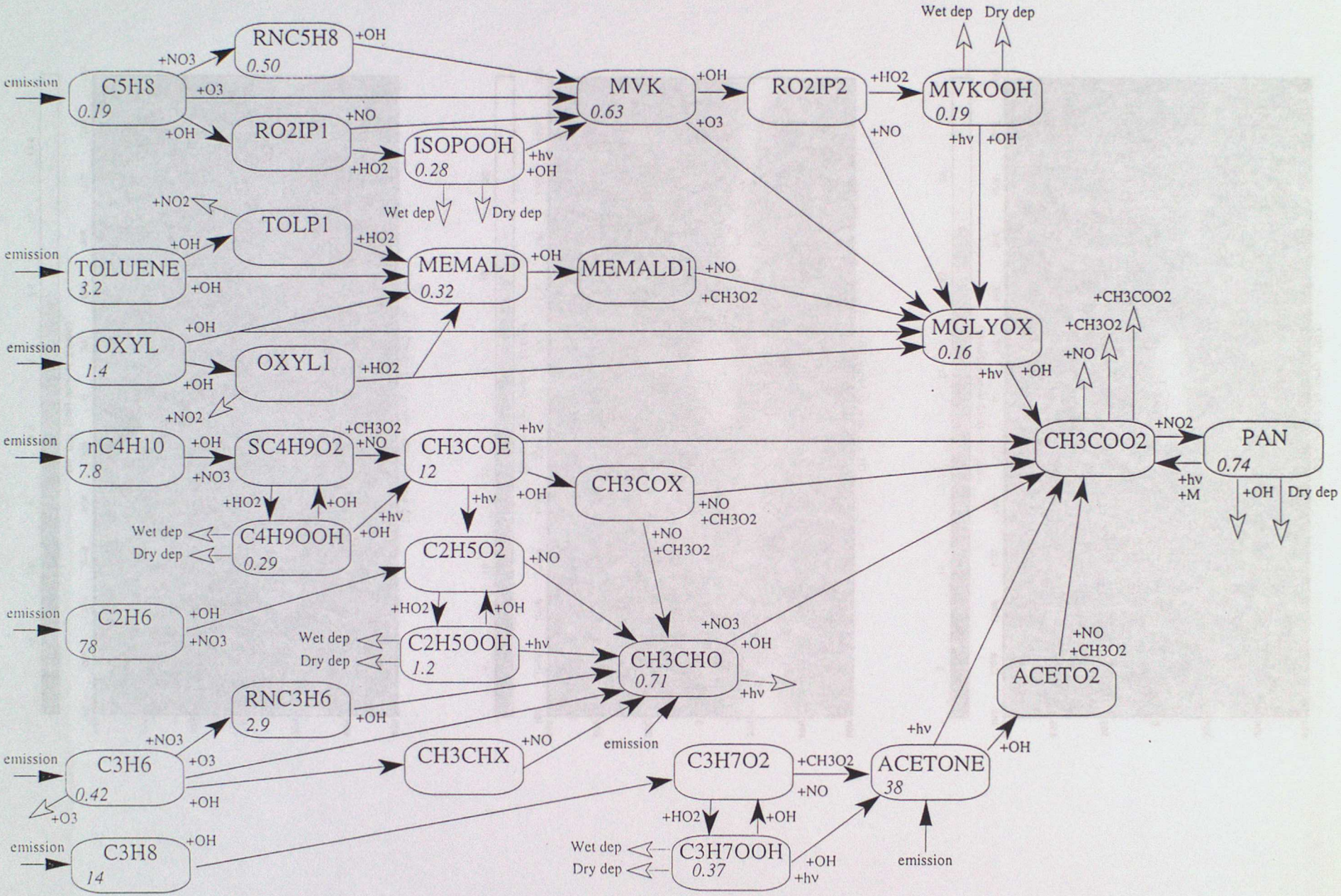

Figure 5. The monthly mean distribution of surface PAN concentrations for a) July 1992 and b) July 2015 and c) their differences.

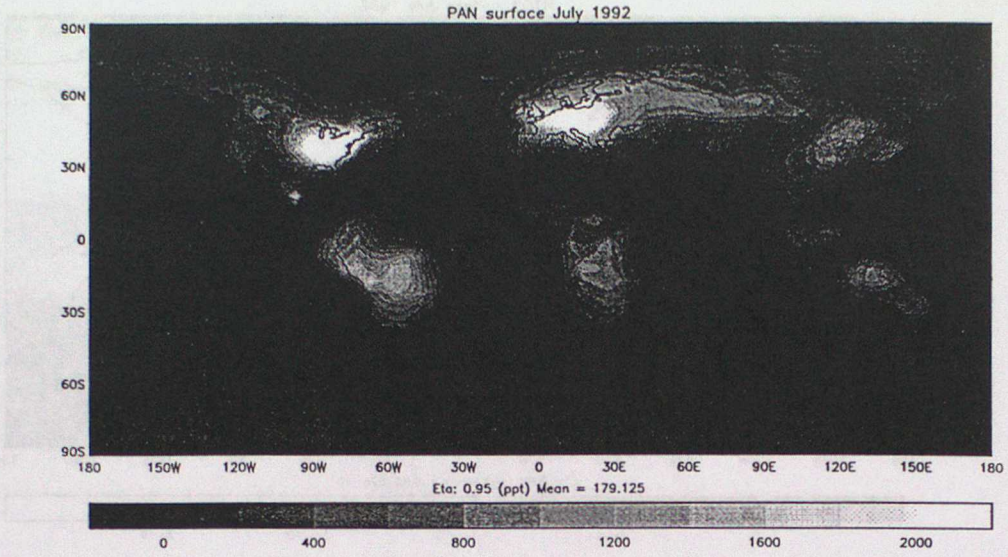

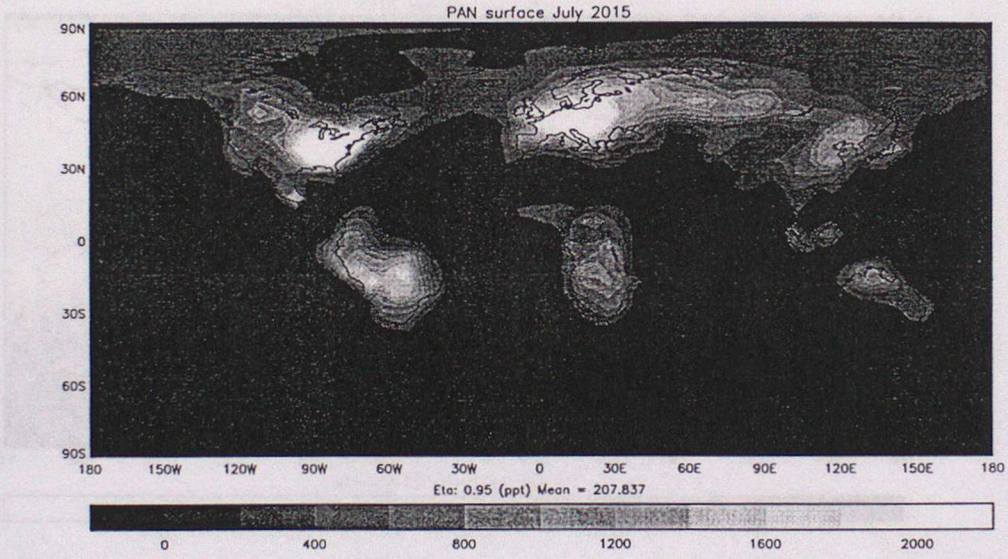

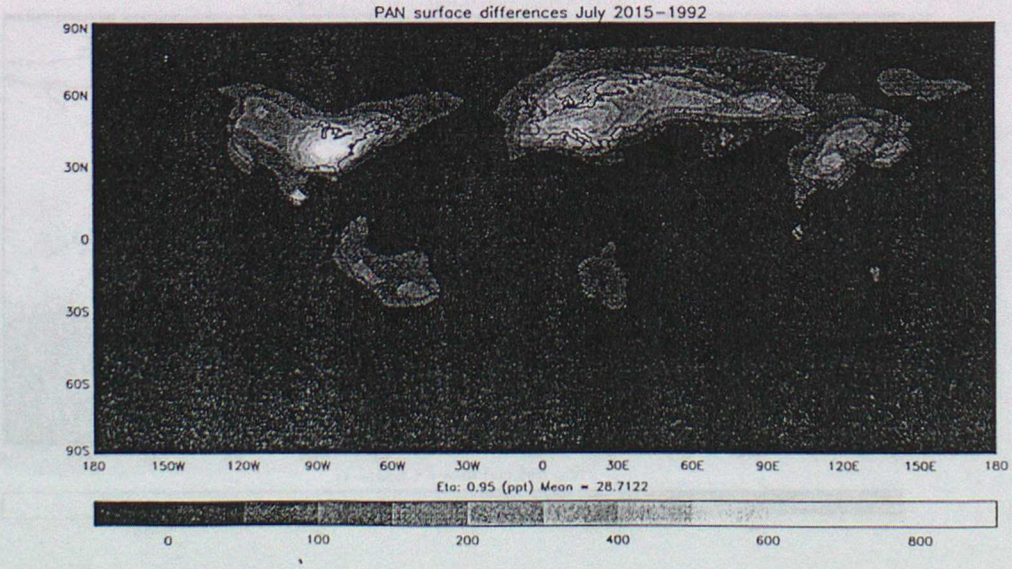

Figure 6. The monthly mean distribution of surface hydrogen peroxide concentrations for a) July 1992 and b) July 2015 and c) their differences.

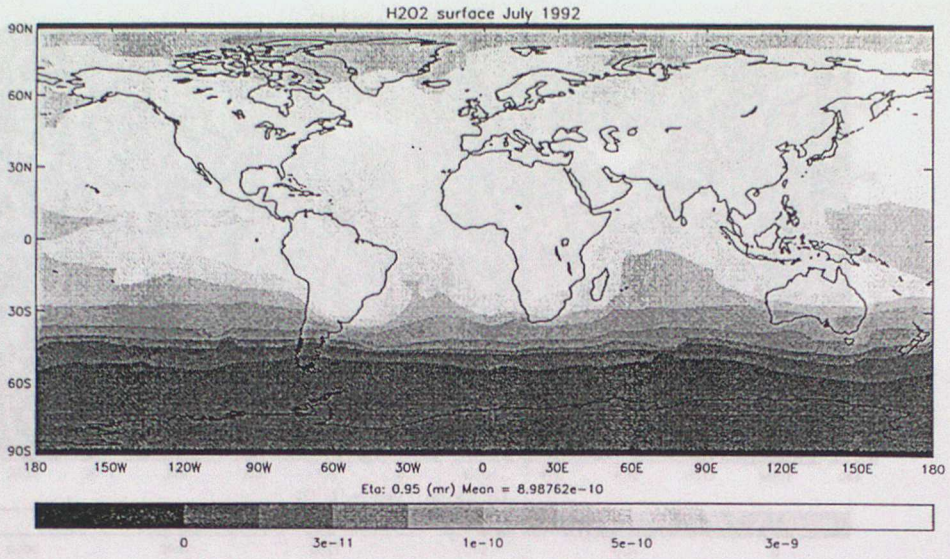

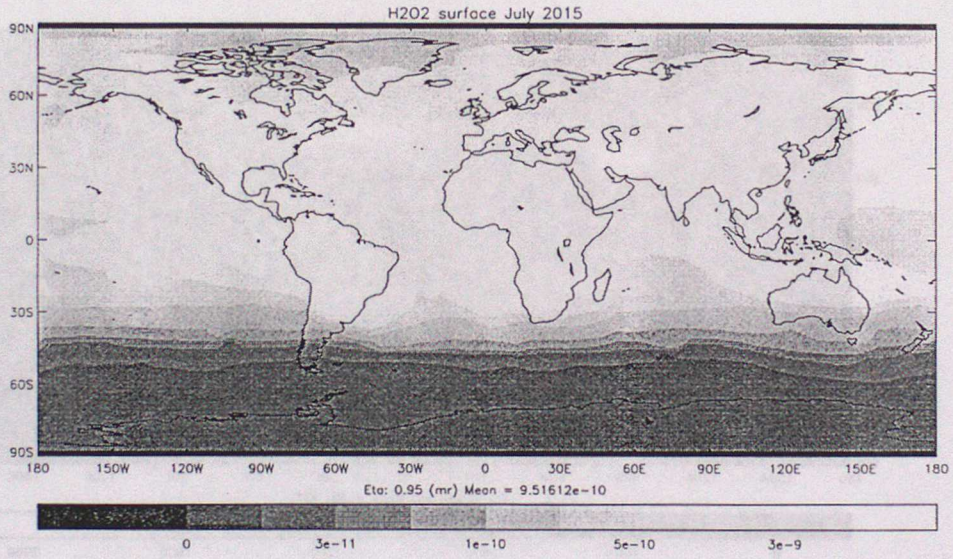

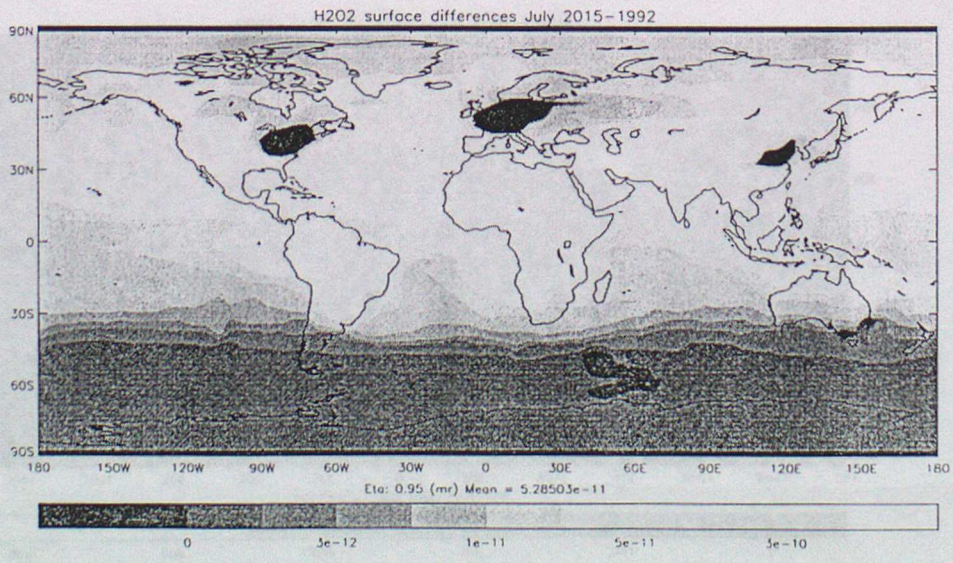

Figure 7. The spatial distribution of each of the sulphur deposition fluxes in the global sulphur cycle for 1992 emissions.

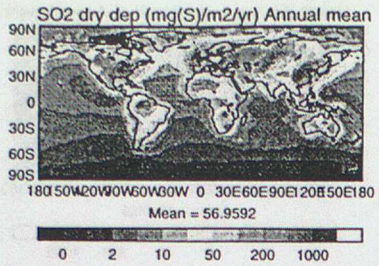

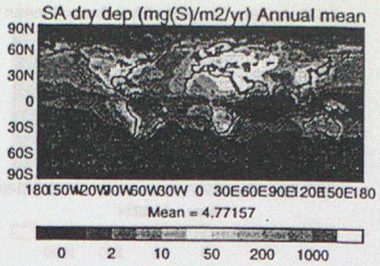

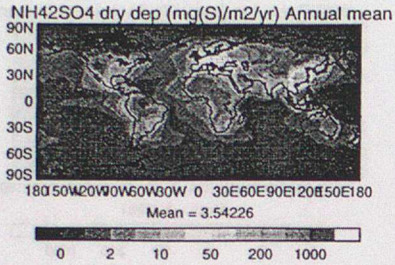

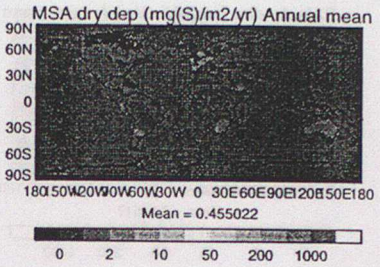

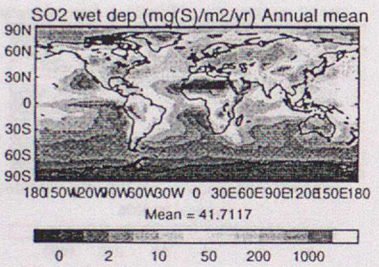

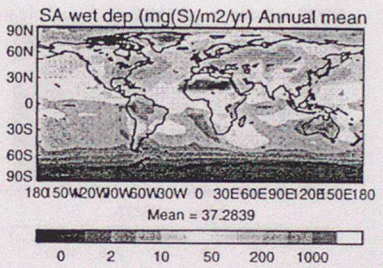

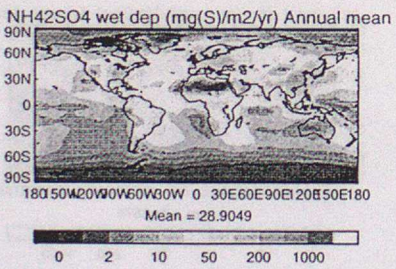

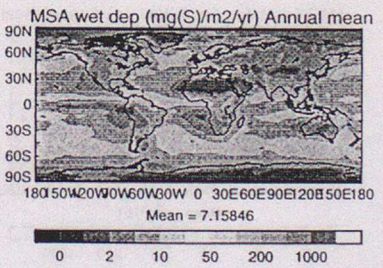

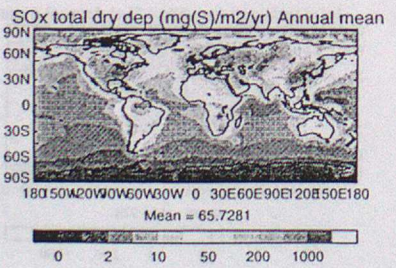

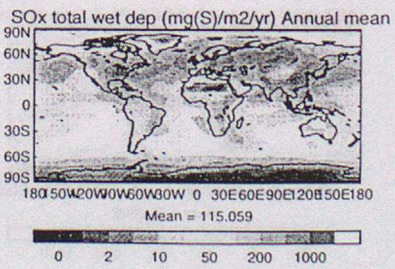

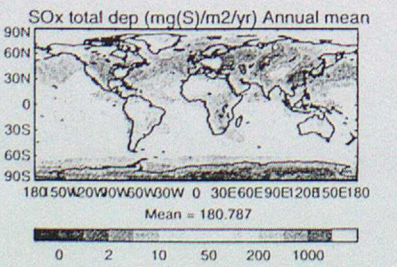

Figure 8. The spatial distribution of each of the oxidised nitrogen deposition fluxes in the global nitrogen cycle for 1992 emissions.

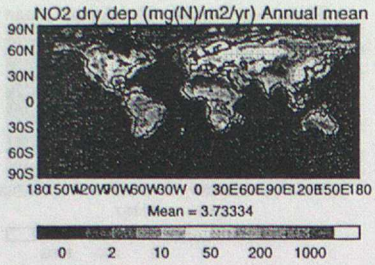

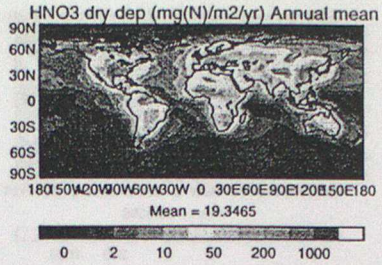

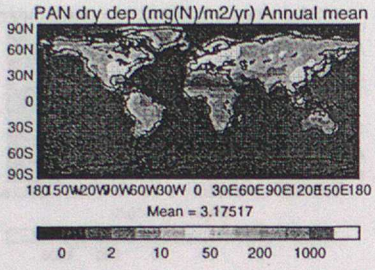

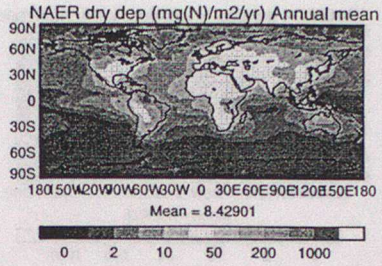

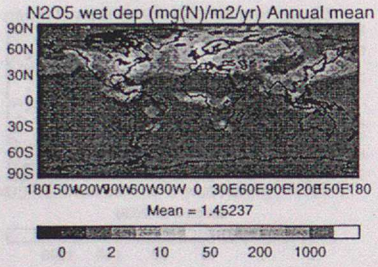

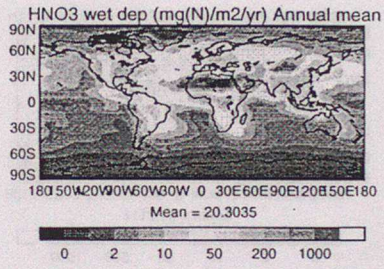

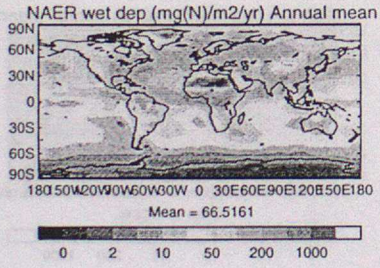

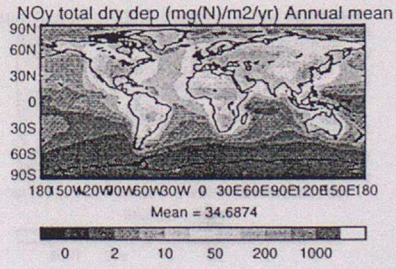

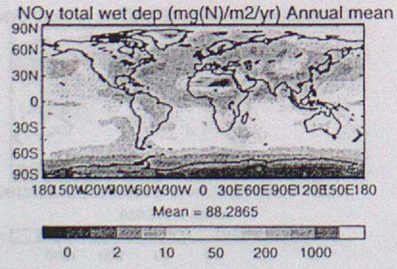

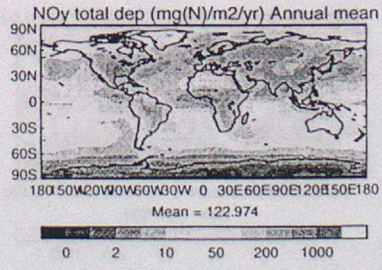

Figure 9. The spatial distribution of each of the reduced nitrogen deposition fluxes in the global nitrogen cycle for 1992 emissions.

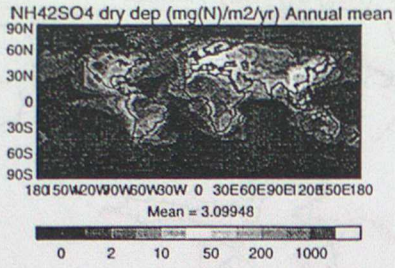

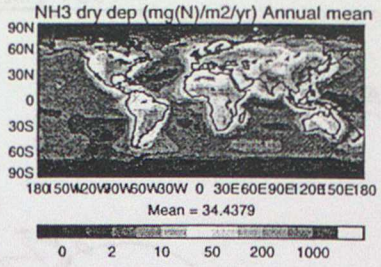

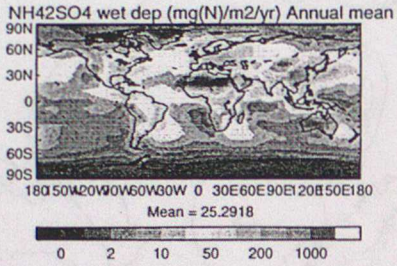

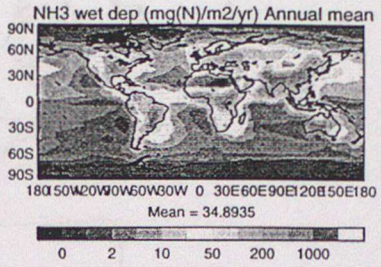

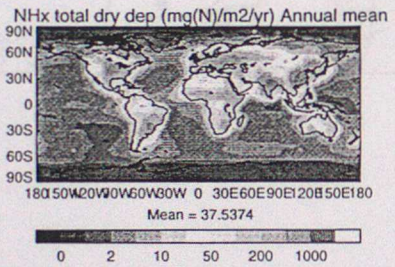

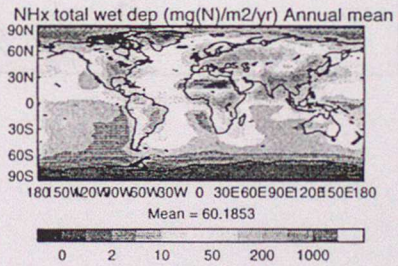

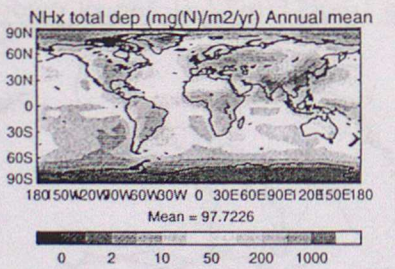

Figure 10. The European dry sulphur deposition field, based on a) 1994 EMEP observations and b) STOCHEM for 1992 emissions.

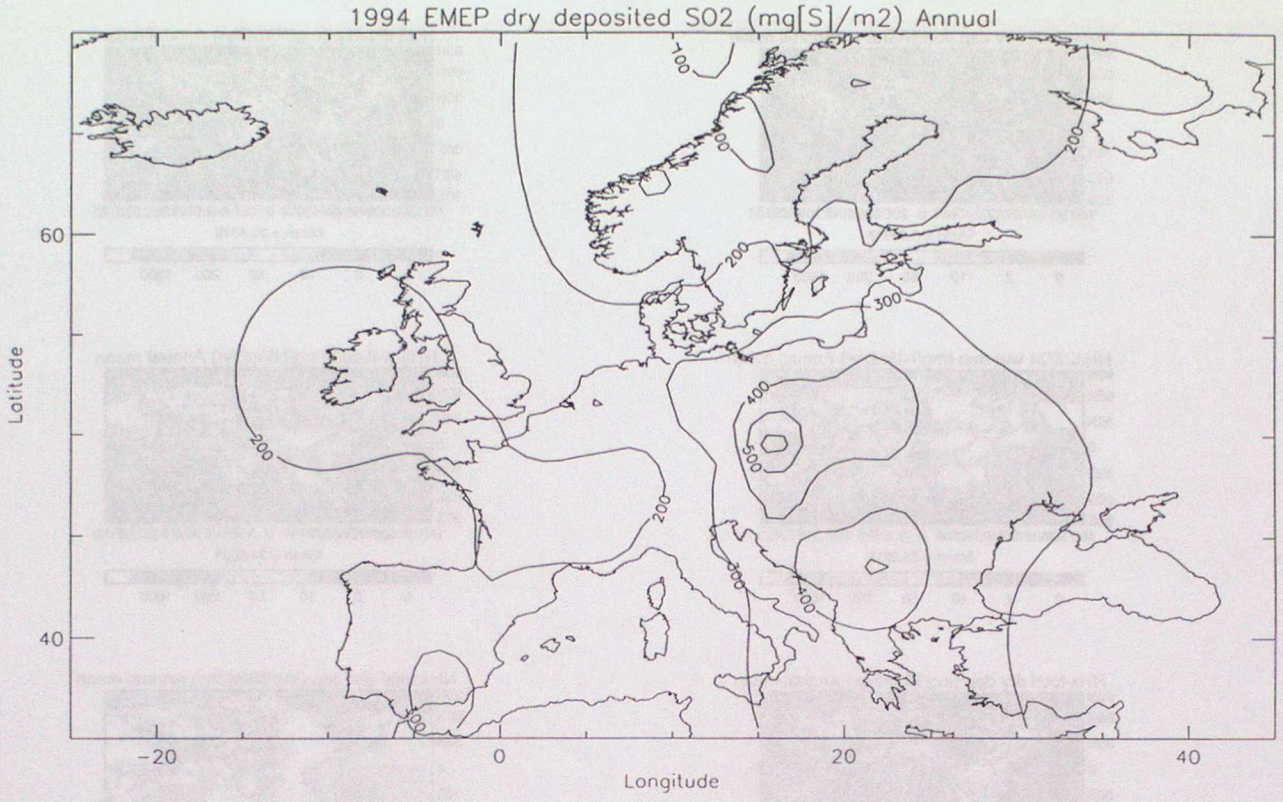

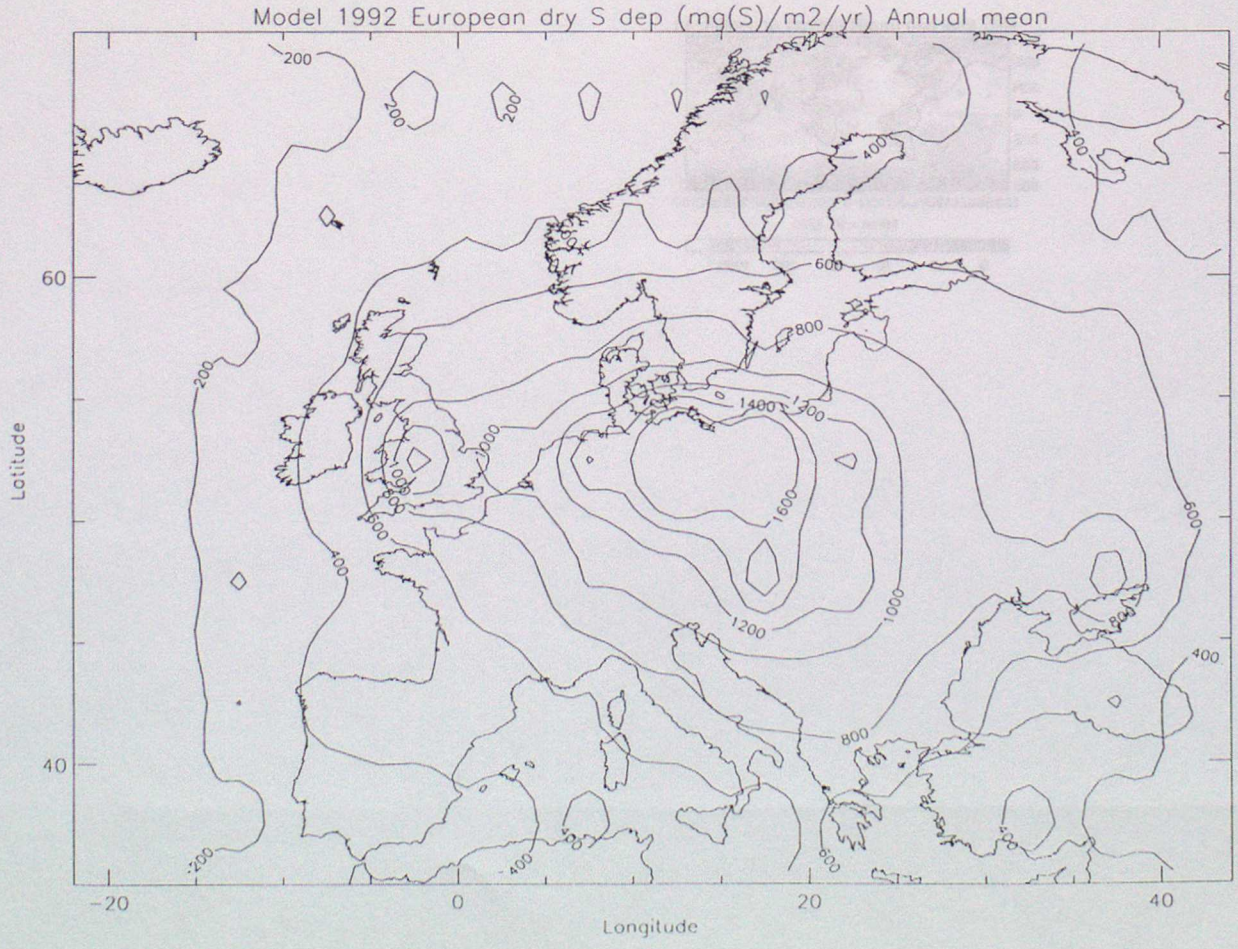

Figure 11. The European wet sulphur deposition field, based on a) 1994 EMEP observations and b) STOCHEM for 1992 emissions.

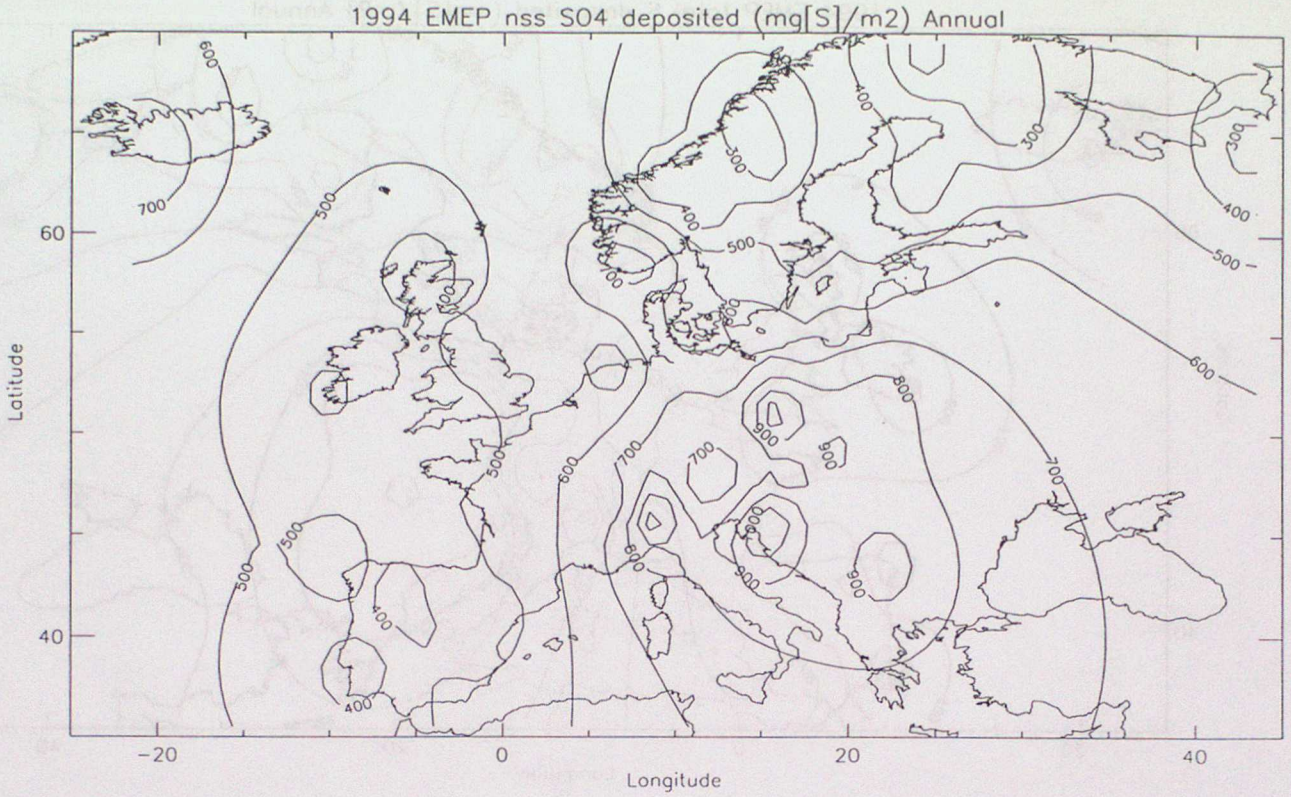

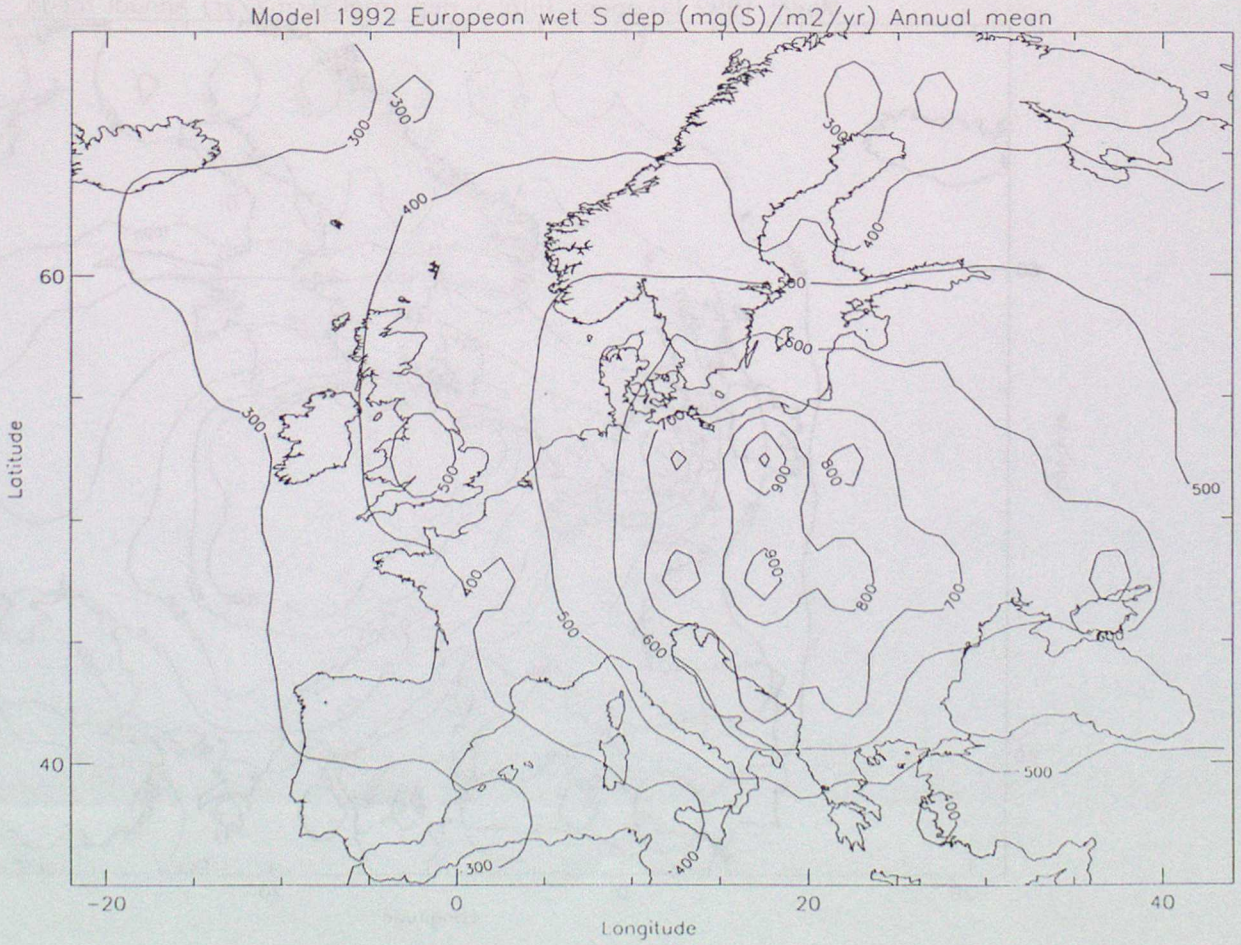

Figure 12. The European total sulphur deposition field, based on a) 1994 EMEP observations and b) STOCHEM for 1992 emissions.

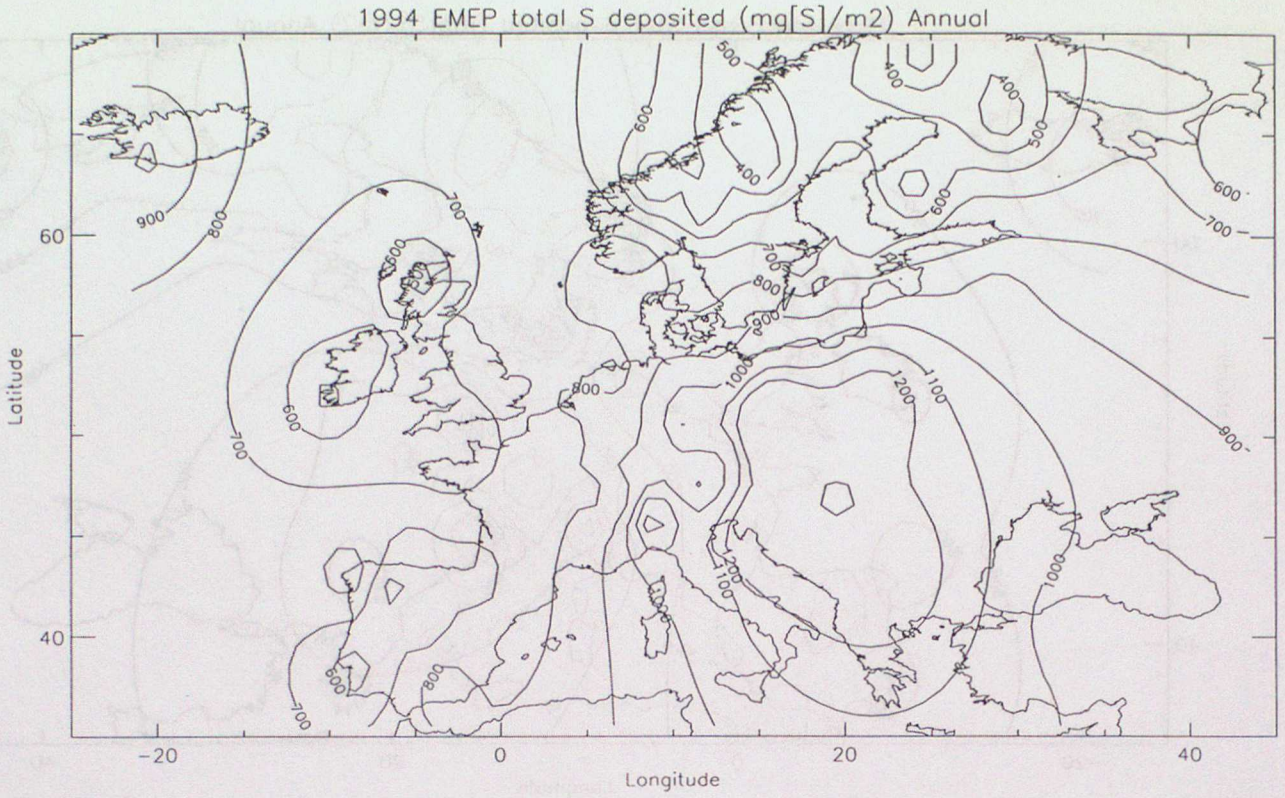

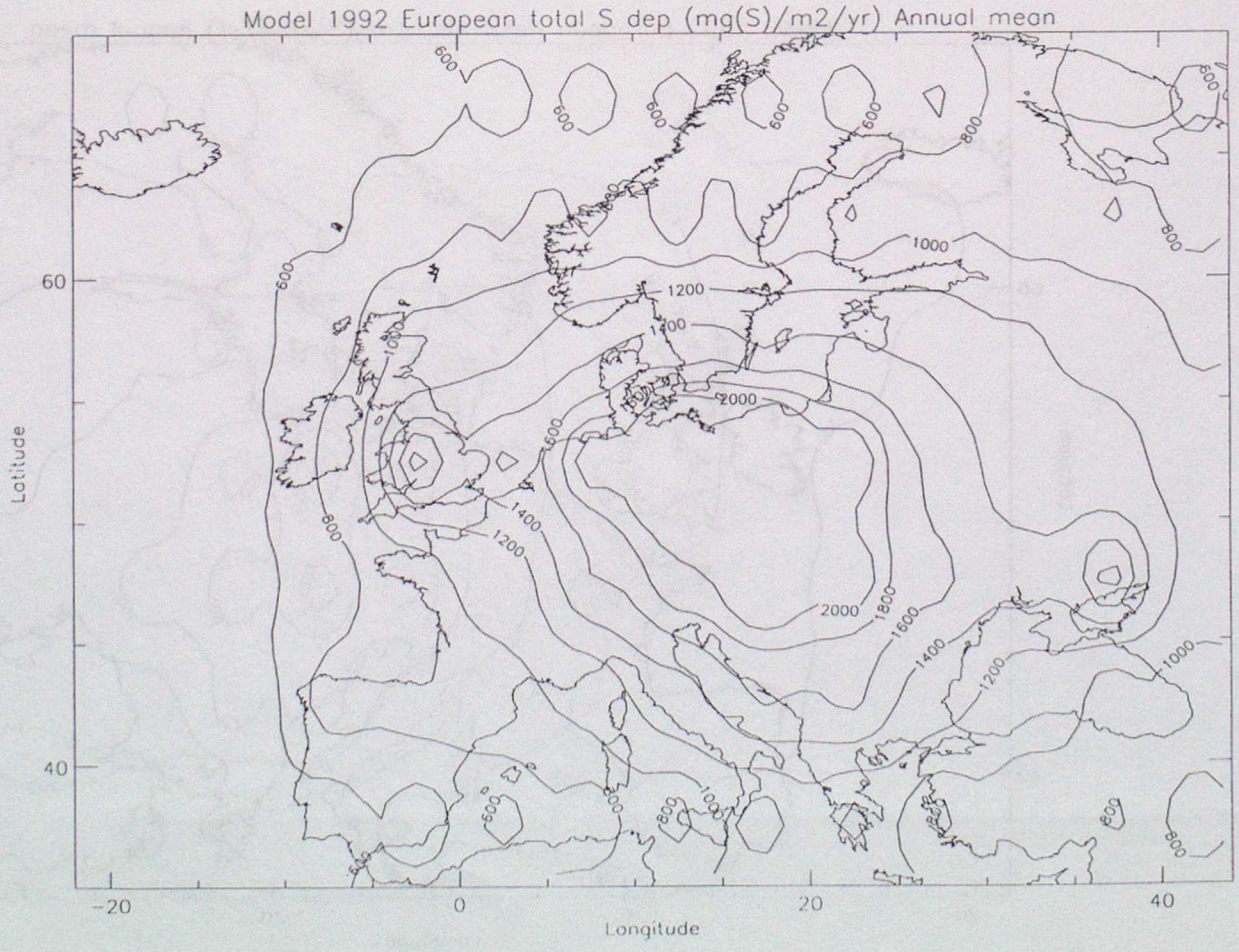

Figure 13. The European wet oxidised nitrogen deposition field, based on a) 1994 EMEP observations and b) STOCHEM for 1992 emissions.

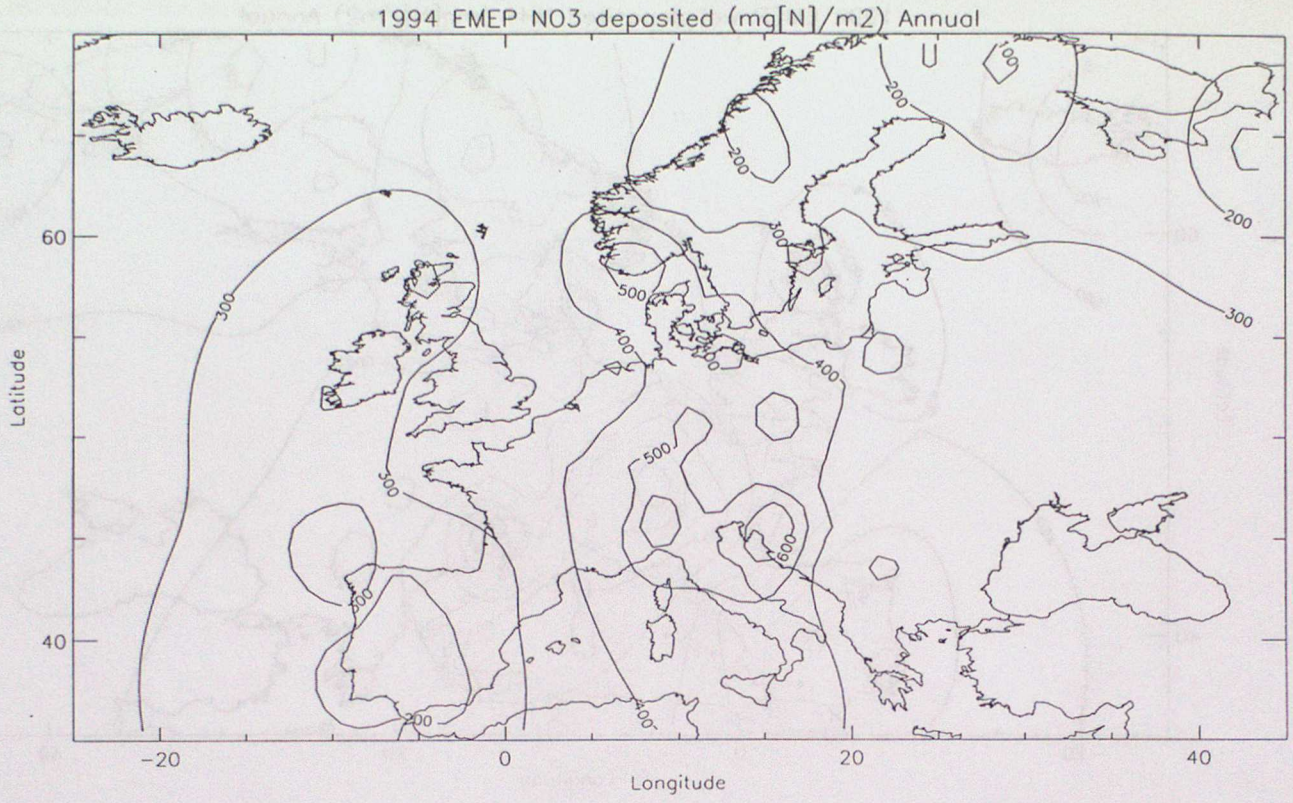

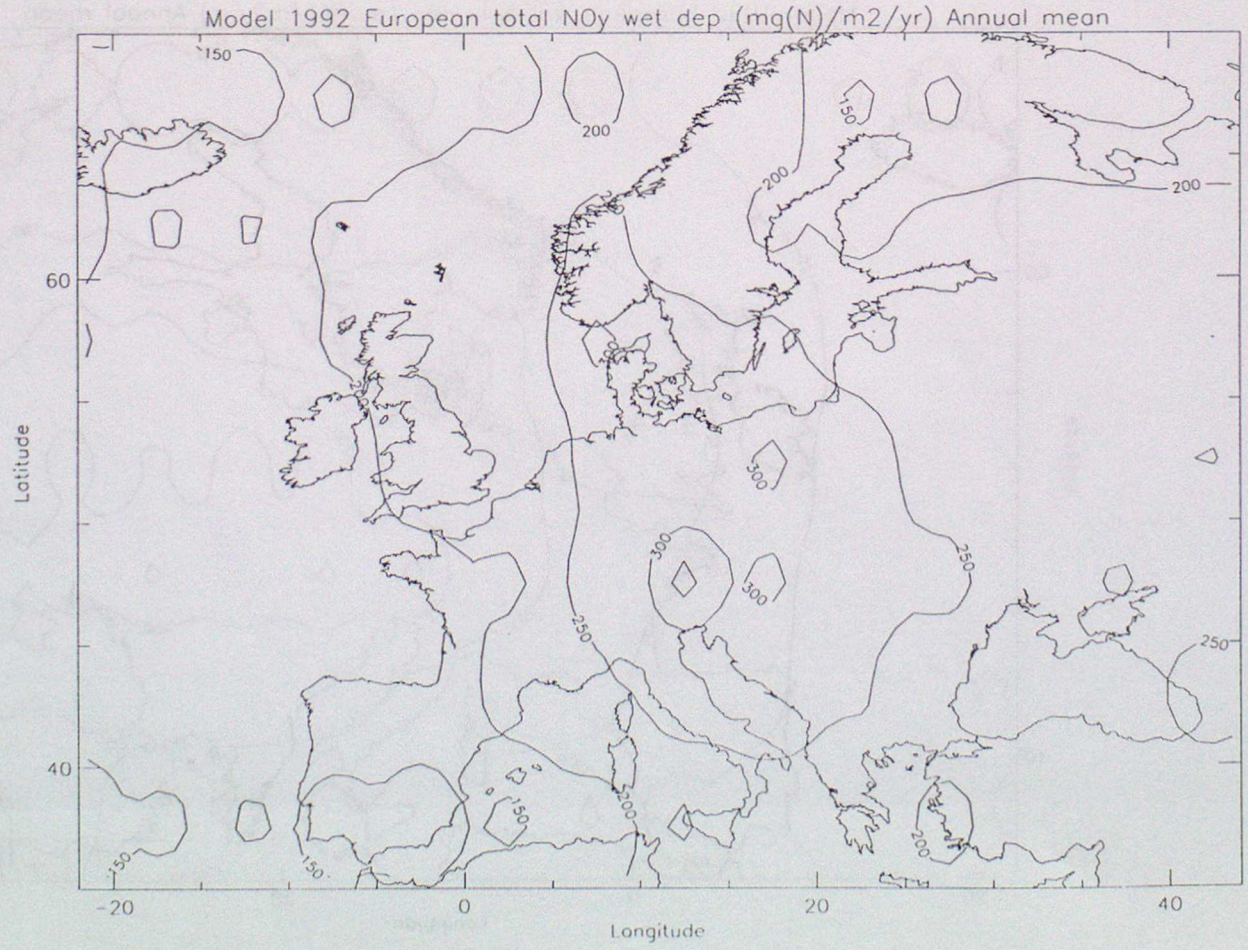

Figure 14. The European wet reduced nitrogen deposition field, based on a) 1994 EMEP observations and b) STOCHEM for 1992 emissions.

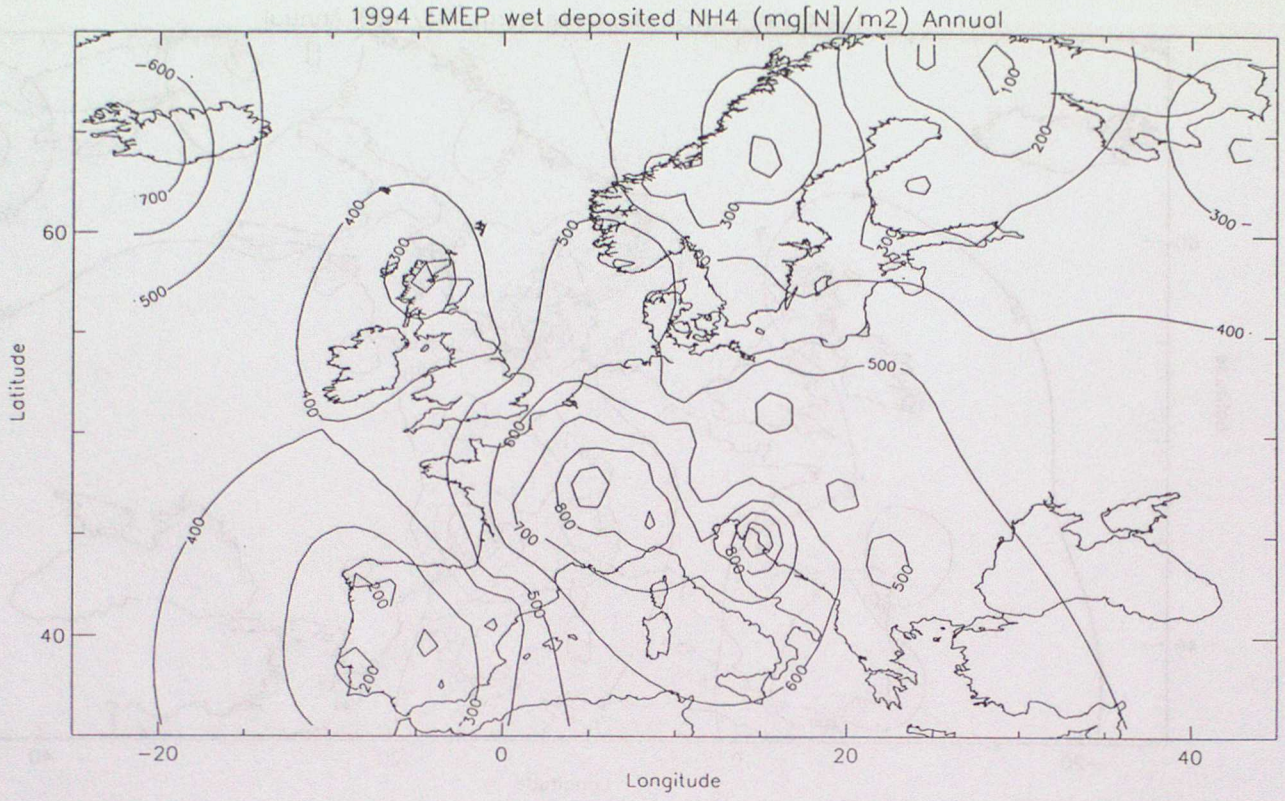

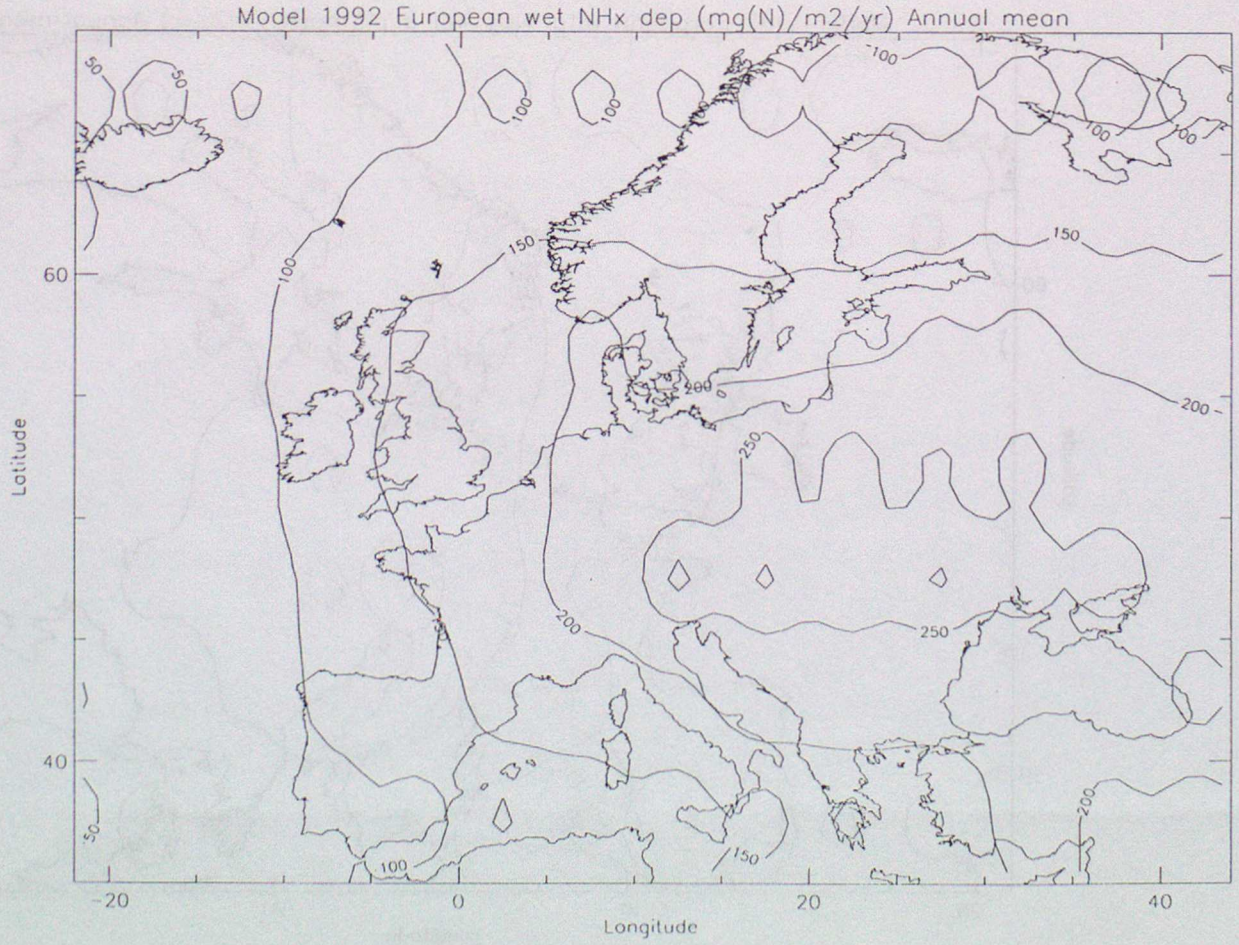

Figure 10. The European dry sulphur deposition field, based on a) 1994 EMEP observations and b) STOCHEM for 1992 emissions.

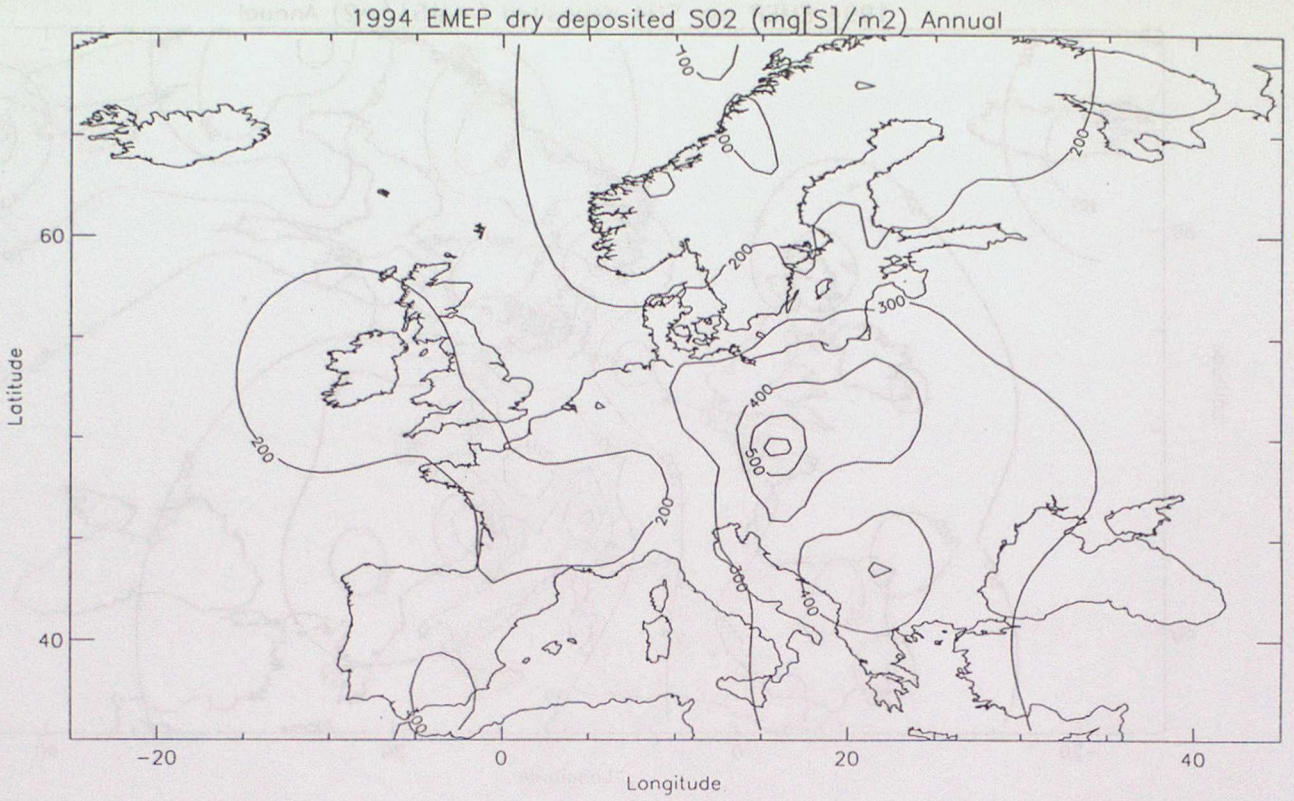

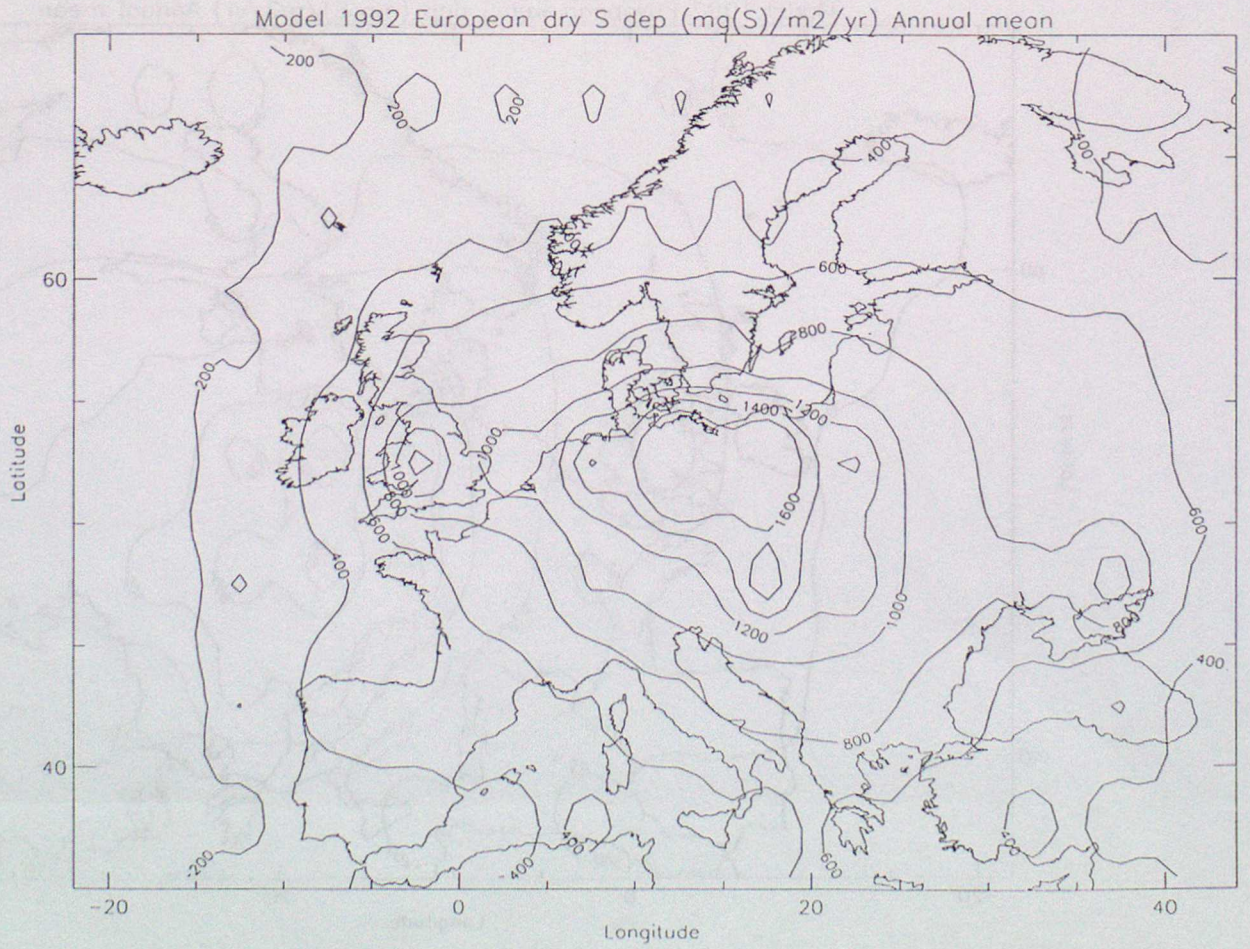

Figure 11. The European wet sulphur deposition field, based on a) 1994 EMEP observations and b) STOCHEM for 1992 emissions.

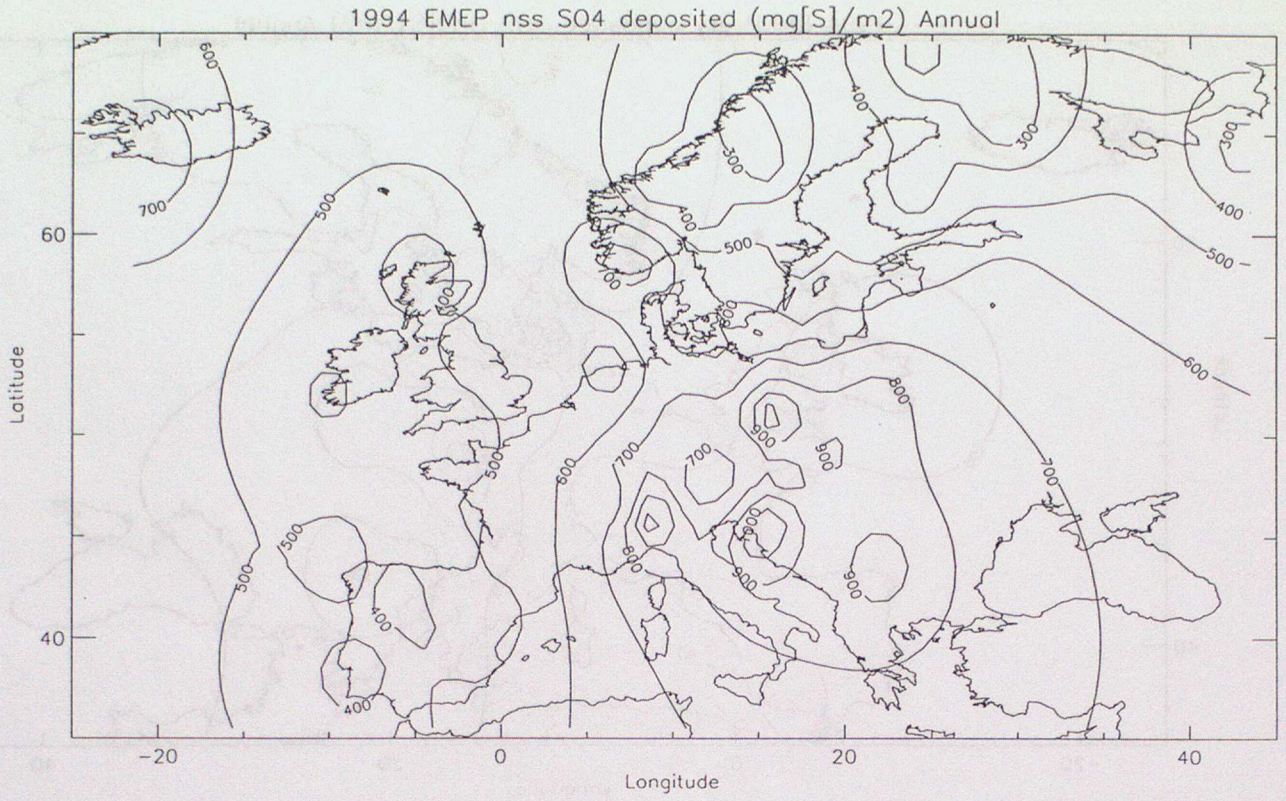

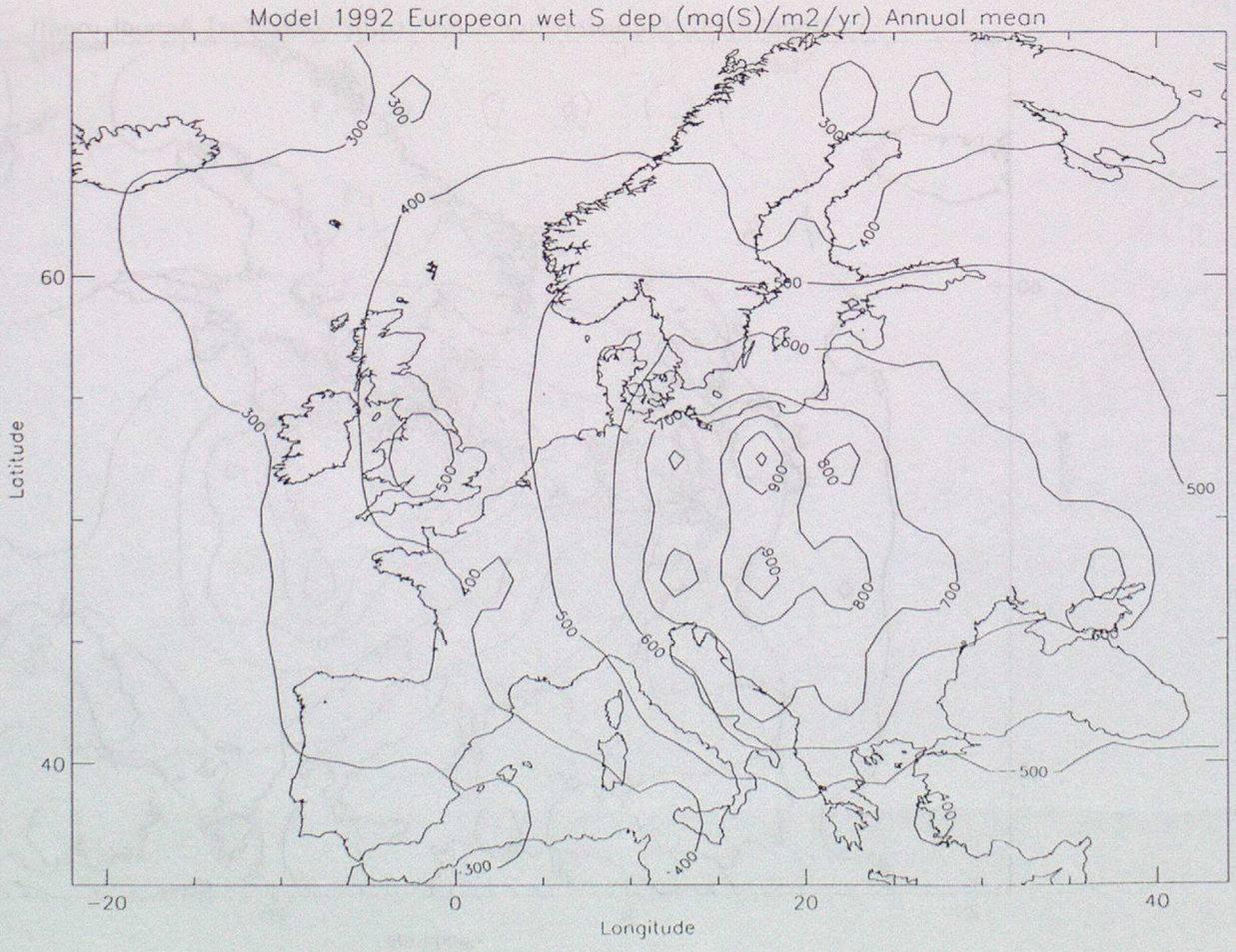

Figure 12. The European total sulphur deposition field, based on a) 1994 EMEP observations and b) STOCHEM for 1992 emissions.

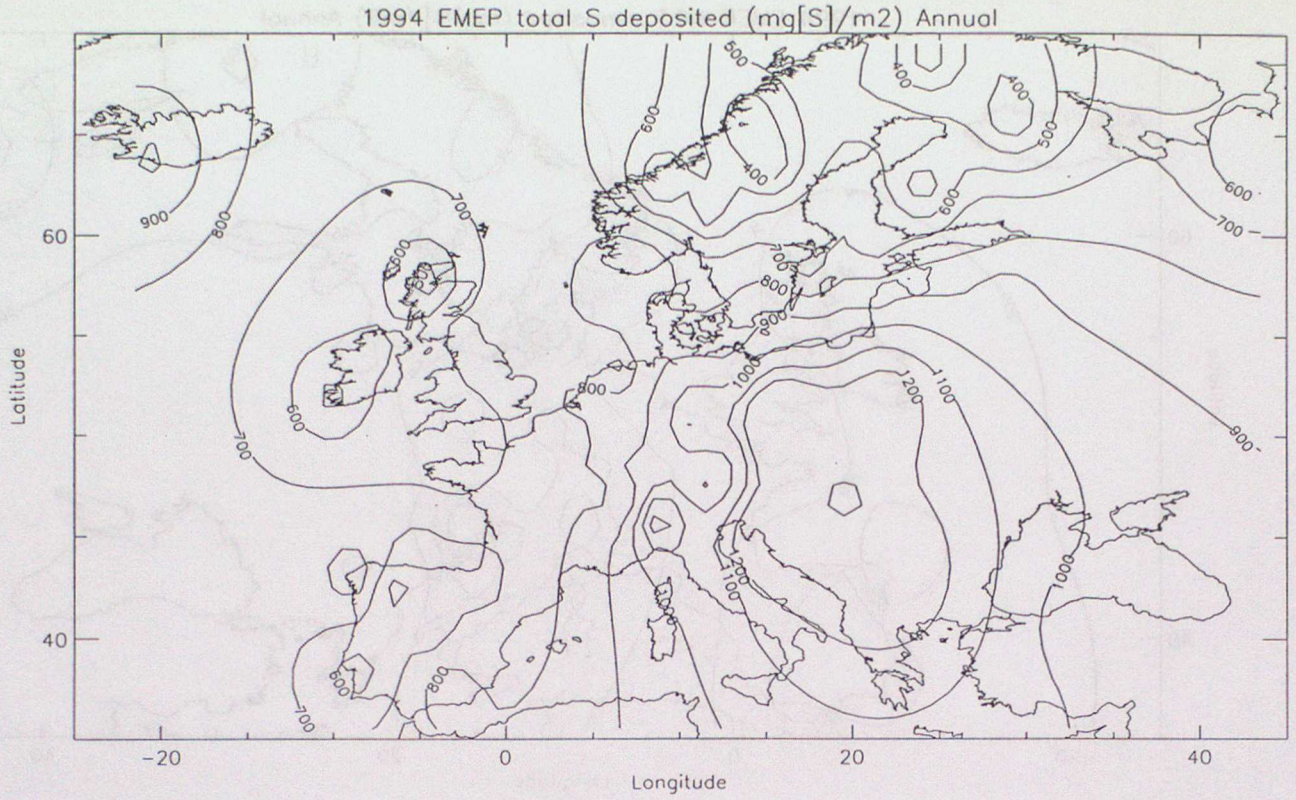

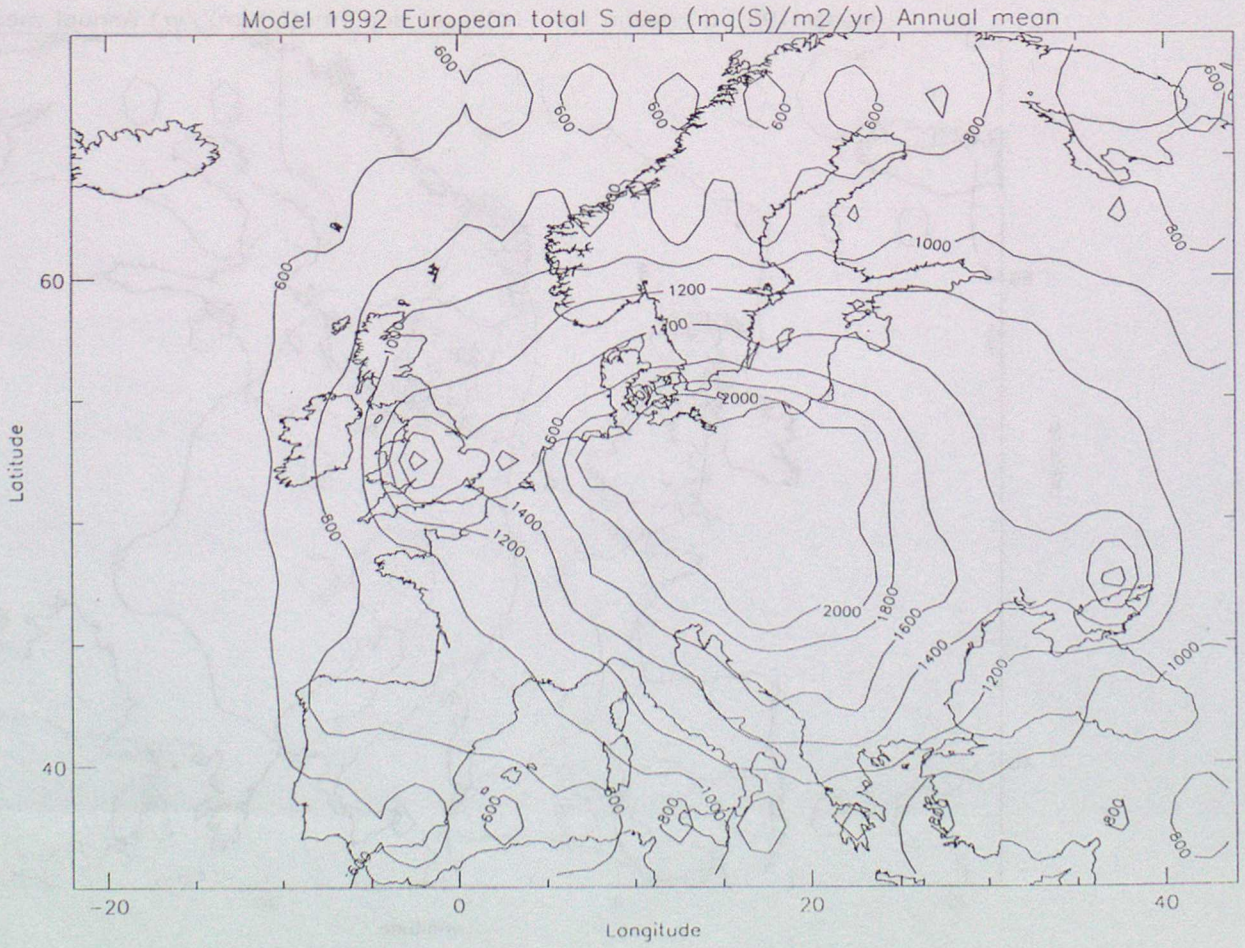

Figure 13. The European wet oxidised nitrogen deposition field, based on a) 1994 EMEP observations and b) STOCHEM for 1992 emissions.

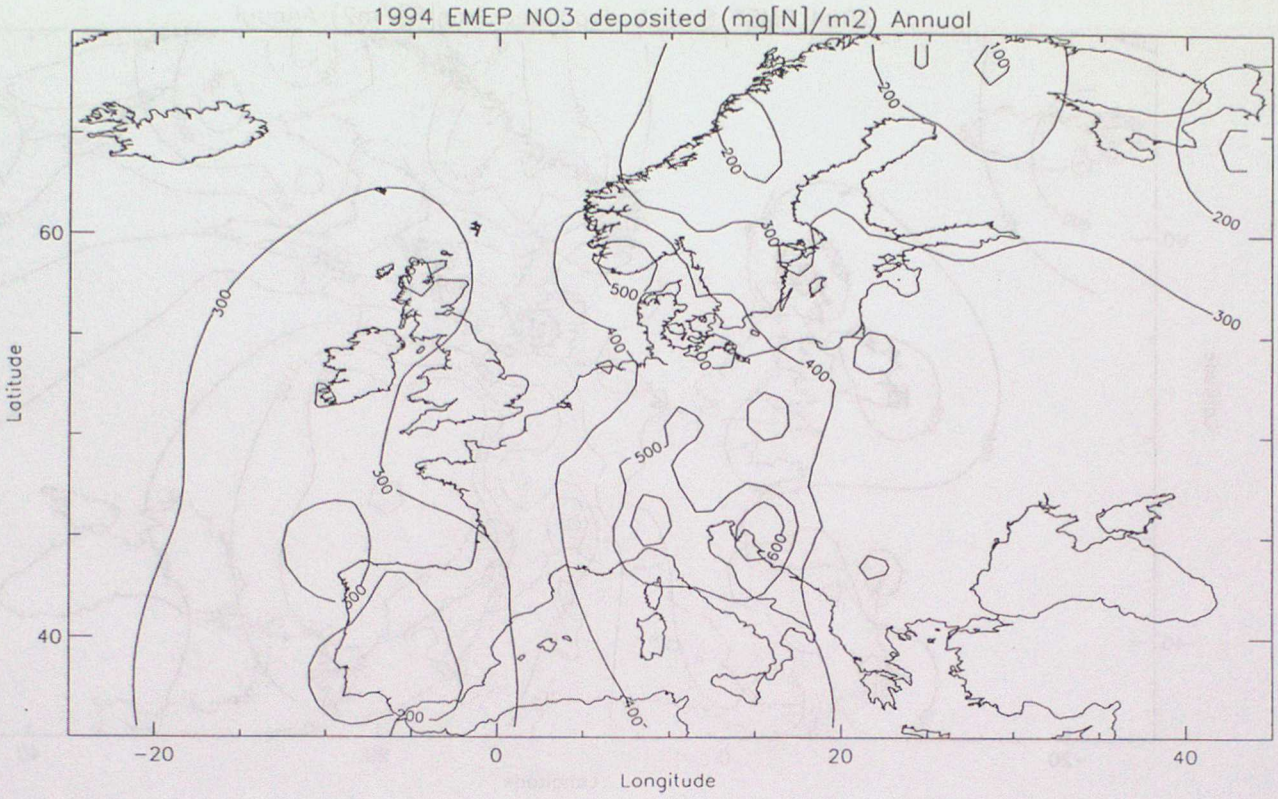

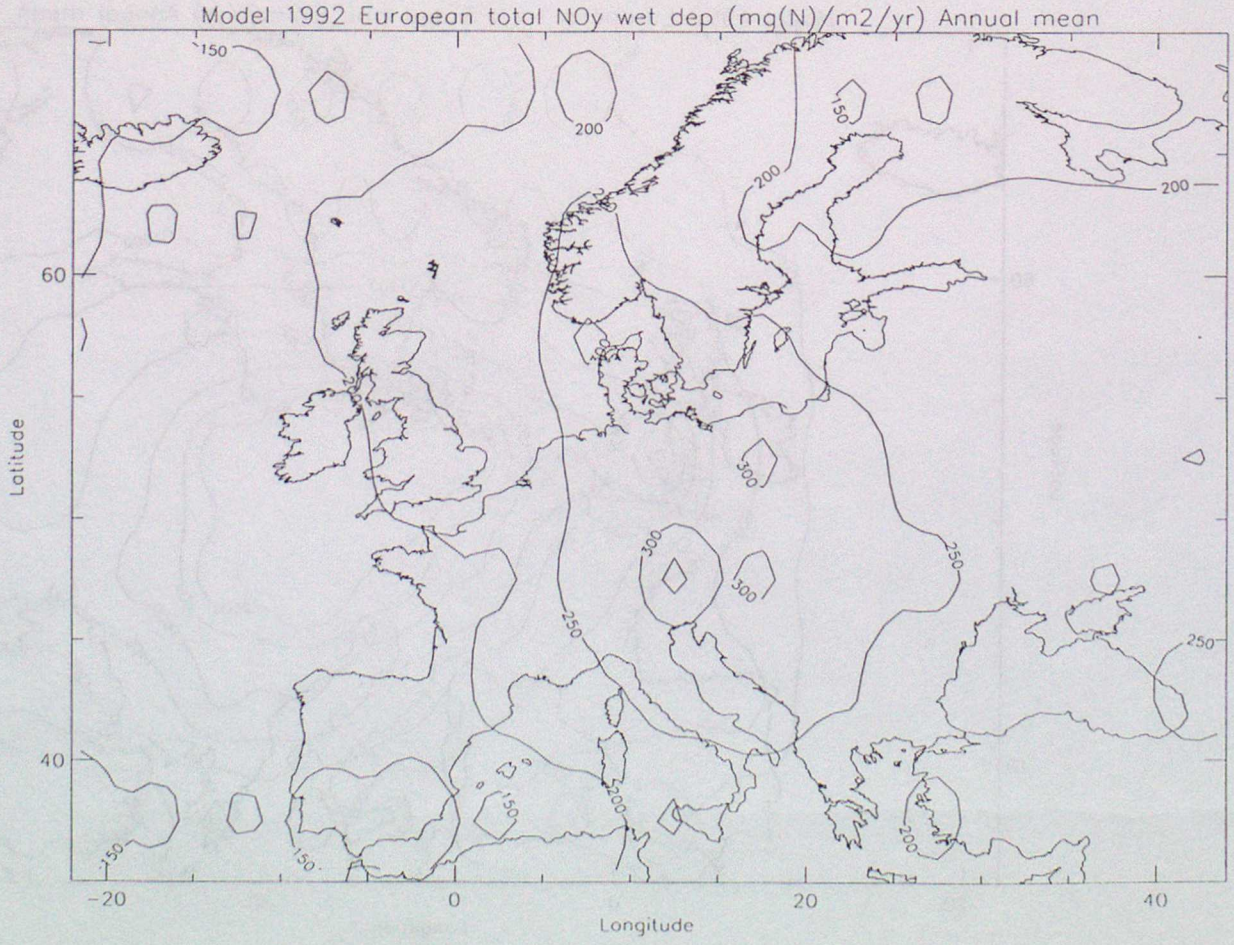

Figure 14. The European wet reduced nitrogen deposition field, based on a) 1994 EMEP observations and b) STOCHEM for 1992 emissions.

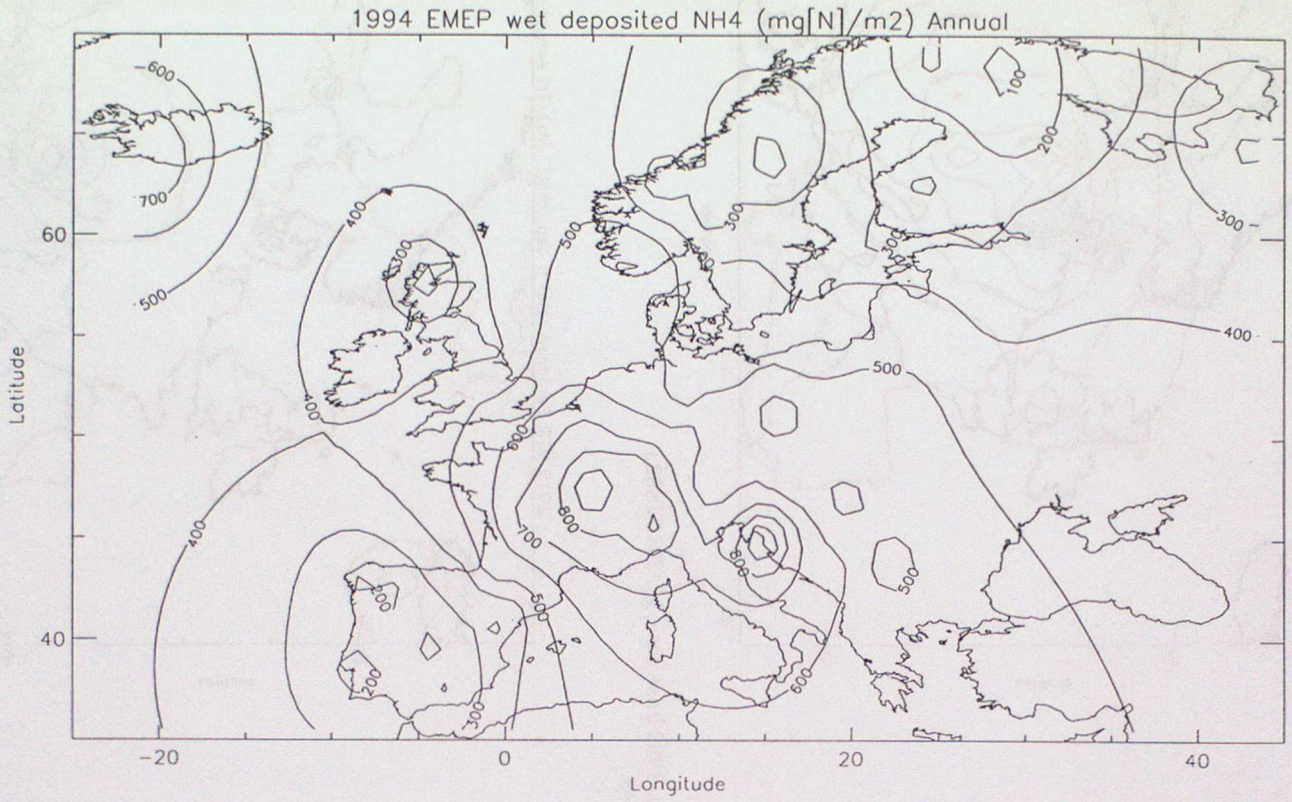

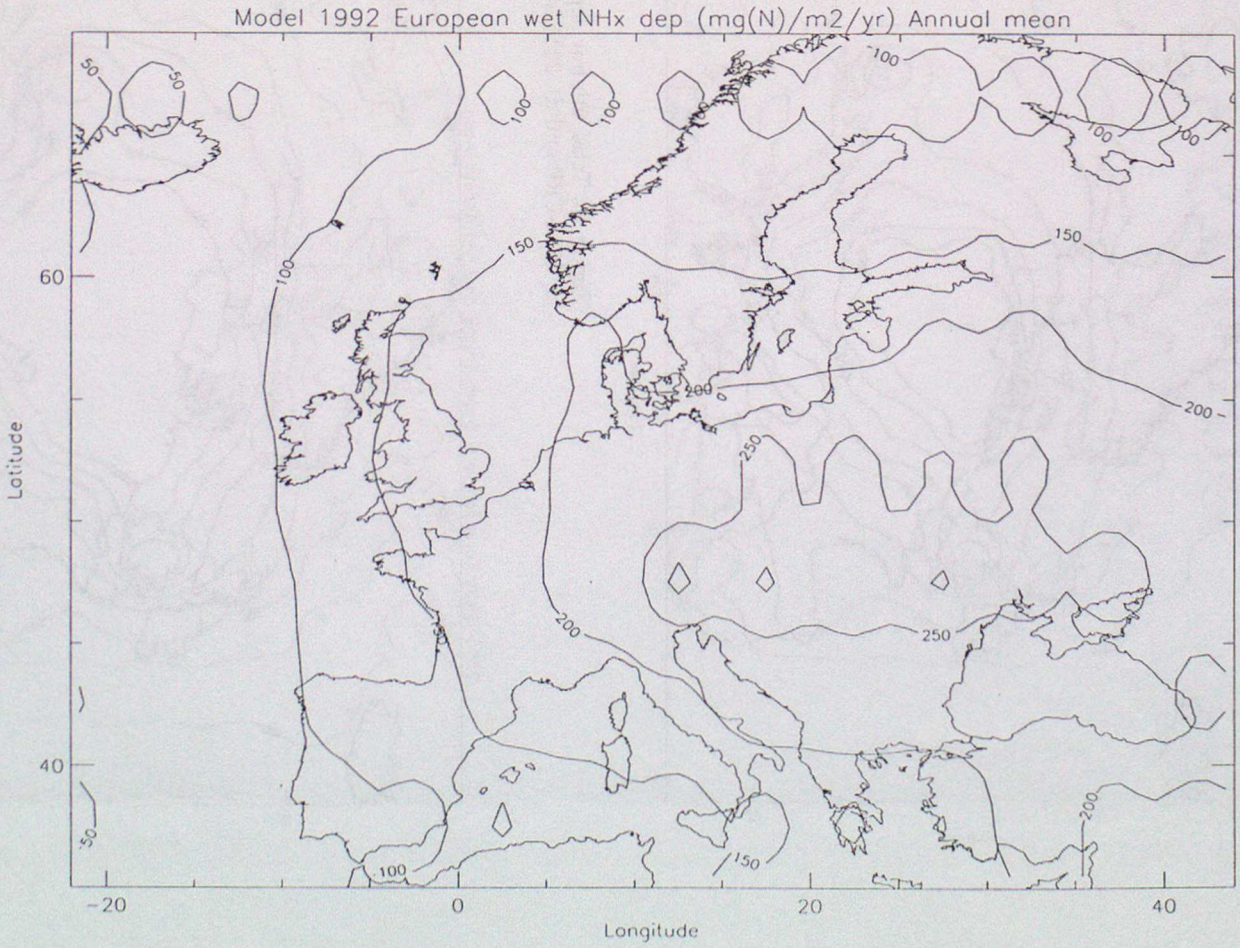

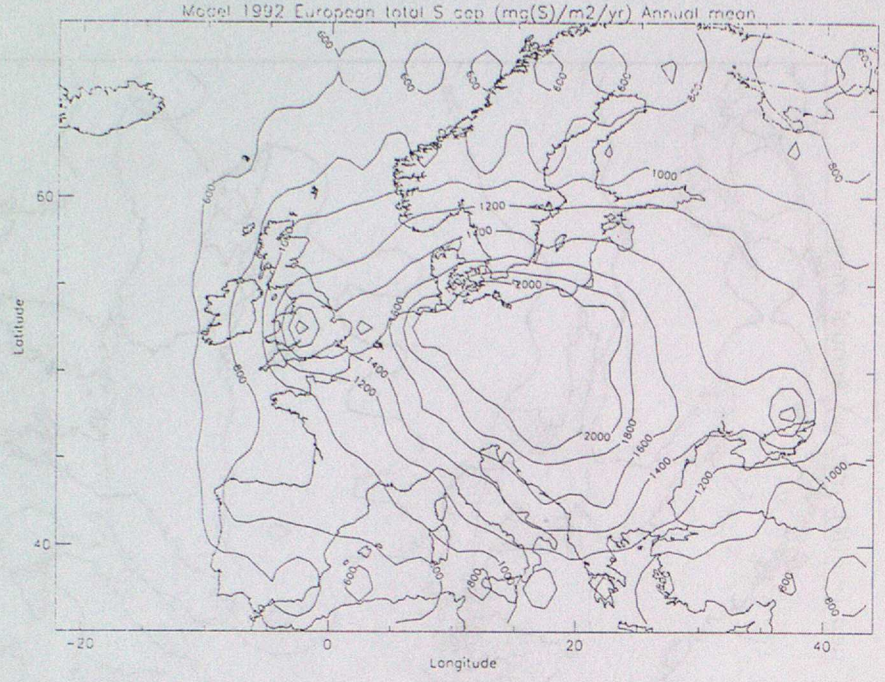

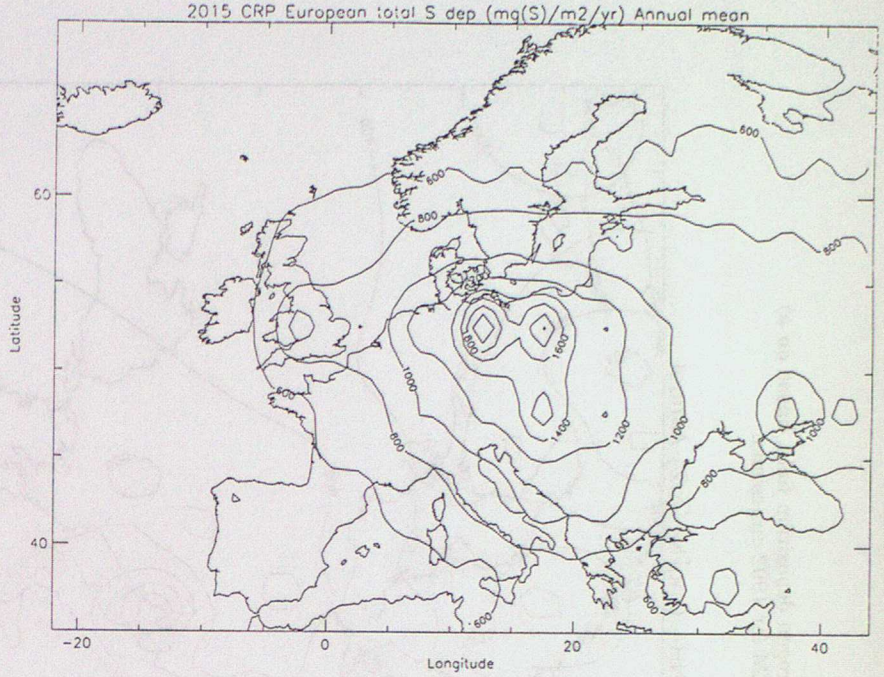

Figure 15. Total sulphur deposition in the a). 1992 base case, b). 2015-IS92a
c). 2015-CRP and d). 2015-MFR scenario cases.

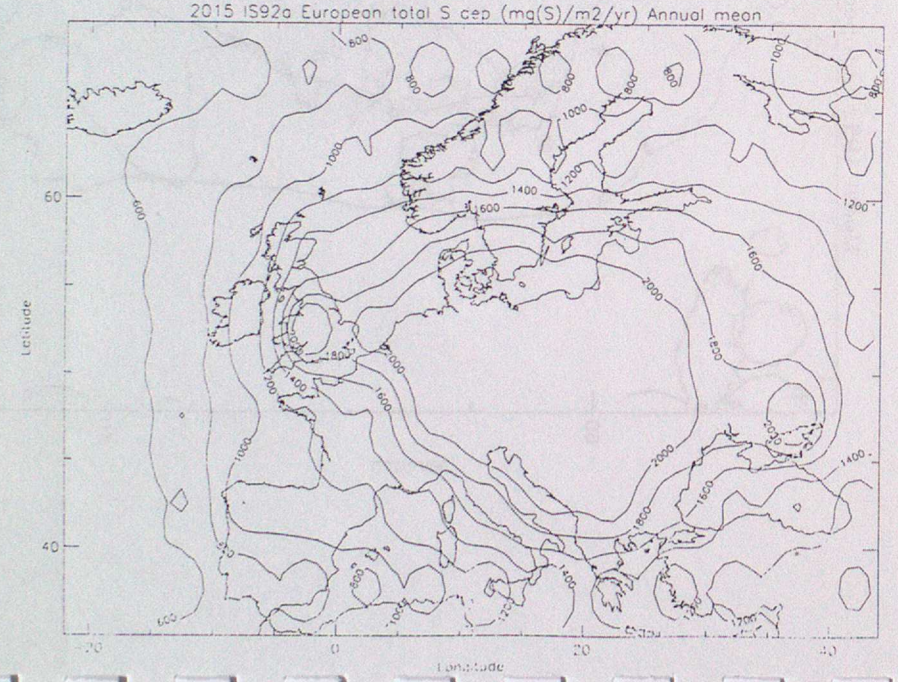

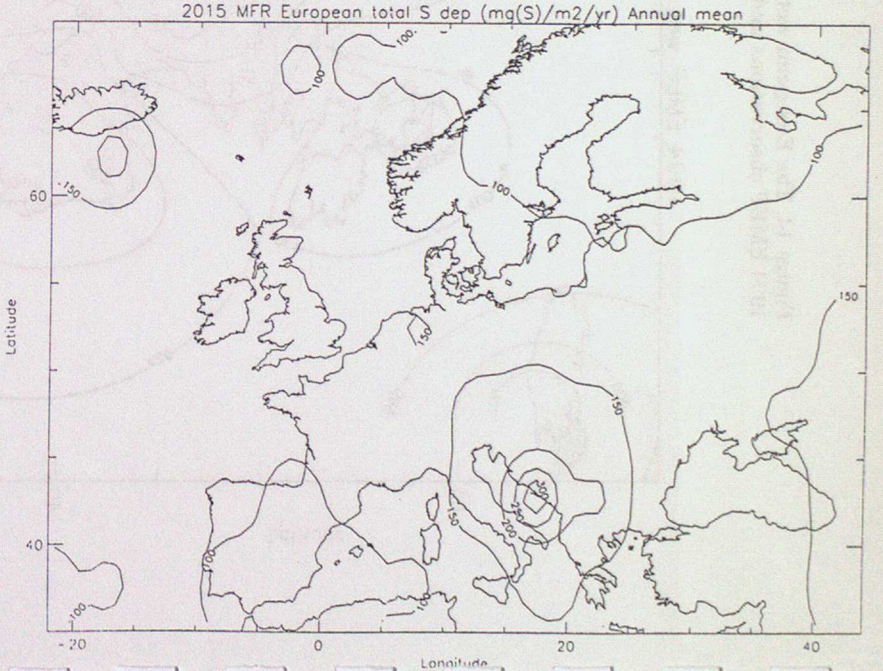

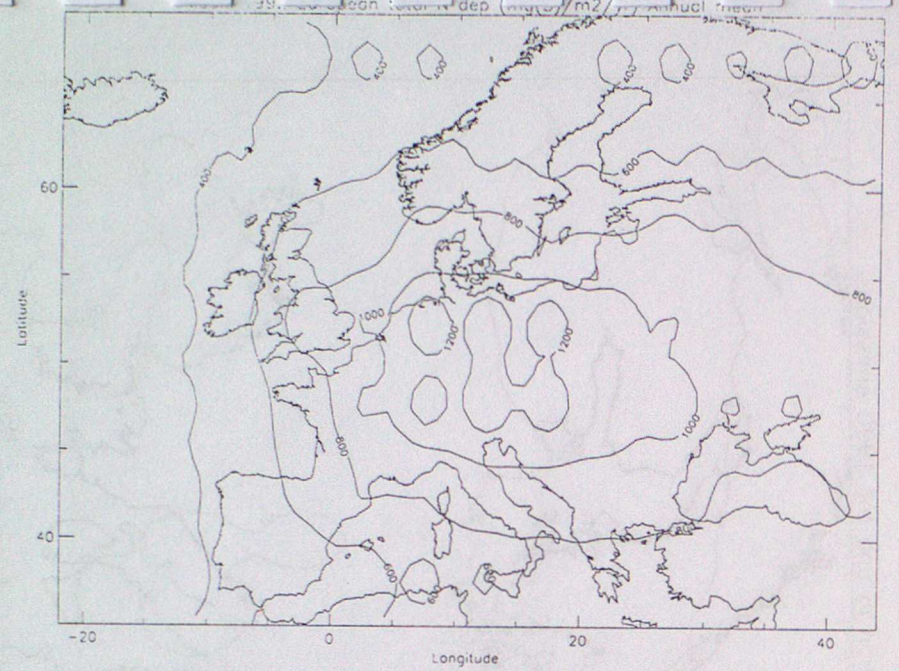

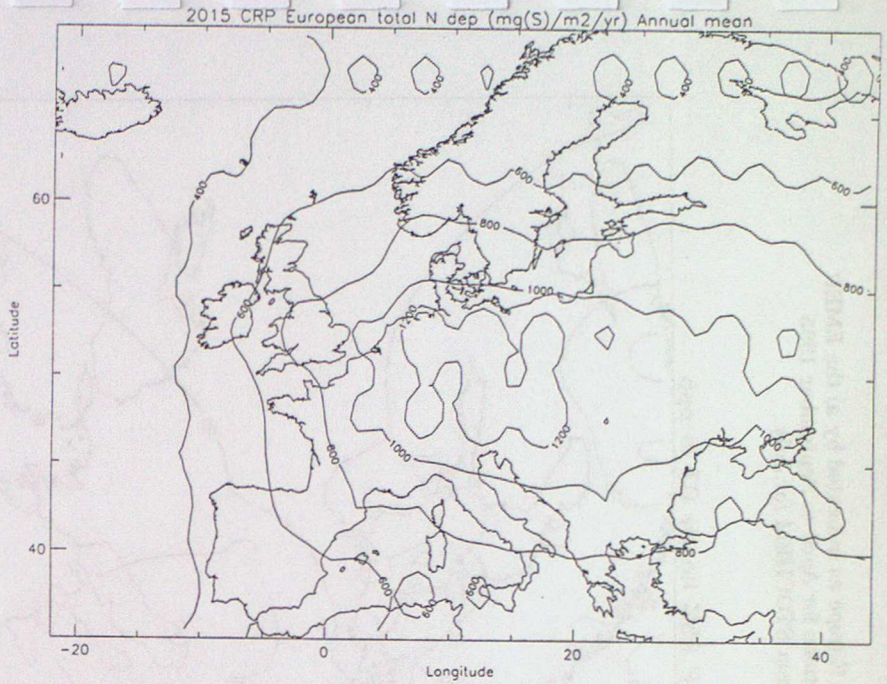

Figure 16. Total nitrogen deposition in the a). 1992 base case, b). 2015-IS92a
c). 2015-CRP and d). 2015-MFR scenario cases.

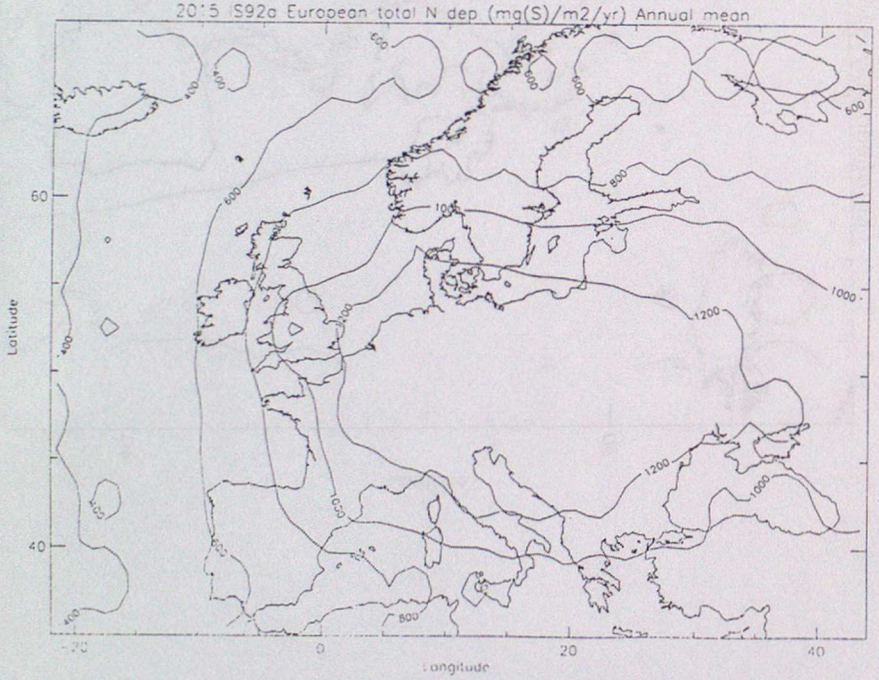

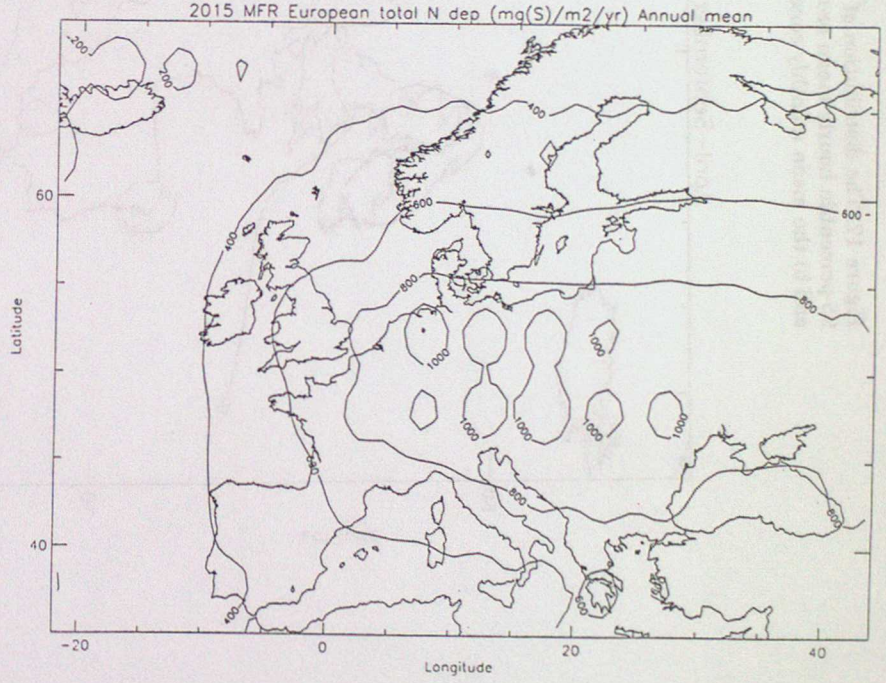

Figure 17. The distribution of ozone across Europe as indicated by a) the EMEP 95-percentile hourly mean ozone concentrations for April to September 1995 and b) the mean monthly concentrations from STOCHEM for July.

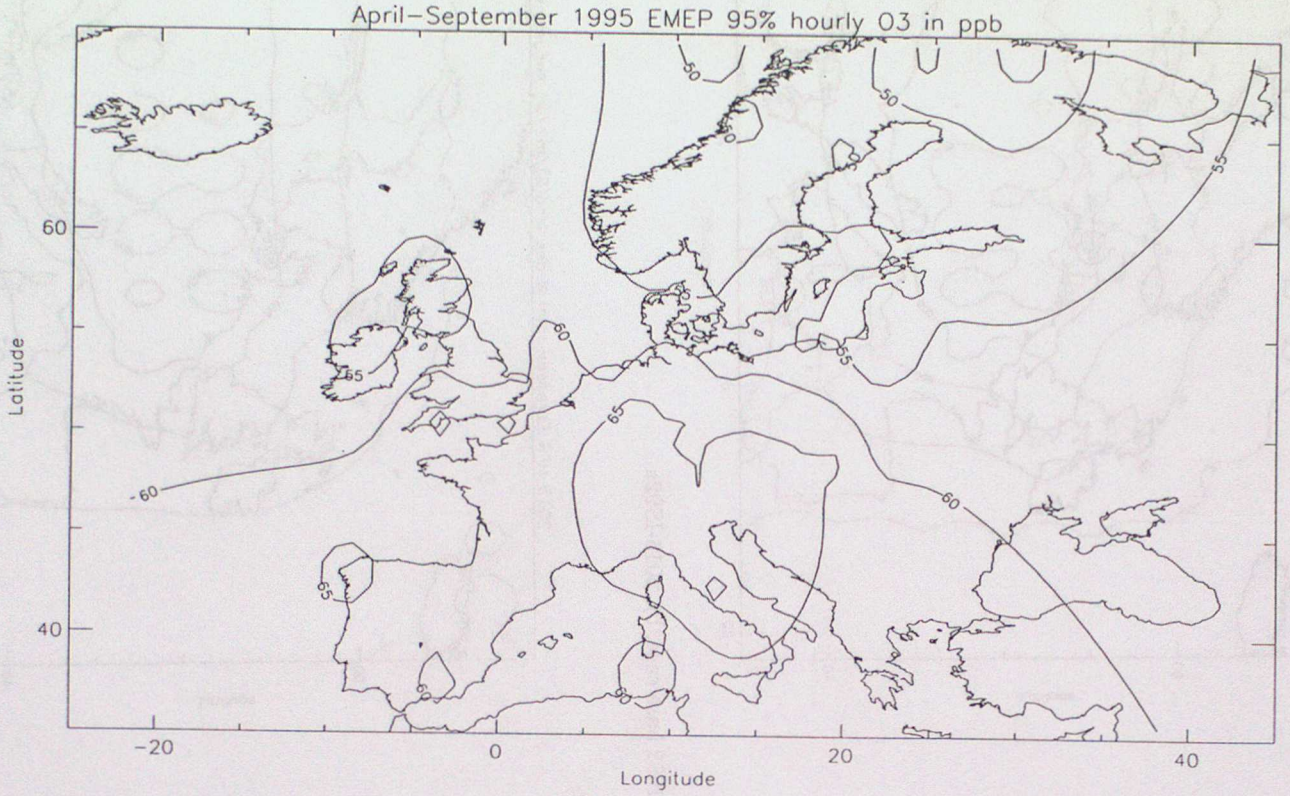

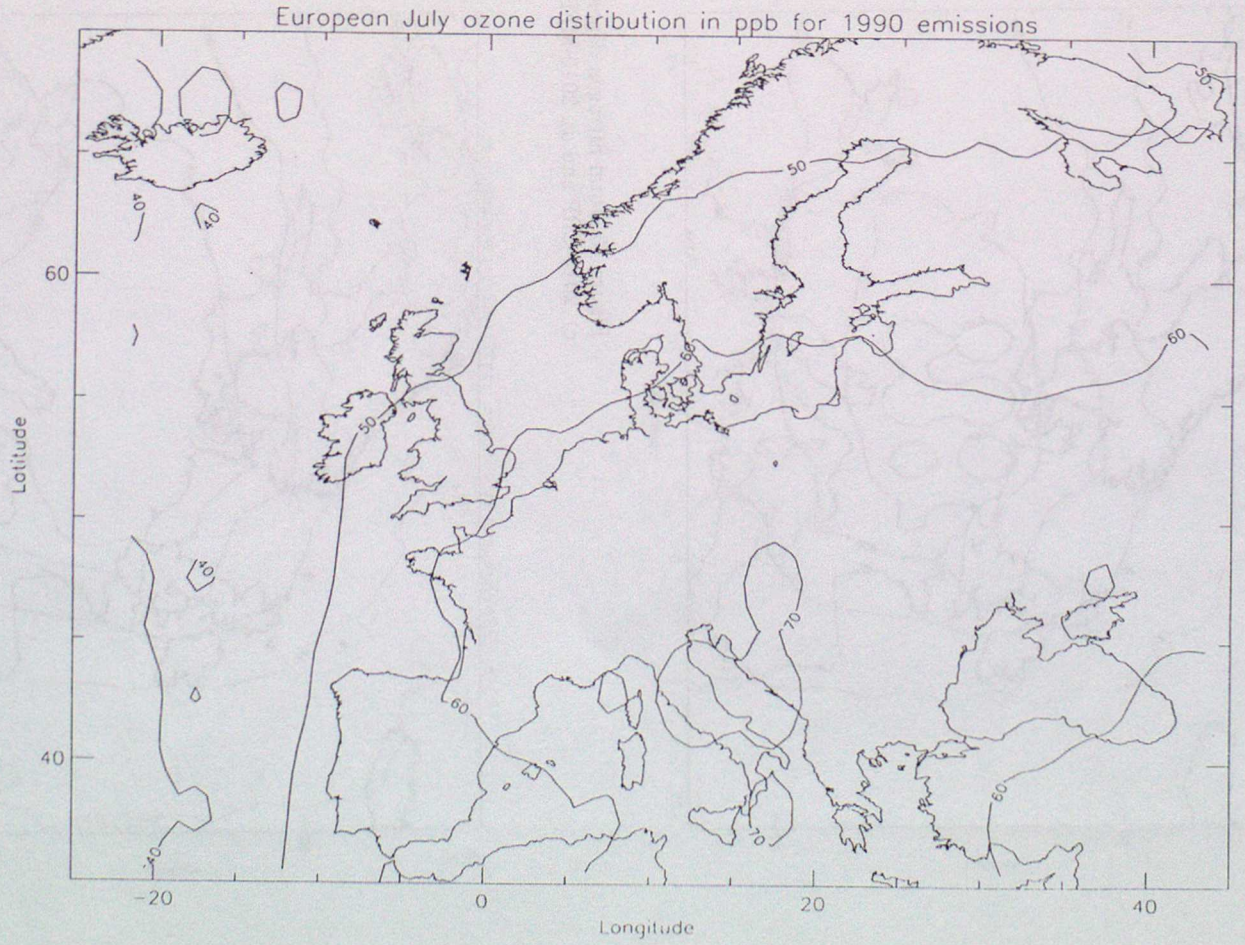

Figure 18. Scatter plots of a). AOT_{60} and b). AOT_{40} crops against the 95-percentile hourly mean ozone concentrations from April to September 1995 for the 96 EMEP monitoring network sites.

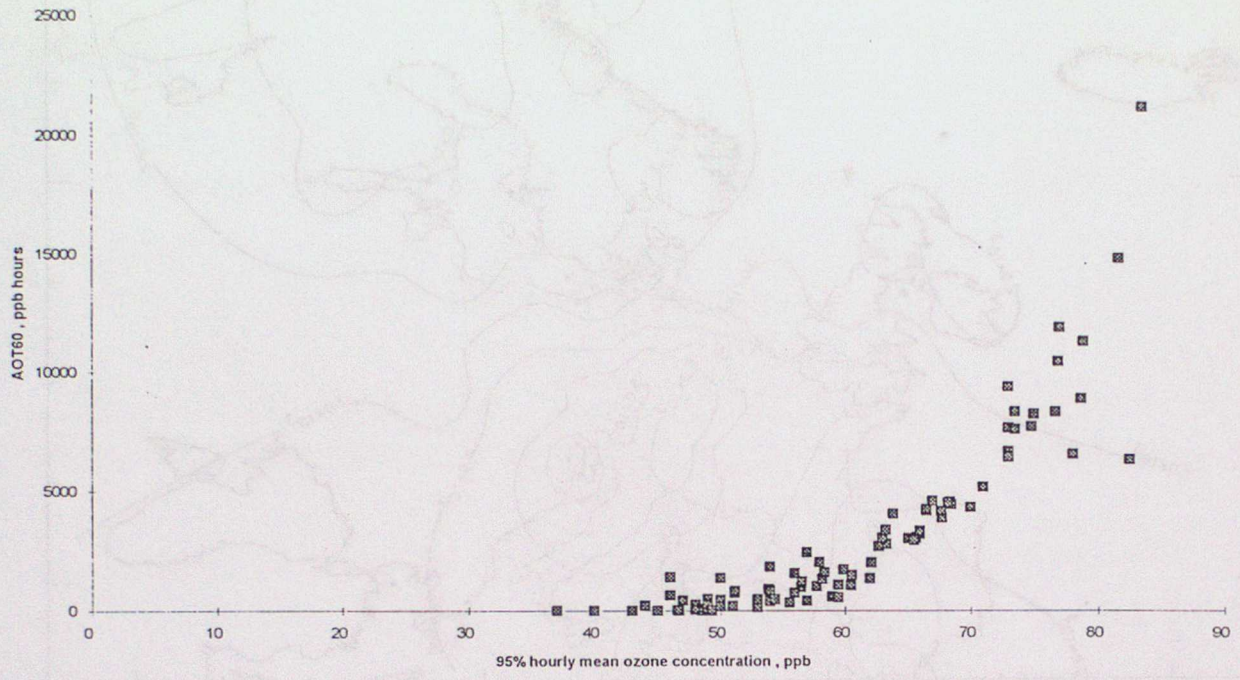

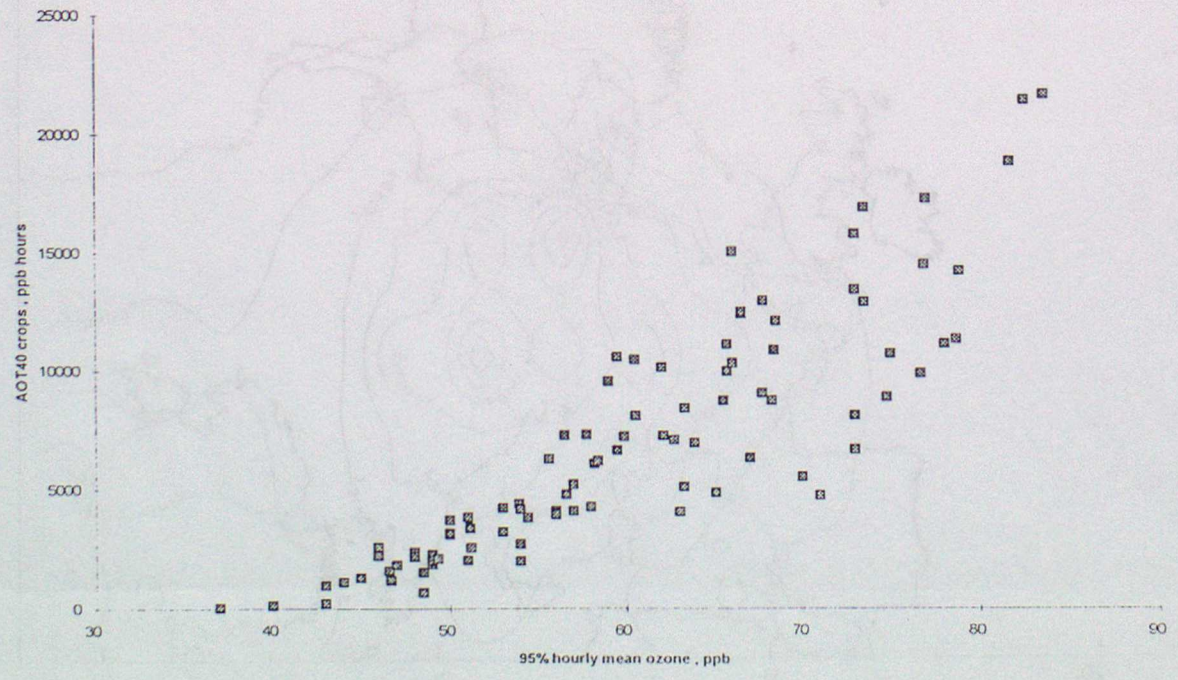

Figure 19. The European AOT_{60} ozone distribution based on a) 1995 EMEP observations and b) STOCHEM for 1992 emissions.

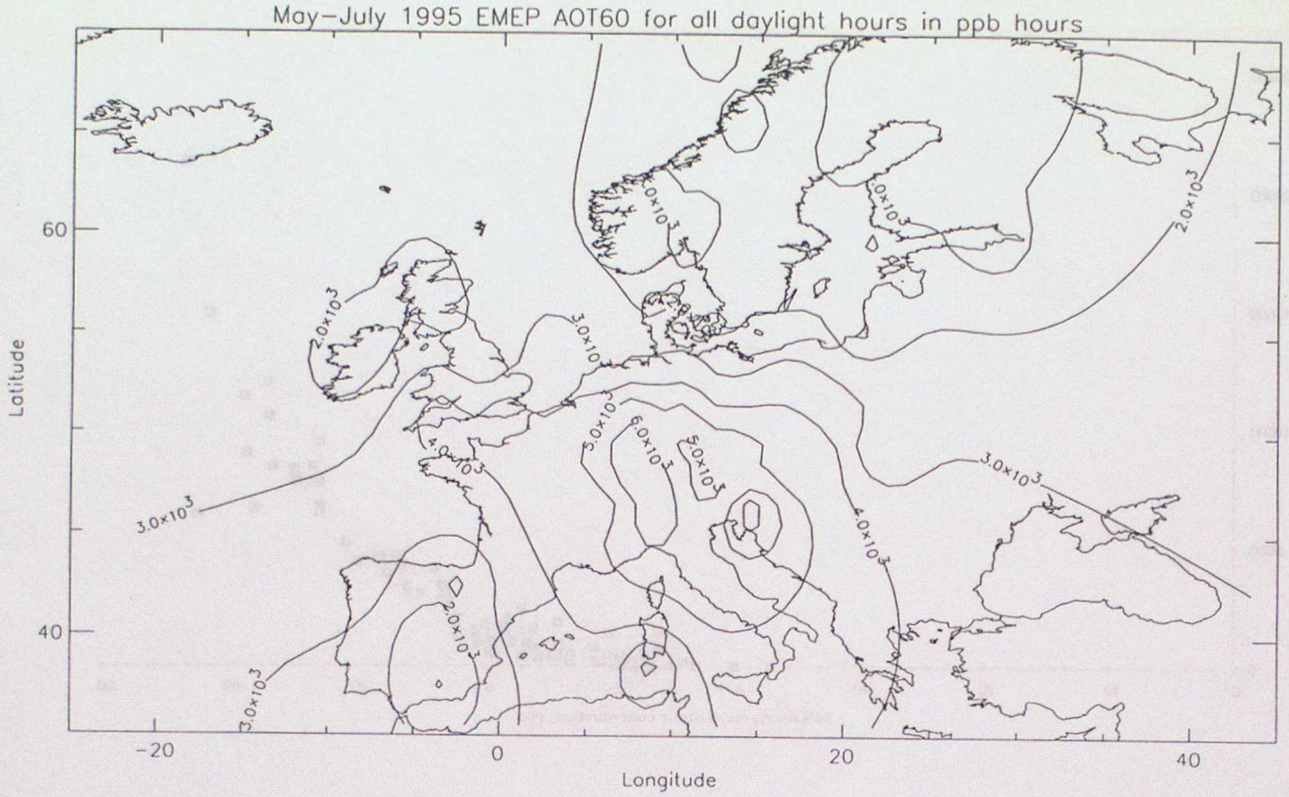

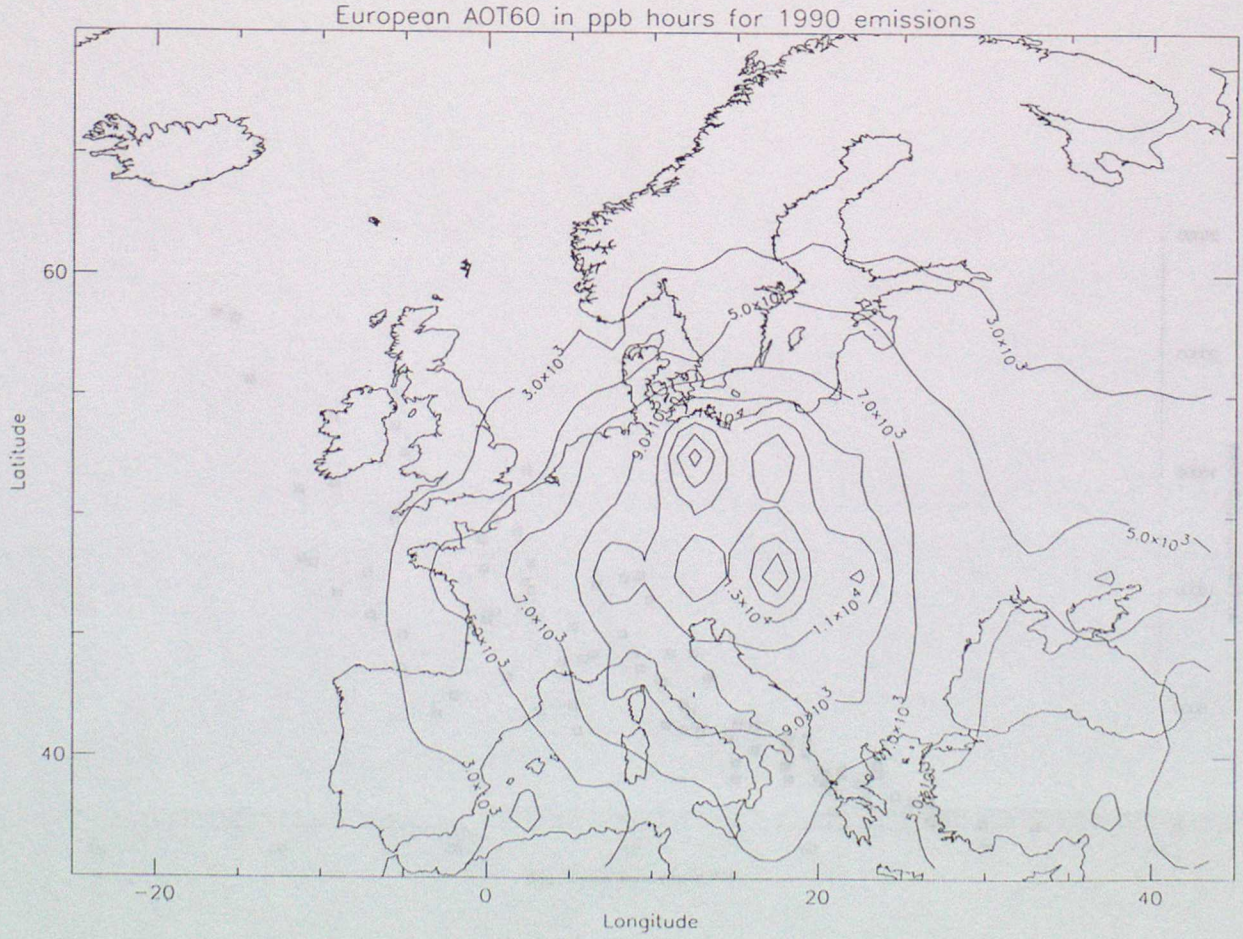

Figure 20. The European AOT_{40} ozone distribution based on a) 1995 EMEP observations and b) STOCHEM for 1992 emissions.

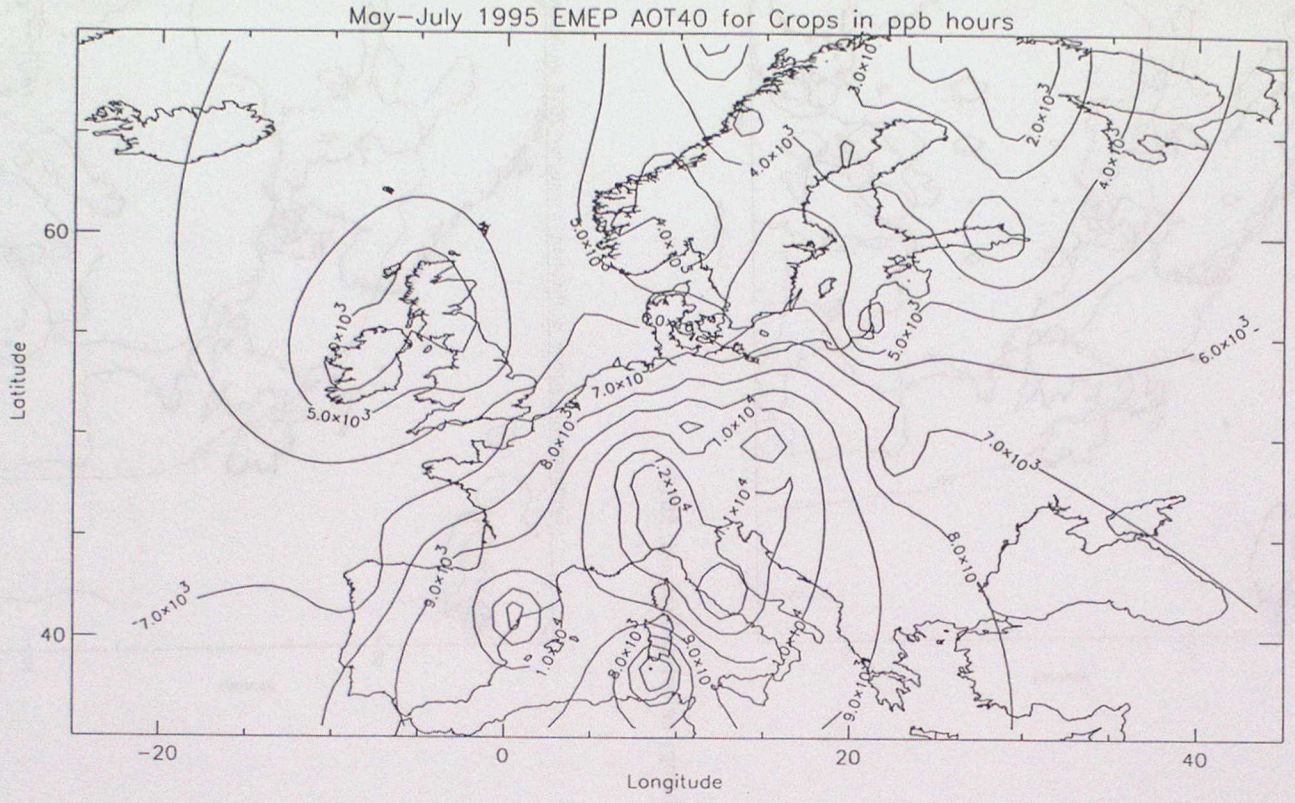

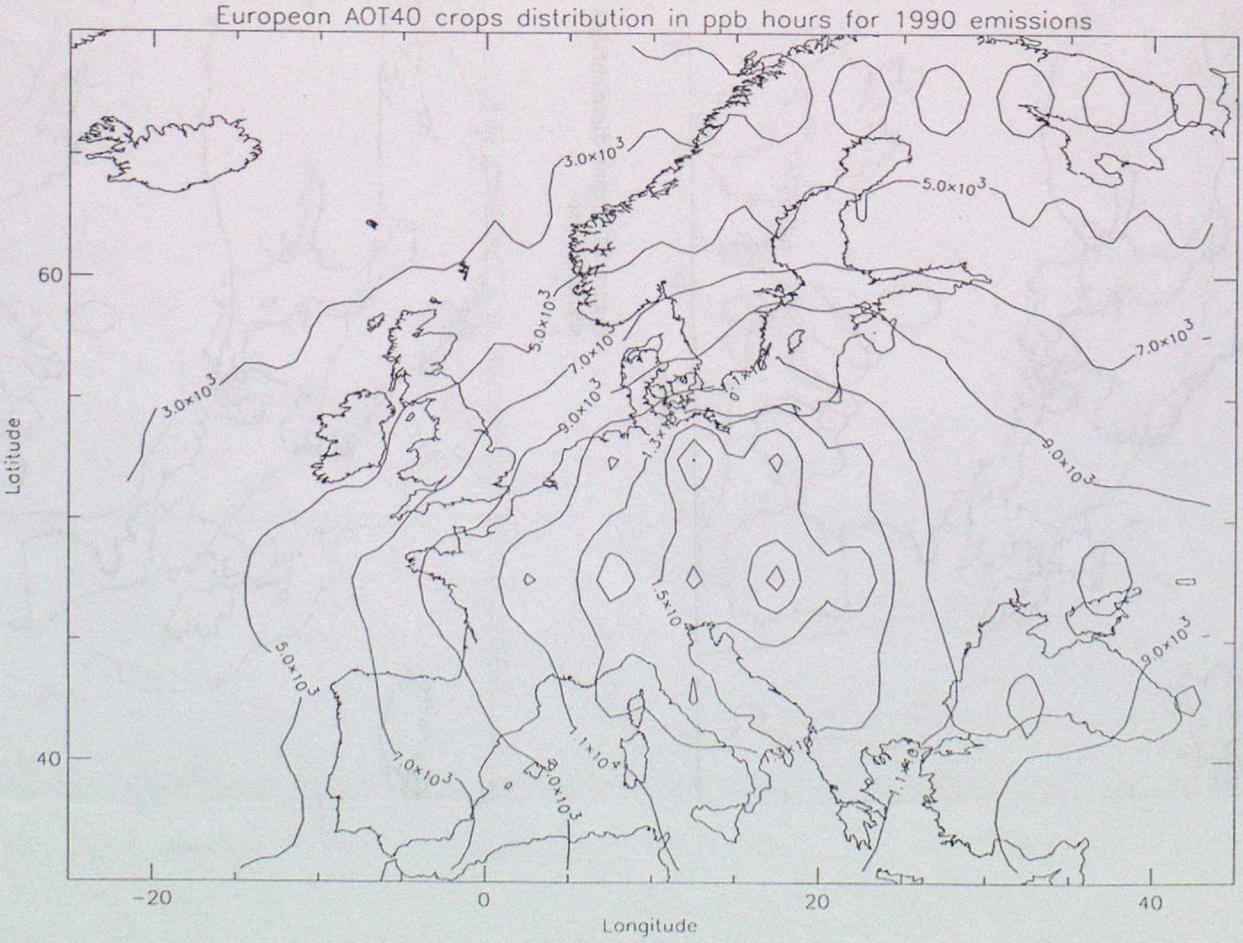

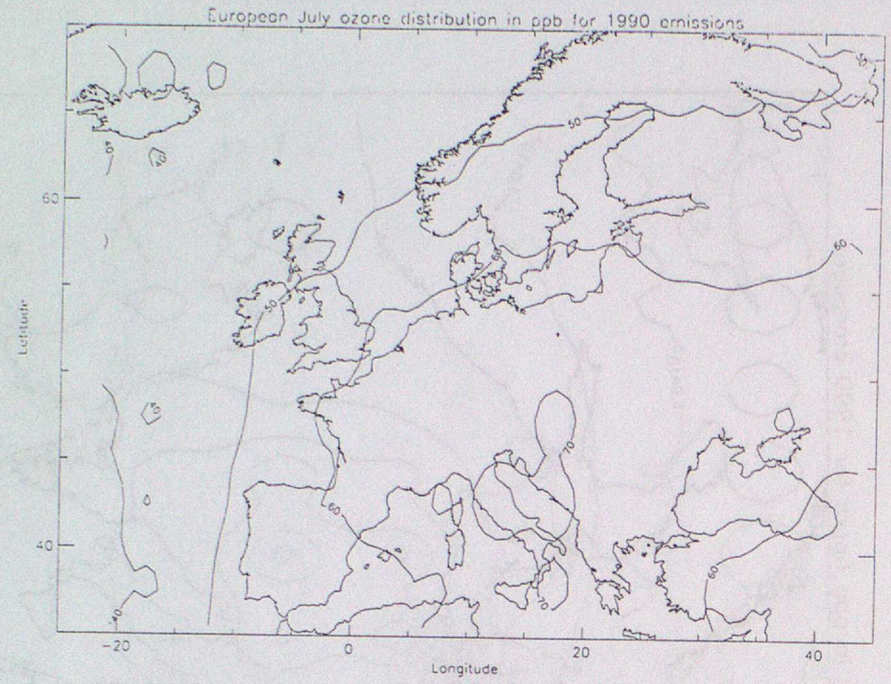

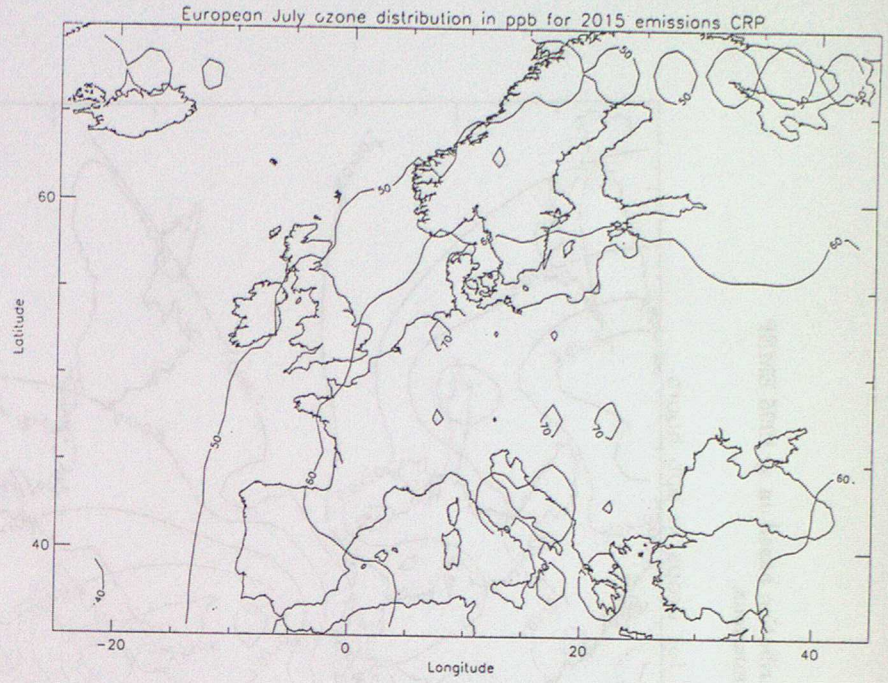

Figure 21. Ozone distributions for July across Europe calculated for a-d) 2015 scenario cases.

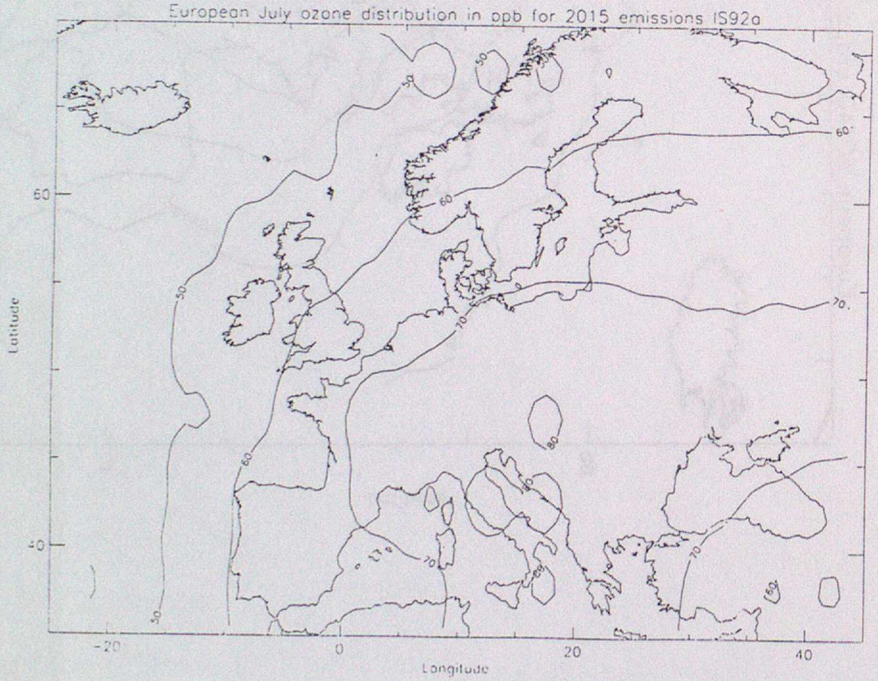

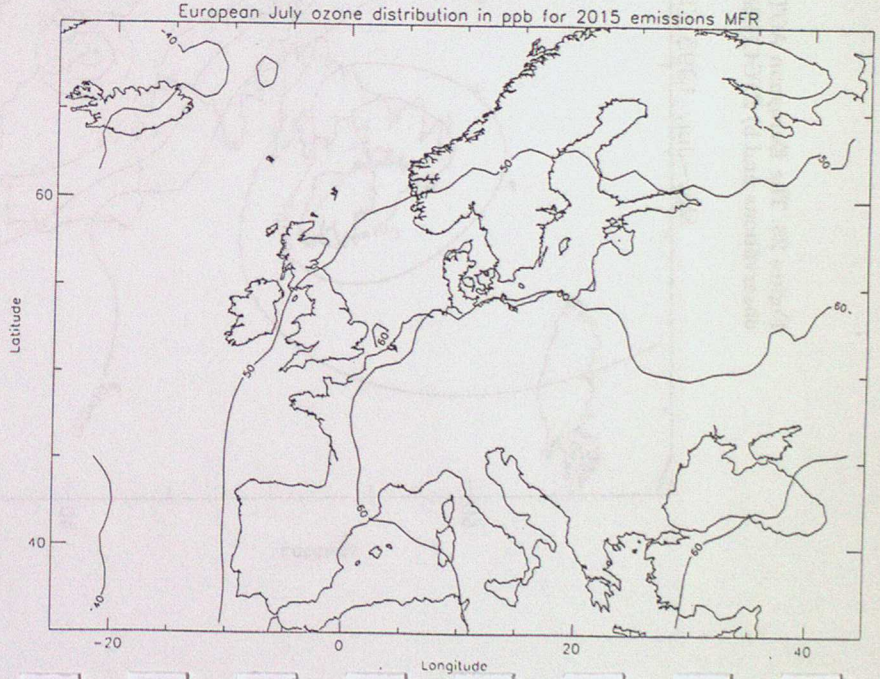

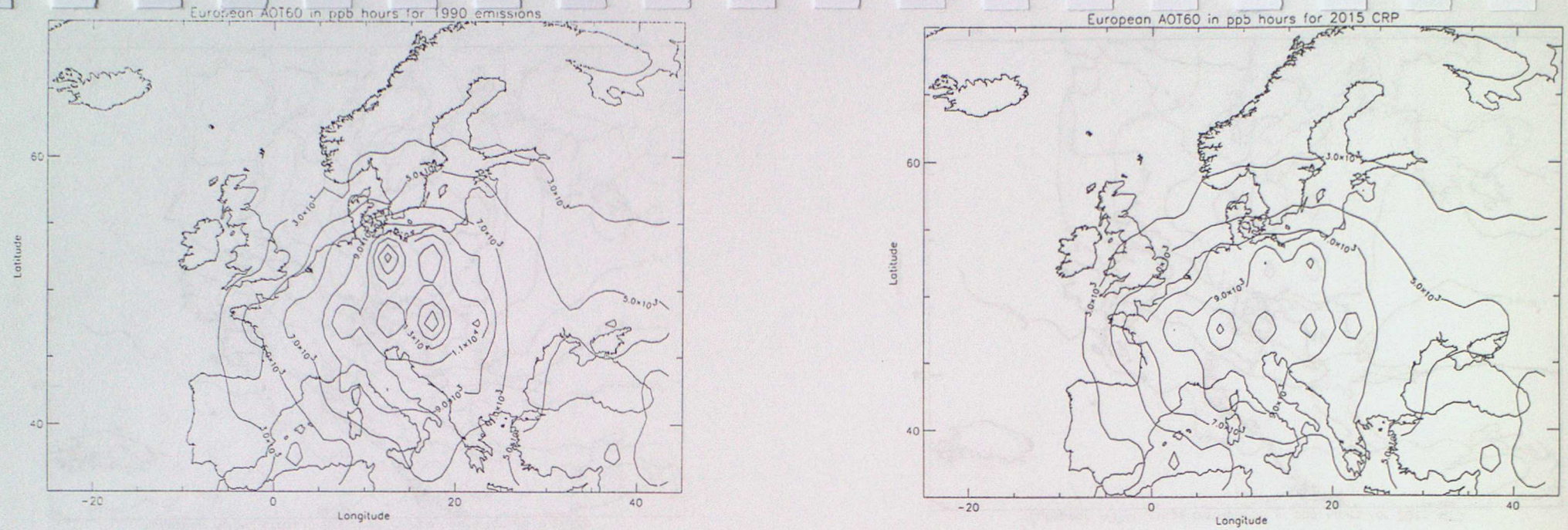

Figure 22. Distributions of AOT_{60} exposures across Europe calculated for a-d) 2015 scenario cases.

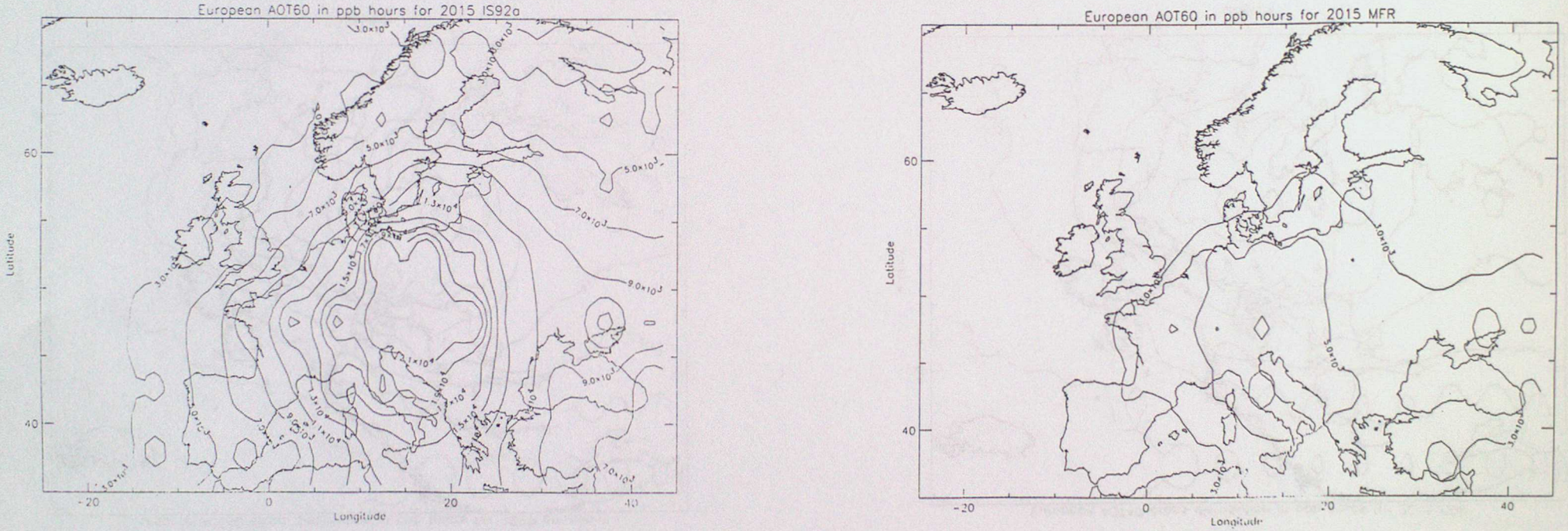

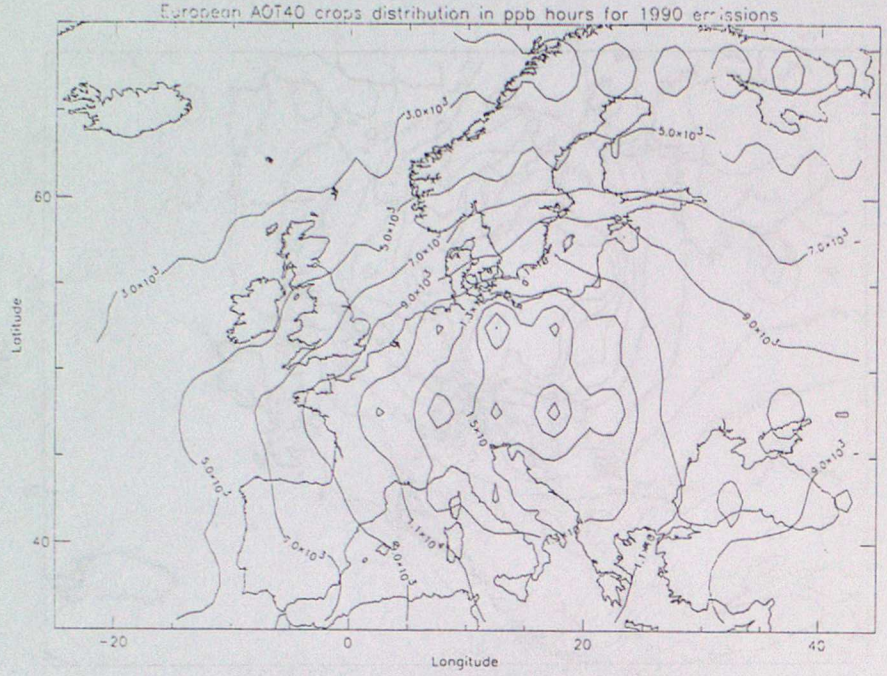

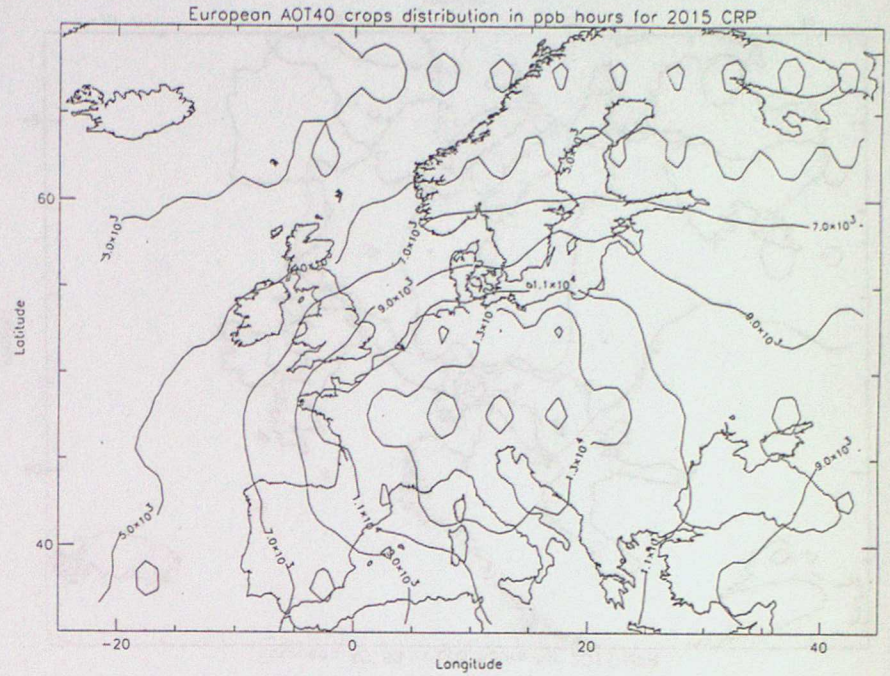

Figure 23. Distributions of AOT_{40} crops across Europe calculated for a-d) 2015 scenario cases.